Thermal design of a helically coiled boiler

by
Jaques Breyten Matolla

Thesis presented in partial fulfilment of the requirements for the degree of Master of Engineering (Mechanical) in the Faculty of Engineering at Stellenbosch University

Supervisor: Prof. Christiaan Meyer

December 2016

DECLARATION

By submitting this thesis electronically, I declare that the entirety of the work contained therein is my own, original work, that I am the sole author thereof (save to the extent explicitly otherwise stated), that reproduction and publication thereof by Stellenbosch University will not infringe any third party rights and that I have not previously in its entirety or in part submitted it for obtaining any qualification.

Date: December 2016

ABSTRACT

This thesis describes the thermal design of a once-through forced circulation helically coiled boiler. The formulation of the one-dimensional steady state thermal model used for sizing the boiler was based on the empirical correlation of Gnielinski and John Thompson best practices.

The magnitude and location of the critical heat flux (CHF) in the helical coil was initially quantified using the empirical correlation of Ünal. Due to the one-dimensionality of the Ünal model and the complexity of the helical coil geometry CFD was used to predict the exact location of the CHF. A single-phase numerical simulation followed by a two-phase flow analysis using the Rensselaer Polytechnic Institute (RPI) wall heat flux partitioning model was used to establish the location and magnitude of the CHF and the results compared to that obtained using the Ünal model. It was found that the Ünal model underestimated the location of the CHF by approximately 37%.

OPSOMMING

Hierdie tesis beskryf die termiese ontwerp van 'n enkel sirkulasie helies gespoelde ketel. Die formulering van die een-dimensionele, bestendige toestand, termiese model wat gebruik was vir die ketel ontwerp was gebaseer op die empiriese korrelasie van Gnielinski en John Thompson se beste praktyke .

Die grootte en ligging van die kritieke hitte vloed in die heliese spoel was aanvanklik gekwantifiseer met behulp van die empiriese korrelasie van Ünal. *CFD* was gebruik om die presiese ligging van die *CHF* te voorspel as gevolg van die een-dimensionaliteit van die Ünal model en die gekompliseerde vorm van die heliese spoel. 'n Enkel-fase numeriese simulasie gevolg deur 'n twee-fase vloei analise met behulp van die Rensselaer Polytechnic Institute (RPI) muur hitte vloed verdeling model was gebruik om die ligging en grootte van die *CHF* te bepaal en die resultate was vergelyk met dié van die Ünal model. Daar was bevind dat die Ünal model die ligging van die *CHF* met ongeveer 37 % onderskat.

TABLE OF CONTENTS

LIST OF FIGURES

LIST OF TABLES

NOMENCLATURE

Acronyms

BBSA	Black body surface area
CFD	Computational fluid dynamics
CHF	Critical heat flux
DNB	Departure from nucleate boiling
GCV	Gross calorific value
HP	High pressure
IAPWS	International association for properties of water and steam
LP	Low pressure
NCV	Nett calorific value
NEWF	Non-equilibrium wall function
ONB	Onset of nucleate boiling
PBM	Population balance model
RANS	Reynolds averaged Navier-Stokes
RNG	Renormalization group
RPI	Rensselaer Polytechnic Institute
SIMPLE	Semi-implicit method for pressure-linked equations
SIMPLEC	SIMPLE-Consistent
SST	Shear stress transport
VOF	Volume of fluid
1D	One-dimensional
3D	Three-dimensional

Uppercase Letters

A	Area [m^2]
A_0, A_s	Empirical constants used in realizable k-ε model [-]
C	Carbon [-]; coefficient [-]
$C_{\varepsilon 1}$, $C_{\varepsilon 2}$, $C_{\varepsilon 3}$,	Empirical constants used in k-ε turbulence models [-]
C_1, C_2,	Empirical constants used in realizable k-ε model [-]
D	Coil diameter [m]
E	Empirical constant for log-law of the wall [-]
F	Dimensionless factor [-]; force [N]
G	Gas mass flux [kg/m^2 s], turbulence production rate [-]
G_u	Grit pick-up [-]
H	Enthalpy [J/kg]

K	Coefficient for determining vapour mass fraction [-]; empirical constant for area of influence [-]
L	Boiler load as percentage of full load [-]; length [m]
N	Nucleation site density [m^{-2}]
P	Pressure [Pa]
Q	Nett heat [J/kg]; interphase energy exchange term [-]
R	Additional term in RNG k-ε model [-]; interfacial drag force [N]
S	Tube pitching [-]; source term [-]
T	Temperature [^oC]
U	Uniformity index [mm], constant for realizable k-ε model [-]
X	Percentage of coal smaller than 1 mm
Y	Percentage ash in coal [-]

Lowercase Letters

a	Dimensionless transverse pitch [-], model constant for Kader's blending function [-]
b	Dimensionless longitudinal pitch [-], model constant for Kader's blending function [-]
c	Specific heat at constant pressure [J/kg ^oC]
d	Tube diameter [m]; bubble diameter [m]
f	Friction factor [-], bubble departure frequency [s^{-1}]
f_a	Tube arrangement factor for in-line tubes [-]
g	Gravitational acceleration [m/s^2]
h	Heat transfer coefficient [W/m^2 K]
k	Thermal conductivity [W/m K], turbulent kinetic energy [m^2/s^2]
m	Mass flowrate [kg/s]
p	Coil pitch [m]
q	Heat transferred [W]
t	Time [s]
u	Velocity component [m/s]
$\bar{u}$	Time-mean velocity in x-direction [m/s]
u^+	Non-dimensional velocity [-]
w	Mean gas velocity gas free area [m/s]
w_a	Gas velocity gas free area [m/s]
x	Cartesian coordinate [m]; vapour mass fraction [-]
y	Cartesian coordinate [m]
y^+	Non-dimensional distance from the wall [-]

Greek Letters

α	Volume fraction [-]
β	Empirical constant for RNG k-ε model [-]
Γ	Thermal diffusion [-], Kader's blending function [-]
γ	Evaluation factor for transition region [-]
Δ	Indicates a differential, e.g. $\Delta T = T_2 - T_1$
δ	Tube thickness [m]
δ_{ij}	Kronecker delta [-]
ε	Emissivity [-]; turbulent dissipation rate [m^2/s^3]
ε_m	Eddy diffusivity for momentum transfer [m^2/s]
η	Kinematic viscosity [m^2/s]
θ	Equilibrium contact angle [deg]
κ	Von Karman constant [-]
μ	Dynamic viscosity [Pa s]
ξ	Friction factor [-]
ρ	Density [kg/m^3]
σ	Stephen-Boltzmann constant [$W/m^2 K^4$], surface tension [N/m^2]
τ	Viscous shear stresses [N/m^2]
Ψ	Area correction factor [-]

Superscripts

b	Bubble-induced
eff	Effective
m	Coil geometric factor
t	Turbulent

Subscripts

ai	Adiabatic
am	Ambient air
b	Buoyancy; bubble
bw	Bubble wall departure
c, conv	Convective
cond	Condensation
cr	Critical
D	Coil diameter; interfacial drag
e	Furnace exit; evaporation
eff	Effective
e_1, e_2	Refer to furnace geometry and emissivity, respectively

f	Fuel; fluid
fg	Evaporation/ boiling
g	Gas; gravitational acceleration
h	Enthalpy
ha	Hot air
i	Inner; inside
ic	Inner coil
ici	Inner coil - inside
ico	Inner coil - outside
if	Interface
in	Input; inlet
k	Turbulent kinetic energy term
L	Longitudinal; lift
l	Laminar flow; liquid
m	Mass flow; mean
mi	Shell mean inside diameter
nw	Near-wall
o	Outside
oc	Outer coil
oci	Outer coil - inside
oco	Outer coil - outside
out	Outlet
p	Pressure; phase p
pq	Refers to exchange between phase p and q and vice versa
q	Quenching; phase q
rad	Radiation
sat	Saturation; superheating of liquid
sub	Liquid subcooling
T	Transverse
t	Turbulent flow
td	Turbulent dispersion
vm	Virtual mass
w	Tube wall
wl	Wall lubrication

1 INTRODUCTION

1.1 Background

Data published by Statistics South Africa (Stats SA) on the national electricity consumption for 2014 highlighted a 1.4% decline in the amount of electricity being produced in South Africa (Electricity produced and available for distribution, [S.a]). De Vos (2014) further adds to this sentiment by stating that the frequent load shedding in South Africa is a clear indication that the country is experiencing a critical electricity generating shortfall. This coupled with the country's population density growth and delays by the national energy provider to bring new power plants online clearly suggest that this situation will not improve in the short to medium term.

The country's prevailing electrical power supply shortfall is driving major price increases in electricity with more increases to come over the next few years. This together with the uncertainty in reliable electricity supply sparks interest in smaller cogeneration plants where industrial customers will be able to generate electricity for their own consumption whilst producing steam for process equipment. In lieu of the ongoing energy crisis in South Africa, many industrial manufacturers are investigating the possibility of generating their own electrical power.

The layout of a typical power island is based on the Rankine cycle which includes a turbine generator set of the back pressure or condensing type, which are typically fitted downstream of the boiler. Back pressure turbines allow the user to extract steam at a predetermined pressure at the turbine exit for use in downstream processes, whilst condensing turbines exhaust the rejected energy to atmosphere. These turbines convert kinetic energy into electrical energy by means of an alternator. Back pressure steam turbines, which are readily available from various turbine manufacturers, require high pressure superheated steam in order to extract the maximum available enthalpy from steam whilst still producing relatively dry steam at the turbine outlet.

The design pressure rating of the current range of John Thompson shell boilers, see Figure 1.1, are limited by geometrical and code design constraints on the boiler shell and furnace. The maximum design pressure for a standard John Thompson shell boiler is restricted to approximately 20.5 bar. In order to overcome the design limitations of shell boilers and the high capital investment associated with water tube boilers, John Thompson is currently developing a high-pressure helical coil steam boiler able to generate saturated and superheated steam. The coil boiler will either be coal or waste fuel fired and will be aimed at both local and international markets.

Figure 1.1: John Thompson Europac TU2100 packaged coal-fired shell boiler

1.2 A Review of Helical Coil Steam Generators

Helically coiled boilers are traditionally fired using automatic forced draught burners. Commercially available steam generators are capable of ramping from cold start-up to maximum steaming rate in approximately 5 to 6 minutes when coupled to a forced draught oil-or gas-fired burner. The forced draught burners used are capable of instantaneously shutting down the boiler heat source in order to protect the boiler tubes in the event of loss of water. These relatively small boilers typically range from 15 to 225 kWth (Clark, 1999: 1). Other commercially available steam generator sizes are presented in Table 1.1.

Table 1.1: Comparison of oil-and gas-fired steam generators

Make of Steam Generator	Steam Evaporation [kg/hr]	Thermal Output [kW]	Operating Pressure [bar]
Thermal Fluid Systems	610 - 11158	235 - 1114	0 - 90
Vapor Power International	281 - 4695	177 - 2943	103 - 214
Thermogenics Inc.	1173 - 9389	733 - 5887	1 - 34
TT Boilers (AB & Co.)	80 - 4000	104 - 1800	3 - 190
Clayton Boilers	235 - 2897	98 - 1815	13 - 58
Gekanonus	711 - 13121	290 - 5350	8 - 90

Helically coiled steam generators can be divided into two types, namely circulating or once-through boilers. In the circulating helical coil boilers water is circulated between a steam drum and the helical coil evaporator at several times the steaming rate of the boiler. For the once-through boiler on the other hand, approximately 90% of the water is converted to steam with the other 10% either being blown down or re-used. Both types of helical boilers are capable of producing saturated steam with a dryness fraction in excess of 0.99 (Clark, 1999: 1).

1.3 A Review of Helically Coiled Tube Heat Exchanger Research

Heat exchangers incorporating helically coiled tubes are used in various applications and industries; these include amongst others power generation, steam generation, nuclear, industrial process plants, heat recovery systems, refrigeration plant, and food industry.

1.3.1 Water/steam Side Heat Transfer

Numerous studies have reported increased heat transfer in helically coiled tubes when compared to straight tubes. Studies by Jayakumar et al (2008: 221) employed empirical correlations and computational fluid dynamics (CFD) to quantify the increase in heat transfer and the corresponding pressure drop for single-phase fluid flow in helically coiled tubes. A significant outcome of their study was a modified Nusselt number correlation for the tube side heat transfer coefficient when taking the fluid to fluid heat exchange into consideration. Jayakumar et al (2008: 221) contributed the enhancement in heat transfer in a helical coil tube to the complex flow pattern which exists within the helical coil.

Elsayed et al (2014: 1) numerically investigated the combined effect of helical coils and nanofluids on the heat transfer characteristics and pressure drop within the turbulent flow regime. Results from the study indicated a 30% increase in the heat transfer coefficient when compared to that of water inside a straight tube at the same Reynolds number. The heat transfer coefficients obtained from CFD was reported against published experimental data and empirical correlations, and was in good agreement with both.

Detailed flow and heat transfer patterns within a syngas cooler consisting of a series of concentric helical coils were analysed for various process loads using CFD by Oh et al (2014: 2136). Oh et al commented that: “Results of the study was not directly validated by operational data and that the use of CFD for helical coil heat exchangers has been proven to have reasonable agreement with experiments.” Overall results from Oh et al’s process model agreed well with the CFD results for different load cases with an error of approximately 5-7% being reported between results for the “as new, clean” condition.

Inaccurate CFD heat transfer coefficients may be predicted for helical coils when constant values are used for the heat transfer medium’s thermal and transport

properties (Jayakumar, 2012: 337). The characteristics of non-isothermal fluid flow and heat transfer under turbulent flow conditions of single-phase water within a helical coil was studied by Jayakumar using CFD. For the boundary conditions of constant wall temperature and heat flux the results suggested a match in the velocity profiles and a mismatch in the temperature profiles. Further studies by Jayakumar to estimate the inner heat transfer coefficient for two-phase flow inside a helical coil by modifying the void fraction and velocity of the air-water mixture reported a decrease in heat transfer coefficients with an increase in the void fraction. Jayakumar (2012: 337) found that coil parameters such as coil pitch circle diameter (PCD), coil tube diameter and the medium inlet void fraction had a significant effect on the heat transfer and pressure drop for two-phase flow conditions.

Raj et al modelled three-dimensional (3D) flow within the Fluent laboratory to simulate the anisotropic flow properties which result from the complex turbulent flow phenomena within a helical coil. Implementing the blending function of the Shear Stress Transport (SST) k-ε turbulence model to replicate the standard k-ε model in the fluid main stream and the standard k-ω model near the boundary wall, heat transfer and flow parameters were optimised by varying the coil pitch (Raj *et al*. 2014: 300).

Turbulent two-phase flow of a dispersed air-water mixture in helical coils using a CFD-Population Balance Model (PBM) approach to model the size distribution of poly-dispersed air produced by the coalescence and breakup of bubbles was done by Rahimi et al (2014: 562). Modelling done studied different two-phase flow modelling schemes including a combination of the SST and k-ε turbulence models coupled with bubble distribution. Results indicated that the secondary flow encountered in helical coils influenced the two-phase fluid flow in the helical coil by encouraging bubble aggregation which results in a radial pressure gradient that concentrates air bubbles towards the inner side of the pipe walls. Rahimi et al suggests that the use of helical coils in steam boilers may be limited by the fact that the inner side of the coil is concentrated with air/vapour. In helical coil steam generators the orientation and low velocity of the air/vapour volume fraction in two-phase flow can make the tubes prone to unexpected failure by overheating of the inner tube wall (Rahimi *et al*. 2014: 570).

1.3.2 Gas Side Heat Transfer

Existing empirical correlations for gas side heat transfer coefficients between concentric helical coils result in large errors with an increase in the gap size (Kharat *et al*, 2009: 1). Physical permutations such as tube diameter, coil diameter and coil gap makes an experimental evaluation of helical coil outside heat transfer performance expensive and time-consuming. Using CFD Kharat et al reported a 117% error between heat transfer using the tube bank correlation and CFD. A modified Nusselt correlation for outside heat transfer coefficient using CFD was suggested by Kharat et al. An overall error of approximately 7% was reported

between results obtained from the modified *Nu* correlation and that from the original CFD.

1.4 Purpose of the Project

The purpose of this project was to design a high-pressure helical coil steam boiler able to generate saturated and superheated steam. The coil boiler either had to be coal or waste fuel fired and would be aimed at both local and international markets. The final conceptual design includes detailed 3D CAD models and two-dimensional (2D) manufacturing drawings of the prototype boiler.

1.5 Objectives of the Project

The objective of this work was to first formulate a one-dimensional (1D) steady-state thermal model, using known empirical heat transfer correlations, which could be used to determine the required heat transfer areas of the helically coiled boiler. Secondly, to determine the geometry of the helically coiled boiler capable of producing 10 tonnes per hour of superheated steam at 45 bar and 380 ^{o}C, and produce manufacturing drawings in order to fabricate the prototype boiler. It was also important to characterise the thermal-fluid flow behaviour inside the coiled tubes in order to quantify the effect of the centrifugal force on the expected single-phase and two-phase flow. Other objectives included:

- Estimating the location of the boiling crisis and determination of the minimum boiler circulation rate.
- Sizing the furnace to ensure that the boiler is able to burn woody biomass, waste fuels and coal.
- Ensuring that the boiler design complies with the following design specifications:
    - Must utilise the John Thompson Triumph TT1050 chaingrate stoker.
    - Have a maximum transport mass of 32 tonnes to allow transport on a 40 foot flat rack.
    - The design should allow it to be offered as a packaged unit complete with matching turbine generator set.
    - The maximum transport height of the boiler must be 3.5m.
- The boiler design must be capable of handling varying electricity demands.
- The boiler design must ensure safe operation of the boiler under normal and abnormal operating conditions.
- The steam produced should be 99% dry.
- The design should prevent overheating of the boiler tubes.
- Gas side pressure drop should be restricted to 200 Pa.
- Steam side pressure drop should not exceed 500 kPa.

1.6 Project Scope and Limitations

The work done in this project was primarily concerned with the thermal design of a helically coiled boiler. CFD was used as a complimentary design tool in order to characterise the thermal hydraulic fluid behaviour inside the tubes of the helically coiled boiler.

The design does not cover experimental validation of the CFD results. Instead, CFD results are validated against known empirical correlations and experimental data available in open literature. The ANSYS Fluent academic licence utilised for the numerical simulations had a computer memory limitation of 1 million cells. Therefore only two coils of the helically coiled boiler was modelled and presented in this thesis.

1.7 Research Methodology

In order to achieve the goals of this research and development project, the methodology listed below was followed:

- Identify a proven empirical correlation used for sizing of helically coiled heat exchangers and formulate a 1D steady-state thermal model using the selected correlation.
- Determine the heat transfer area needed for the required boiler operating conditions. This would define the geometry of the helical coil boiler, hence the boiler evaporation and superheater performance.
- Establish the critical heat flux of the evaporator and determine the required boiler circulation rate using empirical correlations.
- Create a 3D model of the helical coil boiler and generate manufacturing drawings from which the prototype boiler could be fabricated.
- Conduct CFD investigations in order to determine the heat transfer and fluid flow characteristics of the steam-water mixture within the helical coils.
- Validate the CFD model against results obtained from empirical correlations and define conditions for the onset of critical boiling states using CFD and correlations.
- Refine the helical coil boiler geometry using results obtained from the CFD analysis

1.8 Problem Statement

The design of solid fuel fired, high pressure, helically coiled boilers producing superheated steam pose an array of technical and engineering challenges to the designer. One of the most significant constraints of a solid fuel fired coil boiler is the system's inability to protect the evaporator tubes against overheating by the heat source in case of abnormal conditions. The conditions for the onset of the 1st critical (departure from nucleate boiling) and 2nd critical (post dry-out) boiling states within the helical boiler should therefore be fully understood by the designer in order to eliminate or mitigate the effects thereof.

2 1D STEADY-STATE THERMO-FLUID MODEL

2.1 Combustion Heat Balance

The fundamental thermal design of the helical coil boiler is governed by the 1st law of thermodynamics, which states that the energy input or heat supplied must equal the energy output. In boiler systems the energy sources include the sensible heat of the combustion air and boiler feed water, the calorific value of the fuel, the heat of the reactants and the heat of the exothermic reactions. This energy is then transformed to heat energy in steam, sensible heat in the products of combustion (flue gas) and losses leaving the system.

In the applicable furnace heat balance the total nett heat input into the furnace must equal the heat absorbed by the furnace walls and the heat carried by the gas into the convection passes (Magasiner, 1966: 34).

$$Q_{in} = Q_{rad} + Q_{conv} \tag{2.1}$$

The nett heat input into the furnace is depicted by the exothermic combustion of coal on the chaingrate stoker as illustrated in Figure 2.1, and is of the following form:

$$Q_{in} = NCV\left(1 - C_{loss}\right) + m_{ha}\left(c_{ha}T_{ha} - c_{am}T_{am}\right) \tag{2.2}$$

$$Q_{in} = NCV\left(1 - C_{loss}\right) \tag{2.3}$$

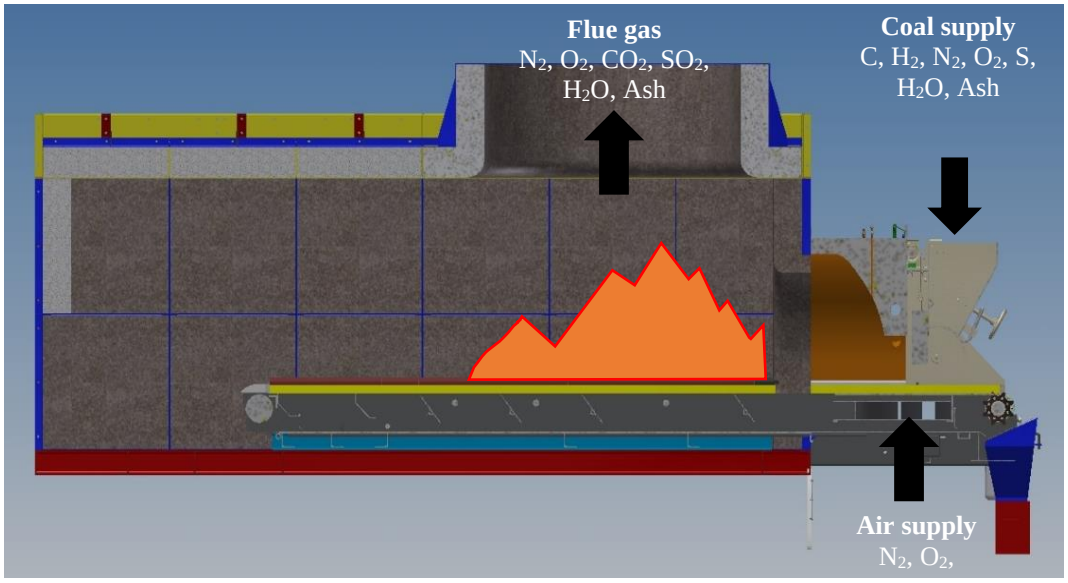

Figure 2.1: Sectional view of refractory lined furnace

Equation (2.3) is the final form used for determining the nett heat input into the furnace in the absence of air pre-heating being considered in the boiler design. The heating value of the fuel used in the calculations is characterised in terms of the Nett Calorific Value (NCV), which is the amount of heat released by complete combustion of 1kg of fuel at a reference state of 100 ^{o}C for the products of combustion, and is determined by a bomb calorimeter. Consult Appendix A for a typical fuel analysis of the South African Grade C-Smalls coal used in the conceptual boiler design.

The carbon loss, C_{loss}, in equations (2.2) and (2.3) depict the percentage unburnt carbon which is entrained in the bottom and fly ash. Its magnitude; which is a function of stoker combustion characteristics such as ash and grits produced, and the carbon content thereof; can be calculated using the following John Thompson correlations;

$$C_{loss} = C_{ash} + C_{grit} \tag{2.4}$$

where:

$$C_{ash} = Y\left(1.0082 + 0.1417U - 0.0039U^2 - 0.053X\right)\left(2.235 - 3.708L + 2.473L^2\right) \tag{2.5}$$

$$C_{grit} = 23.13 + 4.021X - 0.150X^2 \tag{2.6}$$

$$G_u = \left(0.0807 + 0.5657X\right)\left(1.2142L - 0.21426L^2\right) \tag{2.7}$$

In equations (2.5) to (2.7) above Y is the percentage ash in coal, U is the uniformity index (the ratio at which 60% and 10% of coal pass through a selected sieve size), X is the percentage of coal which is smaller than 1 mm, L is the percentage boiler load and G_u is the percentage grit pick-up.

Derivation of the above correlations is based on data from 20 performance acceptance tests as well as tests done on the development boiler at the John Thompson Boiler Development Centre. De Kock (1986: 12) states that results obtained by using these correlations are reasonably accurate and feasible when taking scatter observed during the tests into consideration. The variables referenced in the above equations are functions of the coal properties and include provision for the percentage ash and fines in the coal, the size grading of the coal and the stoker load.

Combustion kinetics for the combustion of solid fuels such as reaction rates, residence time, devolatization, charring, and gasification are not taken into account in the simple combustion model used in the thermal model.

2.2 Heat Transfer by Radiation

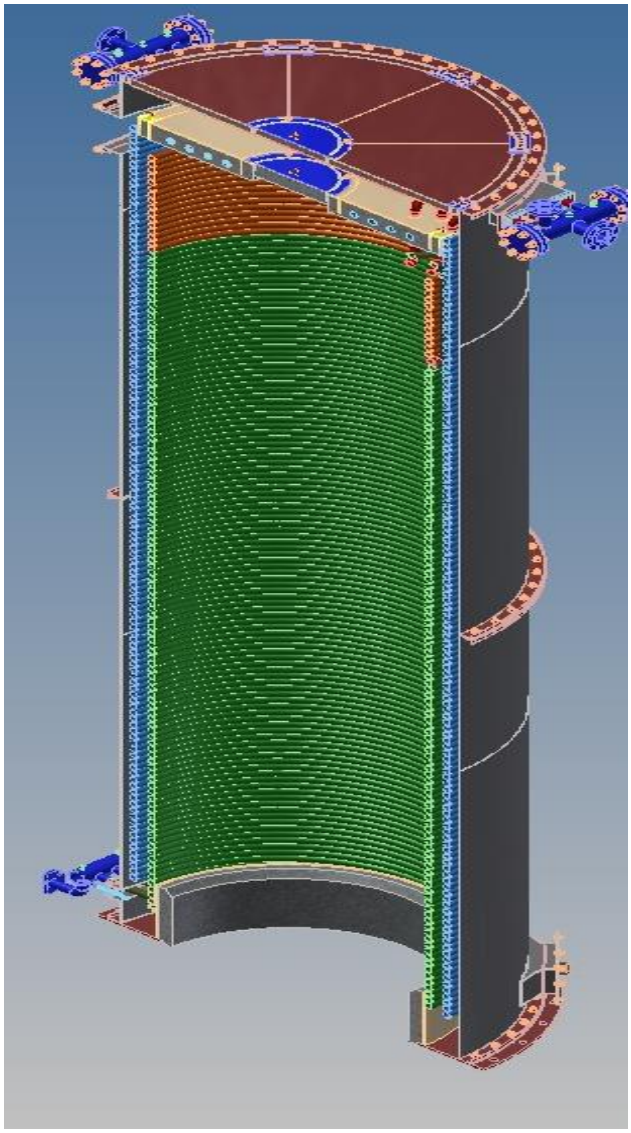

Figure 2.2: Radiant heat transfer areas
- Evaporator (Accounted for in model)
- Superheater (Unaccounted for in model)

Figure 2.2, shown above, indicates radiant heat transfer areas accounted for in the boiler design. Radiation is described as the transfer of heat energy by a body to its surroundings by means of electromagnetic waves. Heat transferred by radiation, q_{rad}, is mathematically expressed by the Stephan-Boltzmann law as:

$$q_{rad} = \sigma A \left(T_1^{\,4} - T_2^{\,4} \right) \tag{2.8}$$

In the foregoing equation it is assumed that the heat source and the heat sink are both black bodies and that the emissivity of both is unity. The Stephan-Boltzmann relationship above must therefore be corrected for a boiler surface, since the emissivity of the combustion flame and the furnace walls are not equal to unity in a boiler. The corrected relationship can be written as:

$$q_{rad} = \sigma A F_{e1} F_{e2} \left(T_1^{\,4} - T_2^{\,4}\right) \tag{2.9}$$

Where F_{e1} is a dimensionless geometric factor and F_{e2} is a dimensionless emissivity factor, which for boiler furnaces can be combined into a single correction factor for geometry and emissivity, ε. The combination of refractory lined (Figure 2.1) and water cooled furnace (Figure 2.2) walls utilised in the furnace design absorb the radiant heat emitted by the luminous products of combustion. The amount of heat transferred by radiation can therefore be presented by the following relationship:

$$q_{rad} = \frac{20.53\,BBSA\;\varepsilon}{m_f}\left(T_{fg}^{\,4} - T_w^{\,4}\right) \tag{2.10}$$

$$q_{rad} = \frac{20.53\,BBSA\;\varepsilon}{m_f}\left(T_e^{\,4} - T_w^{\,4}\right) \tag{2.11}$$

The real flame temperature represented by T_{fg} is only true if the mass of hot gas acts as a black body. Since it is difficult to accurately determine the effect of microscopic black particles and reradiating refractory walls on emissivity the calculations are simplified by setting T_{fg} equal to the furnace exit gas temperature. This results in a higher emissivity value being calculated compared to the value obtained when using the mean radiating furnace temperature. Calculations using this assumption will result in a ± 3.5% error in the final gas temperature (Magasiner, 1966: 34).

2.3 Heat Transfer by Convection

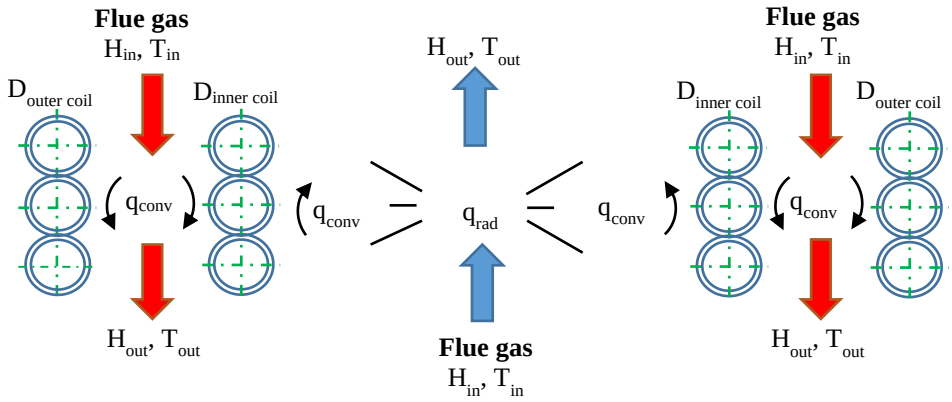

Figure 2.3: Heat transfer areas in boiler convective passes

Convective heat transfer within the helical coil boiler convection passes, as illustrated in Figure 2.3, occur due to the motion imparted on the flue gas mass by the externally mounted induced draught fan. The resultant heat flux is a function of the fluid to wall temperature differential and the fluid velocity and temperature profiles. It is expressed as;

$$q_{conv} = h\left(T_{in} - T_{out}\right) \tag{2.12}$$

The major factors influencing the heat transfer coefficient, *h*, of a flue gas flowing at a constant mass flowrate is velocity, density, specific heat, thermal conductivity and viscosity of the gas as well as the outside diameter of the tube. The formation of a stagnant fluid layer on the tube wall resisting heat transfer as well as fluid mixing within a tube is influenced by previously mentioned fluid and geometric properties. The relationship between these variables are found by dimensional analysis as shown in the following expression:

$$\frac{hD}{k} = A\left(\frac{DG}{\mu}\right)^{a}\left(\frac{c\mu}{k}\right)^{b} \tag{2.13}$$

From the above equation dimensionless groups for the Nusselt, Reynolds and Prandtl numbers are found as follows:

$$Nu = \frac{hD}{k} \tag{2.14}$$

$$Re = \frac{DG}{\mu} \tag{2.15}$$

$$Pr = \frac{c\mu}{k} \tag{2.16}$$

For forced convective heat transfer combining the above dimensionless groups results in the formulation of the heat transfer coefficient by correlations of the following form:

$$Nu = f\left(Re, Pr\right) \tag{2.17}$$

The convective heat transfer coefficient described in equation (2.12) is obtained from the dimensionless Nusselt number, equation (2.17). Correlations for the Nusselt numbers for various flow and heat transfer configurations have been experimentally determined by others.

According to Gnielinski (2010: 725), for the mean Nusselt number of a single pipe in crossflow, the following equation holds true;

$$Nu = 0.3 + \left(Nu_l^2 + Nu_t^2\right)^{1/2} \tag{2.18}$$

Gnielinski's correlation is also applicable for rows of in-line tubes with the introduction of a Reynolds number which is calculated using a mean velocity and a tube arrangement factor, which is a function of the tube layout. The modified Reynolds number compensates for the complex nature of flow across a tube bank, which involves boundary layer separation on each tube and interactions of the resulting wakes with adjacent wakes and downstream tubes (Mills, 1995).

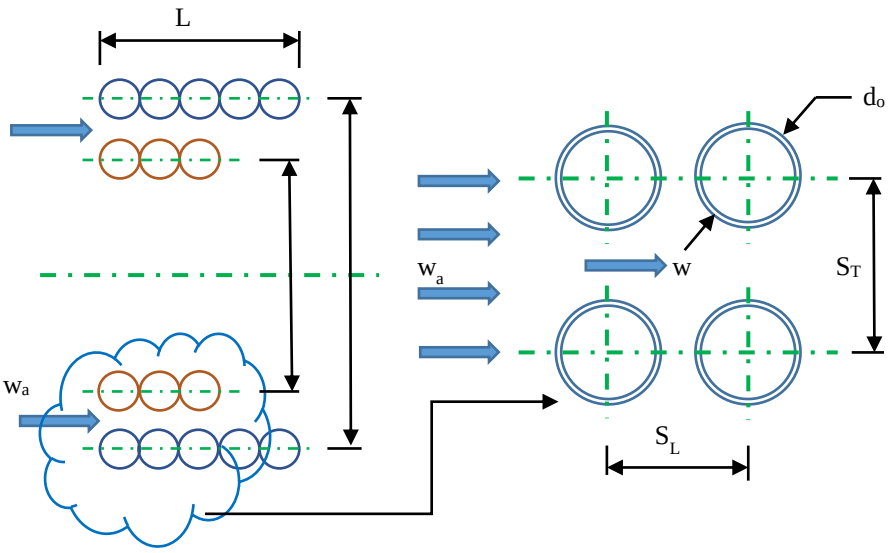

Figure 2.4: Tube arrangement and effective velocities for inline helical tubes

The tube arrangement factor for in-line tubes, see Figure 2.4 above, is computed as follows:

$$f_a = 1 + \frac{0.7\left(b/a - 0.3\right)}{\psi^{1.5}\left(b/a + 0.7\right)^2} \tag{2.19}$$

In equation (2.19) the dimensionless transverse pitch is defined as $a = S_T/d_o$, the dimensionless longitudinal pitch as $b = S_L/d_o$ and the area correction factor (ψ) as;

$$\psi = 1 - \frac{\pi}{4a} \qquad \text{for } b \geq 1$$

$$\psi = 1 - \frac{\pi}{4ab} \qquad \text{for } b < 1$$

The closed spacing of the coils in a helically coiled boiler approaches that of a circular flat plate. The Nusselt number correlation for laminar flow across flat plates proposed by Pohlhausen can therefore be used for determining the heat transfer coefficient for laminar flow conditions (Stephan, 2010: 25).

$$Nu_l = 0.664\sqrt{Re}\,\sqrt[3]{Pr} \tag{2.20}$$

For turbulent flow conditions, Reynolds number greater than 5×10^5, the Nusselt number correlation takes the following form (Gnielinski, 2010: 725);

$$Nu_t = \frac{0.037\,Re^{0.8}\,Pr}{1 + 2.443\,Re^{-0.1}\left(Pr^{2/3} - 1\right)} \tag{2.21}$$

The flue gas properties for the determination of the heat transfer coefficient is evaluated at the mean gas temperature, which is the average of the tube wall temperature and the flue gas bulk temperature.

2.4 Flue Gas Flow Paths

In the helically coiled boiler flue gas flows upwards from the combustion chamber into the inner coil which forms the first gas pass. In the second gas pass the flue gas flows downwards inside the annular gap created by the inner and outer coils. Upon reaching the baseplate of the boiler the flue gas changes direction and flows upwards on the outside of the outer coil, which forms the third gas pass. See Figure 2.5 for a graphical representation of the flue gas passes within the helical coil boiler.

2.5 Water/steam Flow Paths

The helical coil boiler is constructed out of two water or steam filled helically coiled tube units, namely the inner and the outer coil sections. The outer helical coil section, also referred to as the economiser, contains liquid water and consists of four individual tube starts. The inner coil section consists of two parts; an evaporator portion which contains a mixture of saturated water and steam, and a superheater section which transforms the saturated steam to superheated steam. The saturated steam-water mixture from the evaporator is passed through a steam separator to ensure that only dry steam enters the superheater portion. See Figure 2.5 for an indication of the water/steam flow paths.

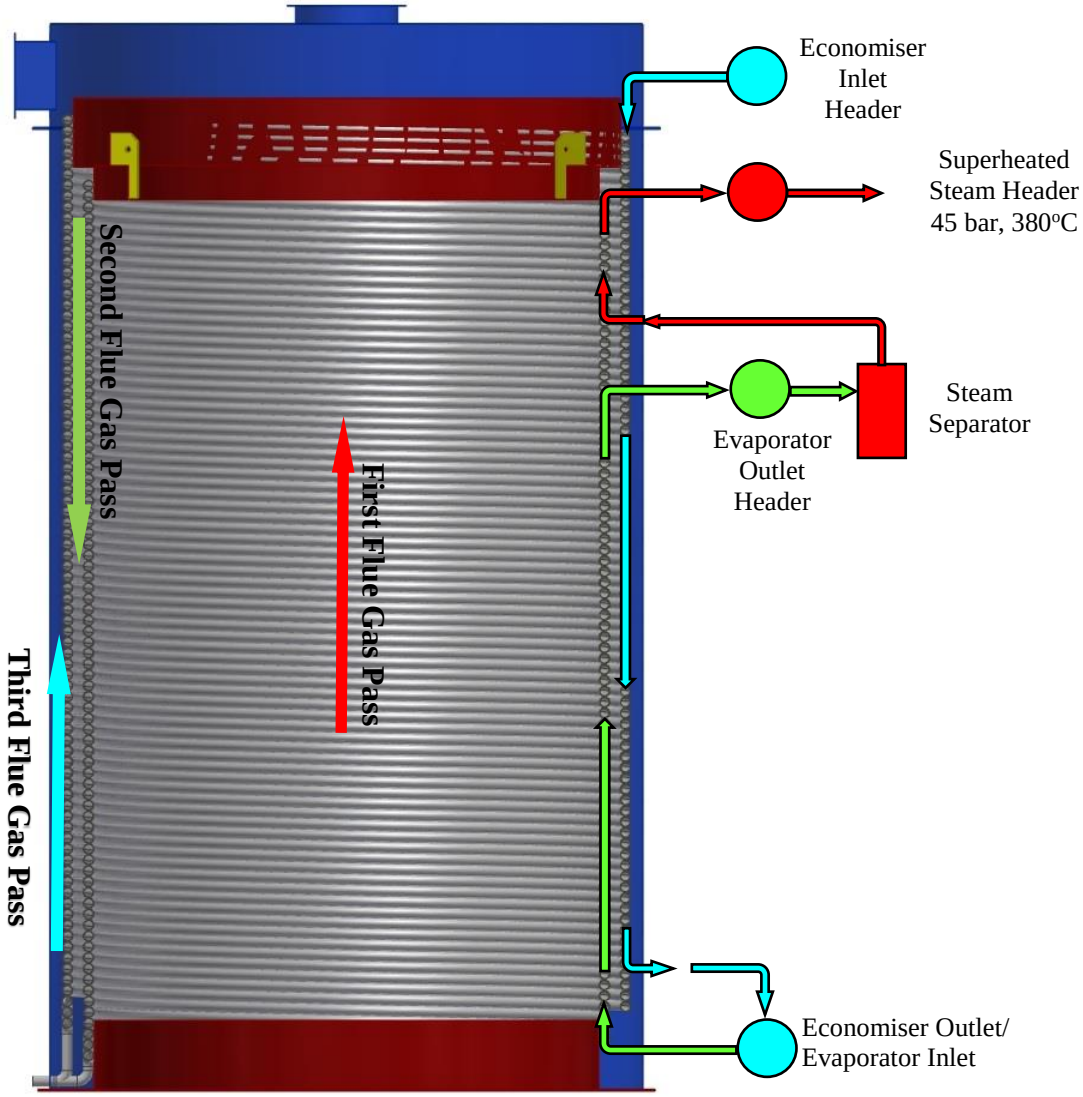

Figure 2.5: Coil boiler gas and steam/water paths

2.6 Single-phase Heat Transfer in Helically Coiled Tubes

Fluid flow inside helically coiled tubes is characterised by a pair of symmetric vortices which result from the secondary flow created by the presence of centrifugal forces within a fluid flowing through a curved pipe, see Figure 2.6. The magnitude of the centrifugal force is dependent on the axial velocity of the fluid particles and the coil radius of curvature (Jayakumar, 2012: 312). Fluid particles at the pipe wall are exposed to lower centrifugal forces due to the tube wall effects. The unequal velocity distribution within the helical coil tube results in fluid flowing at the core being pushed towards the outer tube wall. This results in the maximum fluid velocity being shifted towards the side of the tube.

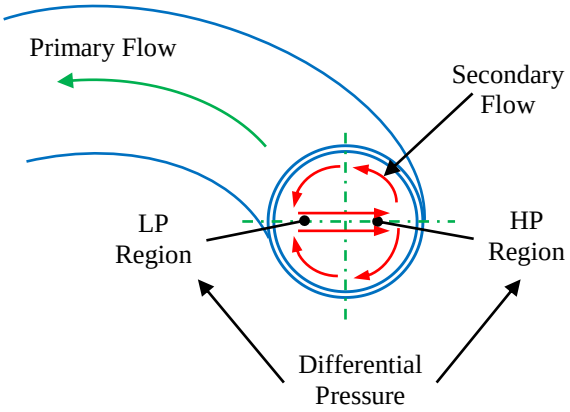

Figure 2.6: Section through coil illustrating secondary flow

The additional fluid transport created by the secondary flow significantly improves the heat transfer between the fluid and the tube wall. The effect of the secondary flow on heat transfer is influenced by the coil curvature ratio in the form (*d/D*), see Figure 2.7. Coil curvature increases the critical Reynolds number within a helical coil tube by suppressing turbulent fluctuations and smoothing the emergence of turbulence (Jayakumar, 2012: 312).

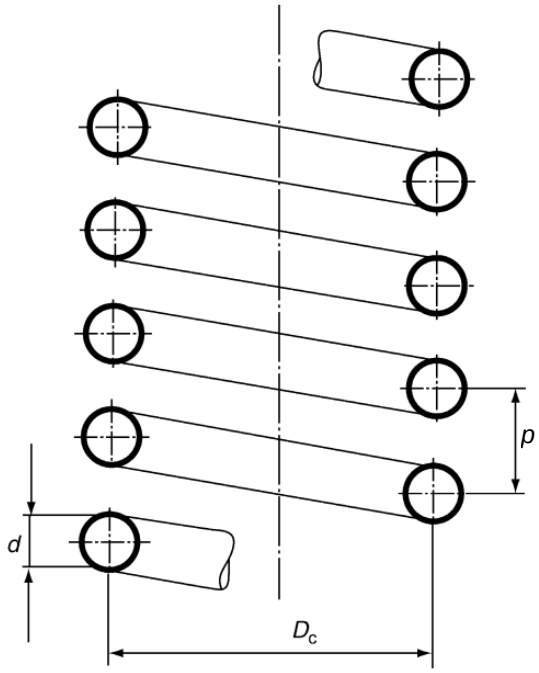

Figure 2.7: Geometry of a helical coil showing critical dimensions. (Gnielinski, 2010: 710)

For laminar flow inside a helical coil tube, $Re < Re_{cr}$, Gnielinski (2010: 710) proposed that the Nusselt number be calculated as;

$$Nu_l = 3.66 + 0.08\left[1 + 0.8\left(\frac{d}{D}\right)^{0.9}\right] Re^m \, Pr^{1/3} \left(\frac{Pr}{Pr_w}\right)^{0.14} \tag{2.22}$$

where $m = 0.5 + 0.2903\,(d/D)^{0.194}$

The critical Reynolds number, Re_{cr}, referenced above is a function of the coil curvature ratio and indicates the transition from laminar to turbulent flow in helical coil tubes. Determination of the critical Reynolds number according to Schmidt is;

$$Re_{cr} = 2300\left[1 + 8.6\left(\frac{d}{D}\right)^{0.45}\right] \tag{2.23}$$

The Nusselt number for turbulent flow is computed using heat transfer theory for the fully developed flow region, which for helically coiled tubes exist at $Re > 2.2\times10^4$ (Gnielinski, 2010: 710).

$$Nu_t = \frac{(\xi/8) Re\, Pr}{1 + 12.7\sqrt{\xi/8}\,\left(Pr^{2/3} - 1\right)} \left(\frac{Pr}{Pr_w}\right)^{0.14} \tag{2.24}$$

Where ξ is the friction factor for helically coiled tubes given by Mishra and Gupta as (Gnielinksi, 2010: 710):

$$\xi = \left[\frac{0.3164}{Re^{0.25}} + 0.03\left(\frac{d}{D}\right)^{0.5}\right]\left(\frac{\eta_w}{\eta}\right)^{0.27} \tag{2.25}$$

For the transition region, $Re_{cr} < Re < 2.2\times10^4$, Gnielinski demonstrated that the Nusselt number can be determined using linear interpolation and proposed the use of the following equation for calculating the Nusselt number.

$$Nu = \gamma\, Nu_l + (1 - \gamma) Nu_t \tag{2.26}$$

where γ is an evaluation factor determined by

$$\gamma = \frac{2.2\times10^4 - Re}{2.2\times10^4 - Re_{cr}} \tag{2.27}$$

2.7 Two-phase Heat Transfer in Helically Coiled Tubes

The ideal flow boiling states in the tubes of a helical coil boiler should preferably range between subcooled and nucleate boiling. Subcooled boiling is expected in the economiser section where the temperature differential between the tube wall and the bulk fluid is small. For the evaporator section on the other hand, nucleate boiling is preferred. This is due to the associated large increases in heat transfer rates for moderate changes in surface temperatures.

The categorisation of the flow regime in multiphase flow is analogous to the identification of laminar or turbulent flows in single-phase flow. Multiphase flow patterns such as separated, mixed or dispersed flow describe the distribution of the liquid and vapour phases. In separated flows there exist a distinct boundary between the liquid and the vapour phase, whilst for dispersed flow in heating applications vapour in the form of steam bubbles is distributed within the liquid phase.

The increase in heat transfer as a result of the motion imparted by the vapour bubble formation during nucleate boiling is ignored in the 1D steady-state boiler design.

2.7.1 Critical Heat Flux (CHF) in Vertical Tubes

Safety margins between the subcooled and nucleate boiling regime, and the boiling crisis are utilised in flow boiling heat transfer to avoid mechanical damage to tubes. These safety margins are determined for various multiphase flow regimes by the introduction of two parameters, namely ΔT_{sub} and ΔT_{sat}, which respectively represent the liquid subcooling and the wall superheat.

These quantities are calculated as follows;

$$\Delta T_{sub} = T_{sat} - T_f \text{ , and} \tag{2.28}$$

$$\Delta T_{sat} = T_w - T_{sat} \tag{2.29}$$

The boiling curve, which is the ratio of wall heat flux to wall superheat, is typically used in boiling heat transfer to quantify the underlying physical mechanisms. Wall superheat is used to identify different boiling regimes in the boiling curve, see Figure 2.8.

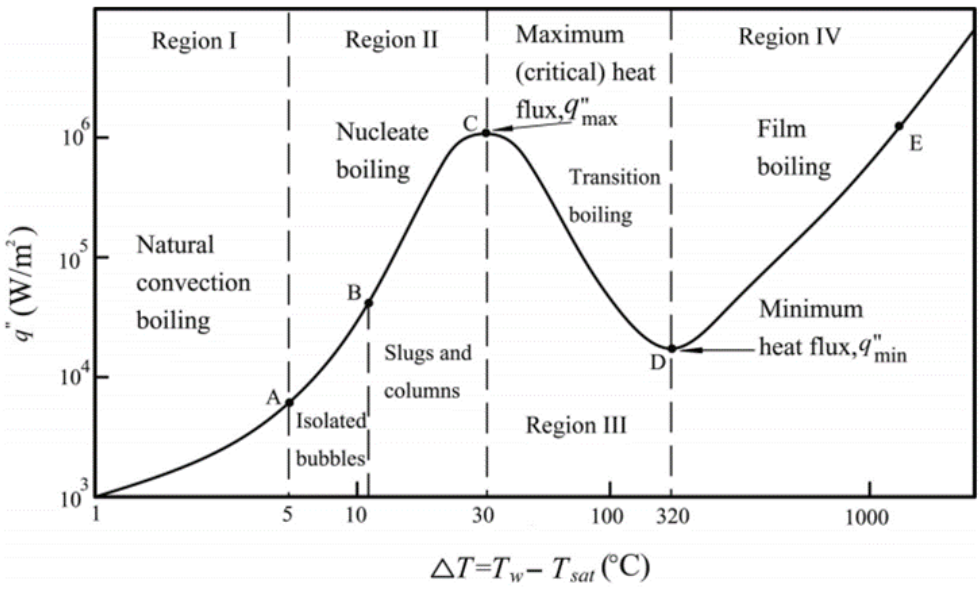

Figure 2.8: Boiling curve for saturated liquid (Wilcox, 2012: 38)

From Figure 2.8 only the two flow boiling regimes important to this study are identified and discussed. Based on water at ambient pressure, these include the single-phase forced convection regime and the nucleate boiling regime.

The natural convection boiling regime, up to point A, is identified with wall superheats (ΔT_{sat}) below 5°C (Charry León, 2014: 14). During this regime single-phase convection is the prevailing heat transfer mechanism and no vapour bubbles are formed. The fraction of the vapour phase in contact with the liquid phase is insufficient to cause boiling at the liquid saturation temperature. The wall heat flux to wall superheat ratio is governed by Newton's law of cooling for single-phase convection transfer.

Nucleate boiling occurs at wall superheats ranging from 5 °C to 30 °C (Charry León, 2014: 15). In Figure 2.8 we see that the onset of nucleate boiling (ONB) starts at point A. At this stage isolated vapour bubbles generated at the nucleation sites begin to detach from the wall causing increases in the heat transfer coefficient due to bubble movement. In the case of subcooled boiling these vapour bubbles condense after detaching from the wall due to the liquid subcooling. For nucleate boiling on the other hand, this is not the case, since the bulk liquid and the vapour bubbles are both at saturation temperature.

Beyond point A, increases in the wall heat flux lead to increases in the bubble departure frequency which result in the agglomeration of the vapour bubbles. At location B groups of vapour bubbles coalesce into slugs of vapour. At point C the

heat flux reaches a maximum value known as the critical heat flux (CHF). According to Charry León (2014: 15) the region between points A and C is known as the fully developed nucleate boiling region and the wall heat flux is determined by the following relation.

$$q'' \approx \Delta T_{sat}^{n} \tag{2.30}$$

As the heat flux continues to increase, groups of vapour bubbles start to aggregate into a continuous film on the heated wall surface. This decreases the contact area between the bulk fluid and the wall and leads to the phenomenon known as the first boiling crisis, which equals the maximum allowable wall heat flux prior to tube failure.

2.7.2 Critical Heat Flux in Helically Coiled Tubes

The vapour mass fractions giving rise to the boiling crisis is lower for horizontal or inclined tubes due to the phase separation caused by the gravitational forces (Auracher & Herbst: 2010: 841). Gravity effects result in unequal wetting of the tube periphery whilst separation effects are dependent on tube geometry. Critical boiling crisis in helical coil tubes is synonymous to that of horizontal tubes in that an initial and final boiling crisis can be identified.

The effect of centrifugal and gravitational forces on the liquid or vapour phase is strongly dependent on the flow regime within the tubes. At flows with low vapour qualities the stratified wavy flow regime is dominant, whilst annular or semi-annular flow regimes can be identified for flows with high vapour qualities. In annular flow there exists a distinct liquid film between the vapour core and the tube wall.

Figure 2.9(b) shows that the liquid film in upward concurrent flow in a helically coiled tube mainly exists on the outer wall of the tube. For a mass velocity below 850 kg/m^2.s the liquid film is moved to the neutral position, Figure 2.9(a). At mass velocities > 850 kg/m^2.s liquid entrained from the liquid film is thrown onto the inner part of the wall as seen in Figure 2.9(c).

In his study Elsayed contributed this relocation of the liquid film from outer to the inner tube wall of helically coiled tubes to film inversion, which occurs at low liquid and high gas flow rates (Elsayed, 2011: 34). Elsayed further adds that this phenomenon is in contrast to the general assumption that the liquid phase in helical coils would be forced to the tube outer wall due the centrifugal effects.

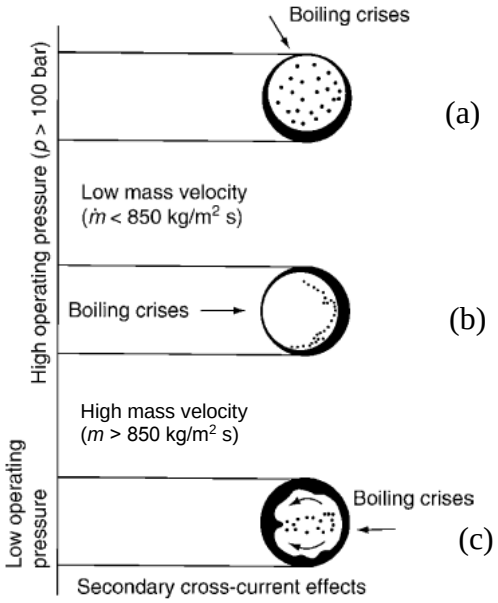

Figure 2.9: Location of the flow boiling crisis in helically coiled tubes (Auracher & Herbst, 2010: 844)

From Figure 2.9 it can also be observed that the location of the boiling crisis is a function of the fluid mass velocity, the resultant centrifugal force and the boiler operating pressure.

The following experimental correlations were formulated by Ünal (1981: 6.7) for determining the critical vapour mass fraction and its position within a helical coil

$$x_{cr} = 3.88\, K_h\, K_P\, K_D\, K_\delta\, K_m + x_{in} \tag{2.31}$$

where the factors above are determined as follows;

$$K_h = 1 + 3.8\left(1 - H_{in}/H'\right)$$

$$K_P = 0.114 - 0.041\, ln\left(1 - P_r\right)$$

$$K_D = 1 + 0.44\, \exp\left(-0.056\, D_w/d\right) \qquad \text{(for the first boiling crisis)}$$

$$K_D = 1 + 0.56\, \exp\left(-0.011 D_w/d\right) \qquad \text{(for the last boiling crisis)}$$

$$K_\delta = \left(\frac{2\delta}{d}\right)^{0.32} \text{ and } K_m = \frac{\left(L_{cr}/d\right) + 4.59\left(L_{cr}/d\right)^{-0.2}}{\left(L_{cr}/d\right) + 28\, Fr^{0.44}}$$

The location and magnitude of the boiling crisis can then be determined from the heat balance and empirical correlation derived by Babarin and Alad'yev (Auracher & Herbst, 2010: 845) as shown below.

$$\frac{L_{cr}}{d} = \frac{m\Delta H_v}{4\dot{q}}\left(x_{cr} - x_{in}\right) \tag{2.32}$$

$$q_{cr} = 585\left(\frac{m}{L/d}\right)^{0.9}\left[1 + C_w\left(0.75 + x_{in}\right)\right] \tag{2.33}$$

2.8 Pressure Drop inside Helically Coiled Tubes

The presence of secondary flows inside helically coiled tubes causes the tube to have higher pressure drops compared to straight tubes. However, the pressure drop analogy used for straight tubes can still be successfully applied to helical coil tubes when a modified equation is used for determining the friction factor. The friction factor correlations for laminar and turbulent flow inside helically coiled tubes proposed by Mishra and Gupta are given as (Gnielinski, 2010: 710):

For laminar flow for range, $1 < Re < Re_{cr}$

$$f_l = \frac{64}{Re}\left[1 + 0.033\left(\log_{10}\left(Re\sqrt{d/D}\right)\right)^4\right] \tag{2.34}$$

For turbulent flow and valid for the range $Re_{cr} < Re < 10^5$

$$f_t = \frac{0.3164}{Re^{0.25}}\left[1 + 0.095\sqrt{d/D}\ \sqrt[4]{Re}\right] \tag{2.35}$$

The critical Reynolds number is the same as previously mentioned, see equation (2.23).

3 HELICAL COIL BOILER SIZING

The calculated geometry of the helical coil boiler prototype is based on the 1D steady-state thermal model described in the preceding chapter. Assumptions applied for creating such a model are as follows:

- State of water entering the economiser section is that of a subcooled liquid
- Final state of water leaving the evaporator is saturated vapour with a dryness fraction of 0.98
- The process of evaporating water is isothermal
- Saturated steam supplied to the superheater is 99% dry
- John Thompson tube wall design temperatures as per Table 3.1

Refer to Appendix E for manufacturing drawings of the superheater, evaporator and economiser sections.

Table 3.1: Tube wall temperature assumptions

Zone	Mode of Heat Transfer	Tube Wall Temperature
Furnace	Radiation	T_{sat} + 20°C
Superheater	Convective	T_{sat} + 50°C
Evaporator	Convective	T_{sat} + 5°C
Economiser	Convective	T_{sat} +5°C

The flue gas composition used in the computations is derived from the combustion of coal. The pertinent flue gas properties such as thermal conductivity, dynamic viscosity, density and mean specific heat of the products of combustion are calculated using the appropriate VDI Heat Atlas tables (Kleiber & Joh, 2010: 301-393).

Thermodynamic properties of water and steam used in the thermal model are based on the data published by The International Association for the Properties of Water and Steam (IAPWS, 2010).

The 1D steady-state thermal model is then iteratively solved in Microsoft Excel™ by incorporating the above assumptions and flue gas and steam properties. Refer to Appendix B, C and D for sample calculations of the furnace, superheater and evaporator.

3.1 Furnace Sizing

The grate rating of a stoker defines the grate area required to efficiently burn 1 kg of solid fuel in an hour. The maximum grate rating is a function of the properties of the fuel. Thus, the better the fuel quality the higher the grate rating.

The John Thompson Triumph chaingrate stoker used as the basis for the boiler design has a maximum grate rating of 220 kg/m^{2}h.

The furnace volumetric heat release rate defines the ratio of fuel burned to energy released per cubic meter within the furnace, and typically falls within the range of 155 – 207 kW/m^3. The size of the refractory lined furnace is based on the previously mentioned John Thompson best practices, whilst that of the water-cooled portion of the furnace is based on the radiant heat transfer equations described in earlier sections. Results of the sizing for a water-cooled furnace are shown in Table 3.2.

Table 3.2: Summary of furnace thermal design

Gas side	Fluid	--	Flue gas
	Side	--	Shell
	Flow rate	kg/hr	17118
	Inlet temperature	^{o}C	967.0
	Outlet temperature	^{o}C	949.6
	Pressure drop	Pa	--
	Heat transferred	kW	104.7
Waterside	Fluid	--	Water/Steam
	Side	--	Tube
	Flow rate	kg/hr	14700
	Inlet temperature	^{o}C	264.9
	Outlet temperature	^{o}C	264.9
	Inlet pressure	kPa	4999.0
	Pressure drop	kPa	--
	Heat transferred	kW	104.7

3.2 Sizing Convective Heat Transfer Areas

The convective heat transfer areas of the helical coil boiler are determined using the 1D steady-state thermo-fluid design model created using previously described heat transfer equations and John Thompson in-house standards. The sizing results from the calculations are summarised in Table 3.3 to Table 3.5.

The manufacturing drawings and fabrication photos of the prototype boiler illustrating the inferred heat transfer areas of the furnace, evaporator, superheater and economiser are shown in Appendix E and G.

Table 3.3: Summary of superheater thermal design

Gas side	Fluid	--	Flue gas
	Side	--	Shell
	Flow rate	kg/hr	17118
	Inlet temperature	^{o}C	949.6
	Outlet temperature	^{o}C	773.0
	Pressure drop	Pa	20.05
	Heat transferred	kW	1049.2
Waterside	Fluid	--	Steam
	Side	--	Tube
	Flow rate	kg/hr	10500
	Inlet temperature	^{o}C	259.0
	Outlet temperature	^{o}C	380.7
	Inlet pressure	kPa	4515.9
	Pressure drop	kPa	15.9
	Heat transferred	kW	1049.2

Table 3.4: Summary of evaporator thermal design

Gas side	Fluid	--	Flue gas
	Side	--	Shell
	Flow rate	kg/hr	17118
	Inlet temperature	^{o}C	773.0
	Outlet temperature	^{o}C	363.0
	Pressure drop	Pa	78.27
	Heat transferred	kW	2289.5
Waterside	Fluid	--	Water/Steam
	Side	--	Tube
	Flow rate	kg/hr	14700
	Inlet temperature	^{o}C	264.9
	Outlet temperature	^{o}C	264.9
	Inlet pressure	kPa	4999.0
	Pressure drop	kPa	483.1
	Heat transferred	kW	2289.5

Table 3.5: Summary of economiser thermal design

Gas side	Fluid	--	Flue gas
	Side	--	Shell
	Flow rate	kg/hr	17118
	Inlet temperature	^{o}C	363.0
	Outlet temperature	^{o}C	278.2
	Pressure drop	Pa	69.12
	Heat transferred	kW	445.6
Waterside	Fluid	--	Water/Steam
	Side	--	Tube
	Flow rate	kg/hr	14700
	Inlet temperature	^{o}C	265.3
	Outlet temperature	^{o}C	265.3
	Inlet pressure	kPa	5027.9
	Pressure drop	kPa	28.9
	Heat transferred	kW	445.6

3.3 Determination of the Evaporator Circulation Rate

The evaporator circulation rate required to avoid departure from nucleate boiling (DNB) was determined using the formulae developed by Ünal (see Appendix D). Results obtained from the 1D steady-state model for a boiler circulation rate of 1.4 times the boiler design evaporation is as follows:

First Boiling Crisis (DNB)

- Critical vapour mass fraction = 0.542
- Location of boiling crisis = 213.3m
- Critical heat flux =77.93 kW/m^2

Second Boiling Crisis (Deposition controlled burnout)

- Critical vapour mass fraction = 0.834
- Location of boiling crisis = 277.1m
- Critical heat flux = 101.09 kW/m^2

4 NUMERICAL MODEL – SINGLE-PHASE FLUID FLOW

In contrast to the empirical correlation used in the 1D steady-state thermal model, CFD simulations are able to provide a more in-depth understanding of the fluid thermal and hydraulic behaviour needed to quantify increases in heat transfer and characterise fluid motion. Of particular importance in the design of the helically coiled boiler is the secondary flow effects, evolution of the vapour phase and the 3D wall temperature profile. The latter is used to establish the location of the first boiling crisis which in turn is used to determine the boiler circulation rate needed to avoid overheating of the tubes.

Computational fluid dynamics entails numerically solving the equations governing the motion and heat transfer of a fluid inside a computational domain. The numerical model used for solving the heat transfer and fluid flow within the helical coil is based on the fundamental principles of conservation of mass, momentum and energy. The numerical solution of the coil segment under consideration in this study is done using the commercially available ANSYS Fluent CFD package. The coil geometry is discretized into 3D control volumes due to the complex nature of the coil geometry and the resulting flow field.

The following section presents the governing equations required to solve the flow field expected within a helically coiled tube.

4.1 Conservation Equations

The governing equations for fluid flow and heat transfer are derived from the principles of conservation of mass, momentum and energy (Versteeg & Malalasekera, 2007: 9). Fluid motion and heat transfer can be described by a set of transport equations which track the gradients of the fluid properties resulting from convection, diffusion and other sources or sinks of the conserved or transport quantity.

4.1.1 Mass Conservation

Mass conservation within the incompressible fluid domain of the helical coil is characterised by the steady state continuity equation as,

$$\frac{\partial}{\partial x_j}\left(\rho u_j\right)=0 \tag{4.1}$$

Where ρ and u in the above expression respectively represent the fluid density and velocity vector in directions x_j (j = 1, 2, 3). The term on the left-hand side of the above equation represents the convective transport of mass flow across the fluid volume.

4.1.2 Momentum Conservation

Momentum conservation of a fluid particle relate the momentum changes of a fluid particle to the surface and body forces acting on the particle, and obeys Newton's second law. The surface forces include pressure, viscous and gravity forces; and the body forces consists of centrifugal, Coriolis and electromagnetic forces (Versteeg & Malalasekera, 2007: 14). Momentum conservation is mathematically expressed as,

$$\frac{\partial}{\partial x_j}\left(\rho u_i u_j + P\delta_{ij} - \tau_{ij}\right) = 0 \tag{4.2}$$

Where pressure is a normal stress denoted by P, δ_{ij} is the Kronecker delta and τ_{ij} is the viscous stress components.

The viscous stress components of the momentum conservation equations for a Newtonian fluid can be expressed in terms of local strain rates, which in three-dimensional flow consists of both linear and volumetric strain rates (Versteeg & Malalasekera, 2007: 29). The linear and volumetric strain rates for an incompressible fluid are related to the viscous stresses in terms of the fluid dynamic viscosity and velocity gradients as,

$$\tau_{ij} = \mu\left(\frac{\partial u_i}{\partial x_j} + \frac{\partial u_j}{\partial x_i}\right) \tag{4.3}$$

Conservation of momentum within the three-dimensional helical coil tube can be expressed in terms of the Navier-Stokes equations. Substitution of the viscous stress terms into the momentum equation, followed by rearranging and averaging of the momentum equations results in the averaged Navier-Stokes equations which can be written as,

$$\frac{\partial}{\partial x_j}\left(\rho u_i u_j\right) = -\frac{\partial P}{\partial x_i} + \rho g_i + \frac{\partial}{\partial x_j}\left[\mu\left(\frac{\partial u_i}{\partial x_j} + \frac{\partial u_j}{\partial x_i}\right)\right] + \frac{\partial}{\partial x_j}\left(-\rho\overline{u_i' u_j'}\right) \tag{4.4}$$

In the preceding Reynolds Averaged Navier-Stokes (RANS) equation the convective terms are on the left-hand side whilst the pressure gradient, gravitational force, viscous stresses, Reynold stresses and other source terms (not shown) are on the right-hand side. The overbar in the Reynolds stress term indicates that the momentum equation has been averaged and that the stress term represents averaged quantities.

4.1.3 Energy Conservation

Energy conservation follows the first law of thermodynamics, which states that energy cannot be created or destroyed, but merely transformed from one form to another. It is expressed in terms of the ensuing equation as,

$$\frac{\partial}{\partial x_i}\left(\rho u_i T\right) = \frac{\partial}{\partial x_j}\left(\left(\Gamma + \Gamma_t\right)\frac{\partial T}{\partial x_j}\right)\Gamma \tag{4.5}$$

where Γ = molecular thermal diffusivity
Γ_t = turbulent thermal diffusivity

4.2 Modelling of Turbulence

In CFD the previously mentioned Reynolds stresses are computed using appropriate turbulence closure models and the subsequent result is used to solve equation (4.4). Turbulence models mathematically resolve the Reynolds stresses by solving the apparent shear stress term, $\overline{u_i u_j}$ (Kays et al, 2005: 182). This is achieved through the introduction of a proportionality factor in the form of the eddy diffusivity for momentum, ε_m, and the eddy or turbulent viscosity term, μ_t,

$$\text{where } \overline{u_i u_j} = \varepsilon_m \frac{\partial \overline{u_i}}{\partial x_j} \tag{4.6}$$

$$\text{and } \mu_t = \rho \varepsilon_m \tag{4.7}$$

These turbulence models predict the mean and fluctuating components of velocity and other scalar quantities, such as pressure and time, of fluid flow without solving the entire turbulent flow field (Bakker, 2002: 33). The turbulence models considered in the analysis of the helical coil tube are summarised in the sections which follow.

4.2.1 The *k*-ε Turbulence Model

The *k*-ε turbulence model is a two-equation model used to compute the Reynolds stresses by solving two additional transport equations with the assumption that an analogy exists between the action of the viscous and Reynolds stresses. Applying the Boussinesq hypothesis in order to relate Reynolds stresses to the mean velocity we get;

$$-\rho\overline{u_i' u_j'} = \mu_t\left(\frac{\partial u_i}{\partial x_j} + \frac{\partial u_j}{\partial x_i}\right) \tag{4.8}$$

The turbulent viscosity term, μ_t, is computed using the *k*-ε turbulence model with the application of two additional equations namely the turbulent kinetic energy and the turbulent dissipation rate equations,

$$\text{where } \mu_t = \rho C_\mu \frac{k^2}{\varepsilon} \tag{4.9}$$

The turbulent kinetic energy term, *k*, is determined using the following transport equation

$$\frac{\partial}{\partial x_i}(\rho k u_i) = \frac{\partial}{\partial x_j}\left[\left(\mu + \frac{\mu_t}{\sigma_k}\right)\frac{\partial k}{\partial x_j}\right] + G_k + G_b - \rho\varepsilon \tag{4.10}$$

Where $\rho\varepsilon$ equals the turbulent destruction rate of the generation of the turbulent kinetic energy due to velocity and buoyancy, represented by G_k and G_b respectively,

$$\text{where } G_k = -\rho\overline{u_i' u_j'}\frac{\partial u_j}{\partial x_i} \text{ and} \tag{4.11}$$

$$G_b = \beta g \frac{\mu_t}{Pr_t}\frac{\partial T}{\partial x_i} \tag{4.12}$$

The turbulent dissipation rate, ε, used in the determination of the fluid turbulent viscosity is calculated from

$$\frac{\partial}{\partial x_i}(\rho \varepsilon u_i) = \frac{\partial}{\partial x_j}\left[\left(\mu + \frac{\mu_t}{\sigma_\varepsilon}\right)\frac{\partial \varepsilon}{\partial x_j}\right] + C_{1\varepsilon}\frac{\varepsilon}{k}(G_k + C_{3\varepsilon}G_b) - 2C_{2\varepsilon}\rho\frac{\varepsilon^2}{k} \tag{4.13}$$

The quantities C_μ, $C_{1\varepsilon}$, $C_{2\varepsilon}$, σ_k and σ_ε as per equations (4.9) to (4.13) are empirical constants based on experimental observations of fluid behaviour under high Reynolds number flows, and have magnitudes as per Table 4.1.

Table 4.1: Standard *k*-ε model empirical constants

C_μ=0.09	$C_{1\varepsilon}$=1.44	$C_{2\varepsilon}$=1.92
σ_k=1.00	σ_ε=1.30	Pr_t=0.85

4.2.2 The RNG *k-ε* Turbulence Model

In contrast to the standard *k-ε* model, the RNG *k-ε* model is derived using statistical methods used in the field of renormalization group (RNG) theory. This model utilises a modified dissipation equation to more accurately account for flow in regions of high fluid strain such as bends. Another enhancement over the standard *k-ε* model is the solution of the turbulent viscosity term by means of a differential equation.

The modified turbulent dissipation rate equation for the RNG *k-ε* model including the additional term, R_ε, used to resolve regions of high fluid strain is:

$$\frac{\partial}{\partial x_i}(\rho \varepsilon u_i) = \frac{\partial}{\partial x_j}\left[\alpha_\varepsilon \mu_{eff} \frac{\partial \varepsilon}{\partial x_j}\right] + C_{1\varepsilon}\frac{\varepsilon}{k}(G_k + C_{3\varepsilon}G_b) - 2C_{2\varepsilon}\rho\frac{\varepsilon^2}{k} - R_\varepsilon \qquad (4.14)$$

$$\text{where } R_\varepsilon = \frac{C_\mu \rho \eta^3 (1-\eta/\eta_o)}{1+\beta\eta^3}\frac{\varepsilon^2}{k} \qquad (4.15)$$

The differential equation for solving the turbulent viscosity term, μ_t, is

$$d\left(\frac{\rho^2 k}{\sqrt{\varepsilon\mu}}\right) = 1.72\frac{\hat{\nu}}{\sqrt{\hat{\nu}^3 - 1 + C_\nu}}d\hat{\nu} \qquad (4.16)$$

where $\hat{\nu} = \frac{\mu_{eff}}{\mu}$ and C_ν is a constant approximately equal to 100.

Analytically derived constants and relationships for the computation of variables used in the RNG *k-ε* model are presented in Table 4.2.

Table 4.2: Analytically derived constants for RNG *k-ε* model

$\eta \equiv Sk/\varepsilon$	$\eta_o = 4.38$	$\beta = 0.012$
$C_{1\varepsilon} = 1.42$	$C_{2\varepsilon} = 1.68$	

4.2.3 The Realizable *k-ε* Turbulence Model

The realizable *k-ε* model improves on the standard *k-ε* model by using a variable instead of a constant for C_μ in order to eliminate physical or unrealizable errors associated with negative Reynolds stresses under highly strained flows.

The variable form of the constant C_μ is subsequently determined using fluid properties such as local strain rate and rotation to eliminate the generation of unrealistic Reynolds stresses. The relationship for the determination of C_μ is

$$C_\mu = \frac{1}{A_0 + A_s \frac{kU^2}{\varepsilon}} \tag{4.17}$$

where the terms A_0, A_s, and U are model constants.

Additionally, turbulence dissipation is computed using source and sink terms which differ from the standard and RNG k-ε models. This leads to

$$\frac{\partial}{\partial x_i}(\rho \varepsilon u_i) = \frac{\partial}{\partial x_j}\left[\left(\mu + \frac{\mu_t}{\sigma_\varepsilon}\right)\frac{\partial \varepsilon}{\partial x_j}\right] + \rho C_1 S \varepsilon - \rho C_2 \frac{\varepsilon^2}{k + \sqrt{\nu \varepsilon}} + C_{1\varepsilon}\frac{\varepsilon}{k} C_{3\varepsilon} G_b \tag{4.18}$$

where $C_1 = \max\left[0.43, \frac{\eta}{\eta + 5}\right]$

$$\eta = S\frac{k}{\varepsilon} \text{ and } S = \sqrt{2 S_{ij} S_{ij}}$$

The treatment of the prediction of ε and the alternative method for calculating μ_t results in a model which is superior to other k-ε models for numerous applications (Marshall & Bakker, 2001: 8). For model constants used with the realizable k-ε model refer to Table 4.3.

Table 4.3: Model constants for use with realizable k-ε model

σ_ε=1.20	$C_{1\varepsilon}$=1.44	C_2=1.9
σ_k=1.00	Pr_t=0.85	

4.3 Near-wall Treatment

The turbulent boundary layer is the region on the wall surface consisting of an outer and inner layer, see Figure 4.1. The inner region can be further subdivided into a viscous sublayer, a buffer layer and a fully turbulent region. The viscous sublayer is the thin region close to the wall where viscous effects dominate. In the fully turbulent region velocity fluctuations exist due to fluid vorticity, which results in turbulent flow (Kays et al, 2005: 181).

According to Wilcox (2010: 16), for the fully turbulent portion of the boundary layer the logarithmic law of the wall is able to accurately represent the log-linear variation of the non-dimensional velocity u^+. In the viscous sublayer it is assumed that $u^+ = y^+$.

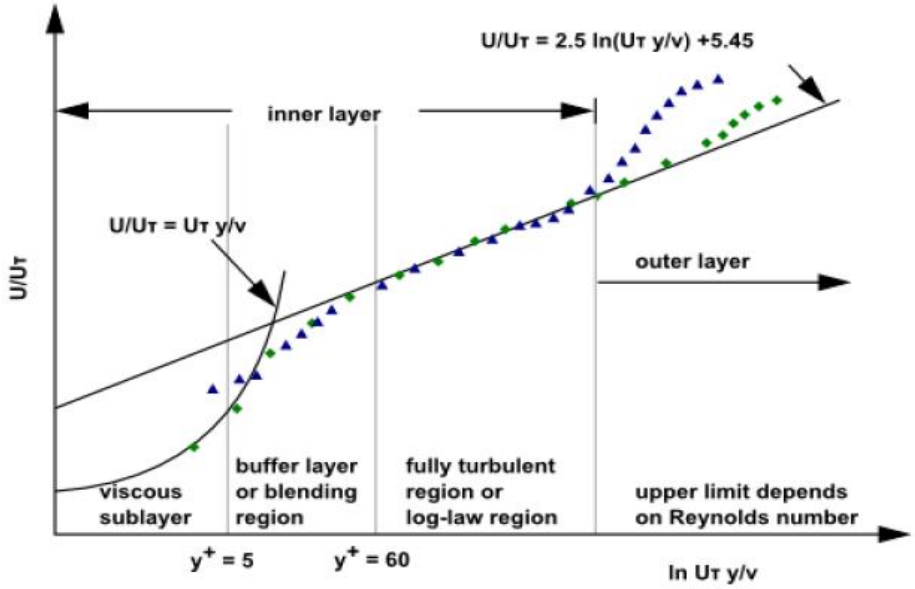

Figure 4.1: The turbulent boundary layer (ANSYS Fluent Theory Guide, 2013:113)

The turbulence models discussed in the earlier sections are used throughout the fully turbulent region, but the momentum and heat flux in the viscosity affected inner region (viscous sublayer and buffer layer) is obtained from the wall function or near-wall modelling approach (see Figure 4.2). In the wall function approach semi-empirical formulae derived from the logarithmic law of the wall are used to bridge the gap between the wall and the fully turbulent region. The near-wall modelling approach on the other hand completely resolves the viscosity affected inner region up to the viscous sublayer by combining a two-layer model with a blended law of the wall. ANSYS Fluent near-wall treatment methods considered in this work included the standard and non-equilibrium wall functions for the wall function modelling approach; and the enhanced wall treatment method for the near-wall modelling approach.

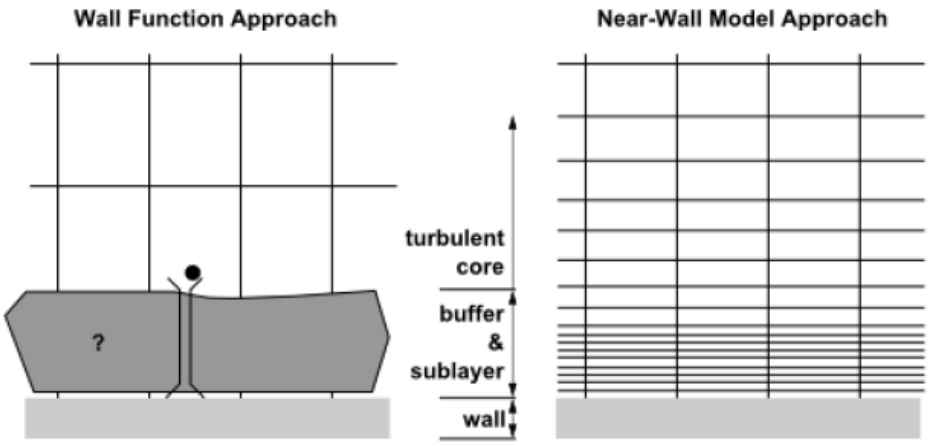

Figure 4.2: Near-wall treatment (ANSYS Fluent Theory Guide, 2013:114)

Standard wall functions for the momentum equations offer good estimations of the near-wall fluid interaction by relating the local shear stress to the mean velocity, turbulence kinetic energy and rate of dissipation. In ANSYS Fluent this is achieved as follows (ANSYS Fluent Theory Guide, 2013: 115):

$$u^+ = \frac{\bar{u}}{\sqrt{\tau_w/\rho}} \tag{4.19}$$

$$y^+ = \frac{y\sqrt{\tau_w/\rho}}{\nu} \tag{4.20}$$

where $u^+ = 1/\kappa \times ln\left(E\,y^+\right)$ for $y^+ \geq 11.225$, and

$u^+ = y^+$ for $y^+ \leq 11.225$

In the above equations $\bar{u}$ is time-mean velocity, τ_w is the wall shear stress, κ is the von Karman constant and E is an empirical constant.

The non-equilibrium wall function is an improvement of the standard wall function by accounting for pressure gradients and is suitable for use in complex flows entailing separation and reattachment such as the case of flow inside a helical coil. It achieves this by implementing a two-layer model to compute a cell-averaged turbulence kinetic energy production and dissipation rate in cells adjacent the wall, and a log law with sensitised pressure-gradient effects (Tu *et al*, 2013: 259).

The enhanced wall treatment method on the other hand resolves the entire boundary layer up the viscous sublayer by using a two-layer model approach together with enhanced wall functions (Tu *et al*, 2013: 260). It directly models the boundary layer for $y^+=1$ and uses the wall function approach for y^+ => 30 by using a blending function to ensure a smooth transition between the linear and log-laws, see Figure 4.2. The enhanced wall function for the momentum equation which includes Kader's blending function is (Kader, 1979: 1544):

$$u^+ = e^{\Gamma} u_l^+ + e^{1/\Gamma} u_t^+ \tag{4.21}$$

where $\Gamma = \dfrac{a\left(y^+\right)^4}{1+by^+}$, is the blending function

and a = 0.01 and b = 5 are model constants.

In order to distinguish the different regions near the wall, the concept of a dimensionless wall y^+, which is the distance measured from the wall in terms of viscous lengths, has been formulated. Table 4.4 shows wall treatment methods with typical y^+ values from literature for use with the previously discussed turbulence models.

Table 4.4: Recommended y^+ values

Wall treatment method	**Recommended y^+ values**
Standard wall function	$30 < y^+ < 300$
Non-equilibrium wall function	$30 < y^+ < 300$
Enhanced wall treatment	$y^+ < 5$

5 NUMERICAL MODEL – TWO-PHASE FLUID FLOW

5.1 Modelling of Multiphase Flows

The capturing of the evaporation effects experienced by the fluid control volume within the helically coiled tube is done using a multiphase flow model. Multiphase flow models predict the location of the liquid-gas interface by assigning a separate set of fluid transport properties to the control volume. These additional fluid properties, such as density, enable forces of different magnitudes to act on the fluid control volume, thereby facilitating the determination of the liquid-gas interface.

The multiphase models available in commercial CFD packages can be divided into two main categories, namely the Eulerian-Lagrangian and the Eulerian-Eulerian approach. In the Eulerian-Lagrangian models the Navier-Stokes equations are used to describe a homogenous fluid phase, whilst the Lagrangian particle tracking method is used to describe a dispersed droplet or bubble phase. The Eulerian-Eulerian models on the other hand treat all phases as interpenetrating continua. In this study only the Eulerian-Eulerian models are described as Eulerian-Lagrangian models were unsuitable, since they are limited to applications where the dispersed phase at any location is less than 10% by volume of the mixture.

5.2 Eulerian Multiphase Model

Interpenetrating liquid and gas systems are modelled using the Eulerian multiphase model. The Eulerian model can be used for a plethora of phase volume fractions. This is made possible by the application of separate sets of momentum and continuity equations to describe each fluid phase. Additional interchange terms within the momentum equation allow for the capturing of momentum transfer between the fluid phases. Heat and mass transfer between fluid phases are incorporated in extra exchange terms in the energy and continuity equations. Fluid phase interaction is monitored by ensuring equilibrium of the volume fractions for all phases within all control volumes. In this model the complete set of conservation equations is solved for each of the fluid phases.

Like single-phase flow, multiphase flow is also governed by the mass, momentum and energy equations. However, and as can be seen in the equations below, additional terms are introduced to the conservation equations for multiphase flows. These terms include the interfacial drag force (R_{pq}), the lift force ($F_{L,q}$), the turbulent diffusion force (F_q), and the interphase energy exchange term (Q).

For mass conservation of phase q,

$$\frac{\partial}{\partial t}\left(\alpha_q \rho_q\right)+\frac{\partial}{\partial x_i}\left(\alpha_q \rho_q u_q\right)=\sum_{p=1}^{n} m_{pq} \tag{5.1}$$

Where subscripts p and q denote the individual phases, α is the volume fraction, ρ is the density, u is the velocity and m_{pq} is the mass exchange from phase p to phase q and vice versa.

For momentum conservation of phase q,

$$\begin{aligned}\frac{\partial}{\partial t}\left(\alpha_q \rho_q u_q\right)+\frac{\partial}{\partial x_i}\left(\alpha_q \rho_q u_q u_q\right)=&-\alpha_q \frac{\partial}{\partial x_j} P+\frac{\partial}{\partial x_j}\tau_q+\alpha_q \rho_q g_q \\ &+\sum_{p=1}^{n}\left(R_{pq}+m_{pq}u_{pq}\right) \\ &+\alpha_q \rho_q\left(F_q+F_{L,q}+F_{wl,q}+F_{vm,q}+F_{td,q}\right)\end{aligned} \tag{5.2}$$

Where τ_q is the strain tensor, g_q is the gravitational acceleration, R_{pq} is the interfacial drag force between phase p and q, $F_{wl,q}$ is the wall lubrication force, $F_{vm,q}$ is the virtual mass force, and $F_{td,q}$ is the turbulent dispersion force.

And for energy conservation of phase q,

$$\begin{aligned}\frac{\partial}{\partial t}\left(\alpha_q \rho_q H_q\right)+\frac{\partial}{\partial x_i}\left(\alpha_q \rho_q u_q u_q\right)=&-\alpha_q \frac{\partial P}{\partial t}+\tau_q : \frac{\partial}{\partial x_j} u_q-\frac{\partial}{\partial x_j} q_q \\ &+S_q+\sum_{p=1}^{n}\left(Q_{pq}+\dot{m}_{pq}H_{pq}\right)\end{aligned} \tag{5.3}$$

Where H_q is the specific enthalpy of phase q, q_q is the heat flux, S_q is a source term for enthalpy, Q_{pq} is the intensity of heat exchange between the phases and, H_{pq} is the interphase enthalpy.

The multiphase flow models and interphase exchange terms available in ANSYS Fluent, which were considered in this study, are described later in the text.

5.2.1 Volume of Fluid (VOF) Model

Computationally the least expensive Eulerian model available, this model is used to replicate two or more immiscible fluids by solving a single set of momentum equations.

The VOF model separately assigns gas or liquid properties to the computational cells, which result in the solution of a single set of the Navier-Stokes equations. It is mostly used where tracking of the liquid-gas interface is of importance, and achieves this by tracking the volume fraction of each of the fluids through the

computational domain. The model however is limited to applications where the vapour phase at any location is less than 17% by volume of the mixture.

5.2.2 Mixture Model

The mixture model is a simplified multiphase model used to simulate flows where the phases move at different velocities and assume local equilibrium across a small spatial length scale. It is able to model homogeneous multiphase flows where the phases have strong coupling effects. In this model the momentum, continuity and energy equations are solved for the mixture, whilst volume fraction transport equations are used for tracking the different phases. Algebraic expressions, in the form of the slip velocity term, are used to resolve the relative phase velocities.

This model enables the modelling of water evaporation, boiling of water and the rise of gas within a liquid by allowing heat, mass and momentum transfer between the dispersed and fluid phases.

5.2.3 The RPI Wall Boiling Model

The Kurul and Podowski model for heat flux partitioning, also known as the Rensselaer Polytechnic Institute (RPI) model, is used in high-pressure boiling applications to split the wall heat flux into three different modes of heat transfer.

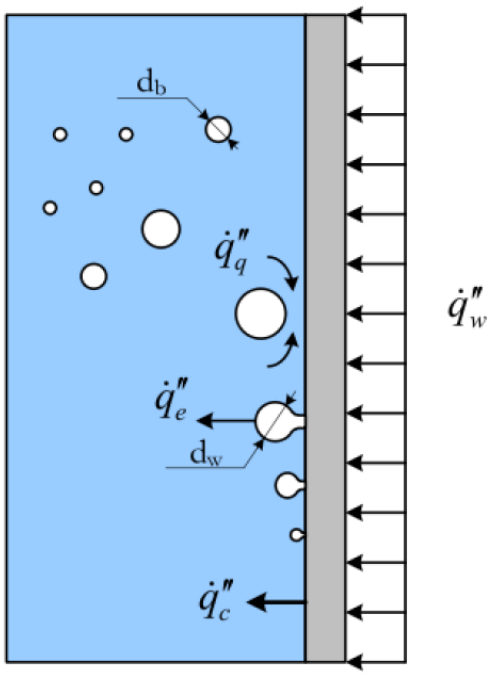

Figure 5.1: Kurul and Podowski model for partitioning of wall heat flux (Mitchta, 2011:10)

The modes of heat transfer incorporated in the RPI model are summarised as;

$$q_w = q_c + q_q + q_e \tag{5.4}$$

Where q_c is the single-phase convection heat flux, q_q is the quenching heat flux and q_e is the heat flux due to wall evaporation (Kurul & Podowski, 1990: 22). Refer to Figure 5.1 for a graphical representation of the RPI model.

The single-phase convective heat transferred to the liquid phase, which takes place in the area of the wall where nucleating bubbles are not present, is modelled using the wall temperature function of Kader.

$$q_c = \frac{\rho_l \, c \, u_w}{T^+_{y^+(nw)}} \times (1 - A_b) \times \left(T_w - T_{l(nw)}\right) \tag{5.5}$$

In equation (5.5) above, $T_{l(nw)}$ is the liquid temperature of the near-wall cell, $T^+_{y^+(nw)}$ is the non-dimensional temperature determined using Kader and u_w is the frictional velocity (Kader, 1979:1). Here A_b is the wall surface area covered by nucleate bubbles and is subject to convective or quenching heat transfer. The area covered by the liquid phase is presented by the term, $(1 - A_b)$ in equation (5.5). This term is known as the area of influence and is a function of the nucleation site density and bubble diameter as can be seen below (Del Valle & Kenning, 1985: 1916);

$$A_b = \min\left(1, K \frac{N_w \pi d_{bw}^2}{4}\right) \tag{5.6}$$

In the above equation N_w is the nucleate site density, d_{bw} is the bubble departure diameter and *K* is an empirical constant determined using the relation based on the findings of Del Valle and Kenning, where;

$$K = 4.8 \times e^{(-Ja/80)} \tag{5.7}$$

In equation (5.7) above, the constant is a calculation factor and Ja is the Jacobs number, which is a measure of the bubble subcooling,

$$Ja = \frac{\rho_l \, c_l \left(T_{sat} - T_l\right)}{\rho_g H_{fg}} \tag{5.8}$$

The behaviour of the bubbles near the tube wall has a profound influence on the wall heat flux. Bubble near-wall characteristics were studied by numerous researchers and their findings resulted in a number of correlations used for

determining the bubble characteristics. These include, amongst others, the correlations of Lemmert and Chawla, Ünal, and Kocamustafaogullari and Ishii.

In this work the correlation of Kocamustafaogullari and Ishii, as described below, was implemented. The most pertinent near-wall bubble parameters include nucleation site density, bubble departure diameter and bubble departure frequency. The equation used for determining the bubble quantity at the nucleation site is (Kocamustafaogullari & Ishii, 1983: 1383):

$$N_w = \frac{1}{d_{bw}^2}\left[\frac{2\,\sigma\,T_{sat}}{(T_w - T_{sat})\rho_g H_{fg}}\frac{2}{d_{bw}}\right]^{-4.4} \times f(\rho^*) \tag{5.9}$$

where $\rho^* = \dfrac{\rho_l - \rho_g}{\rho_g}$,

and $f(\rho^*) = 2.157\times10^{-7}(\rho^*)^{-3.2}(1+0.0049\rho^*)^{4.13}$

Bubble departure diameter is calculated as follows:

$$d_{bw} = 2.469\times10^{-5}(\rho^*)^{0.9}\theta\left[\sigma/g(\rho_l - \rho_g)\right]^{0.5} \tag{5.10}$$

In equation (5.10) above, θ is the equilibrium contact angle between the wall and the bubble and has a magnitude of 80°. The surface tension between the liquid and vapour is σ, and g is gravitation acceleration.

The bubble departure frequency, f ,was empirically formulated by Cole (1960: 537) using frame-by-frame measurements of bubble diameter and position using high-speed photography. Its magnitude is determined using the following equation,

$$f = \sqrt{\frac{4\,g(\rho_l - \rho_g)}{3\,d_{bw}\,\rho_l}} \tag{5.11}$$

The heat transfer due to surface quenching depends on both fluid and vapour bubble properties, and accounts for heat expended in the reformation of the thermal boundary layer in areas vacated by bubbles. The quenching heat flux is determined using the equation:

$$q_q = h_q A_b (T_w - T_{l,y^+(const.)}) \tag{5.12}$$

where $h_q = \dfrac{2}{\sqrt{\pi}}\sqrt{K_l \rho_l c_l}\sqrt{f}$

In equation (5.12), h_q is the quenching heat transfer coefficient and $T_{l,y^+(const.)}$ is the liquid temperature at a known one-dimensional distance from the wall y^+. Equation (5.12) assumes that the quenching heat flux is proportional to the temperature difference measured at a known distance from the wall.

Heat and mass transfer occur between the heated wall and the subcooled fluid during subcooled boiling flow. Heat is transferred to the subcooled liquid due to the condensation of the vapour bubbles. Mass flow m_w on the wall due to evaporation, which accounts for bubble birth and mortality, is modelled as per the equation below.

$$m_w = \left(\frac{\pi \times d_{bw}^3}{6} \right) \rho_g \; f \times N_w \tag{5.13}$$

where d_{bw} equals the bubble departure diameter, f equals the bubble departure frequency and N_w is the nucleation site density. Evaporation mass flux is used to determine the evaporation heat flux as shown:

$$q_e = m_w H_{fg} \tag{5.14}$$

where H_{fg} is the latent heat of boiling.

5.3 Interfacial Momentum Transfer

The effect of interfacial forces such as drag, lift, turbulent dispersion and wall lubrication on multiphase flows is captured using the interfacial momentum transfer models. The interfacial drag force R is a function of the velocity dependent bubble drag coefficient, see below equation. Well known empirical correlations used for determining the bubble drag coefficient include the Schiller-Naumann and Ishii and Zuber correlations.

$$R = \frac{3}{4} \frac{C_D}{d_b} \alpha_g \rho_l \left| \vec{u}_g - \vec{u}_l \right| \left(\vec{u}_g - \vec{u}_l \right) \tag{5.15}$$

In equation (5.15) C_D is the drag coefficient, determined using the Ishii model, and d_b is the average bubble diameter.

The other terms in the aforementioned equation are vapour volume fraction (α_g), liquid phase density (ρ_l) and the respective liquid and gas phase velocities (u_l and u_g).

The shear-induced lift force (F_L) is responsible for bubble migration from regions with high fluid velocities to that of lower velocities. It represents the non-homogenous radial void fraction distribution and acts at 90 degrees to the axial flow direction.

$$F_L = \alpha_g C_L \rho_l \left(\vec{u}_g - \vec{u}_l\right) \times \left(\nabla \times \vec{u}_l\right) \tag{5.16}$$

The correlations developed by Moraga or Tomiyama is typically applied to estimate the magnitude of the lift force coefficient (C_L) used to solve equation (5.16).

In order to account for the dispersion of vapour bubbles during two-phase flow a turbulent dispersion force (F_{td}) is used. This force is determined by Favre averaging of the interfacial drag force, equation (5.15), to produce the following relation,

$$F_{td} = -\frac{3 C_D \mu_l}{4 d_b \sigma_t} \left(\vec{u}_g - \vec{u}_l\right) \frac{\nabla \alpha}{1-\alpha} \tag{5.17}$$

where μ_l and σ_t are the liquid phase total dynamic viscosity and turbulent Schmidt number, respectively.

The wall lubrication force (F_{wl}) acts on the detached near-wall bubbles and facilitates movement of vapour from the wall to the bulk flow region. This force is responsible for preventing the accumulation of bubbles on the wall when fluid flows between the wall and the bubble. As for the previous models, an empirical model, this time based on the work of Antal et al (1991: 645), is used in determining its magnitude as follows:

$$F_{wl} = -\frac{\alpha \rho_l \left(\vec{u}_g - \vec{u}_l\right)^2}{d_b} \times \vec{n} \times \max\left(C_1 + C_2 \frac{d_b}{y_w}, 0\right) \tag{5.18}$$

In the above equation the terms C_1 and C_2 has values of -0.01 and 0.05, respectively.

The vapour inside the heated bubble as well as the bubble interface is assumed to be at saturation temperature as the bubble moves into the zone containing subcooled liquid. This temperature differential between the bubble and its surrounds result in interfacial condensation across the bubble wall. The interfacial condensation rate is defined as,

$$\Gamma_{cond} = \frac{h_{if} A_{if} \left(T_{sat} - T_l\right)}{H_{fg}} \tag{5.19}$$

Where the term h_{if} is the interfacial heat transfer coefficient, modelled using the Ranz-Marshall correlation described in the following section, and A_{if} is the interfacial area.

5.4 Interfacial Heat Transfer

The temperature differential between the vapour bubbles and bulk fluid accounts for the heat transfer between the bubble and liquid phases. The determination of this mass independent heat transfer is done using the following equation:

$$q_{if} = h_{if} A_{if} \left(T_g - T_l\right) \tag{5.20}$$

where $h_{if} = Nu \dfrac{k_l}{d_b}$, and h_{if} is the interfacial heat transfer coefficient.

The previously mentioned Ranz-Marshall correlation, equation (5.20) above, is applied in the RPI model to determine the magnitude of the previously discussed Nusselt number. This results in the following (Ranz & Marshall, 1952: 143):

$$Nu = 2 + 0.6\, Re_b^{0.5}\, Pr_l^{0.3} \tag{5.21}$$

Where Re_b equals the bubble Reynolds number and is determined as follows,

$$Re_b = \frac{\rho_l \left|u_g - u_l\right| d}{\mu_l} \tag{5.22}$$

and $\left|u_g - u_l\right|$ is the bubble local slip velocity.

5.5 Turbulence Modelling

The Eulerian multiphase fluid approach introduces an alternate form of the turbulent viscosity term, which now consists of a liquid phase molecular viscosity, a shear induced turbulent viscosity term and a bubble-induced turbulent viscosity term.

$$\mu_l^{eff} = \mu_l + \mu_l^t + \mu_l^b \tag{5.23}$$

In equation (5.23), the omission of a turbulent viscosity term for the gas phase is based on the assumption that in nucleate boiling flow, gas fluctuations will follow that of the liquid phase. The liquid phase turbulence, μ_l^t, is computed using the single phase fluid models discussed earlier (refer to equation (4.9)).

The bubble-induced turbulence viscosity term depicted in equation (5.23) is determined as follows:

$$\mu_l^b = C_{\mu b}\,\rho_l\,\alpha\,d_b\left|\vec{u}_g - \vec{u}_l\right| \tag{5.24}$$

where α is the volume fraction, d_b is the local bubble diameter and $\left|\vec{u}_g - \vec{u}_l\right|$ equals the gas to liquid velocity gradient.

As per the work done by Sato et al (1980: 169), the value of the C_μ term in equation (5.24) amounts to 0.6.

6 NUMERICAL ANALYSIS – SINGLE-PHASE FLUID FLOW AND HEAT TRANSFER IN HELICALLY COILED TUBES

6.1 Introduction

Numerical modelling of flow inside the helical tube to investigate the effects of the secondary flow on heat transfer and pressure drop was done in ANSYS Fluent using the finite volume method. The helical coil does not have any symmetry axis and was subsequently modelled in 3D space. In order to reduce the number of cells and the corresponding computational costs of the numerical model, only two coils of the helical pipe were considered. The resulting CFD model was validated against the Gnielinski correlation used for the development of the 1D steady-state thermal model previously discussed. The results obtained from the empirical correlation and CFD were compared to that of a straight pipe of equivalent length in order to quantify reported increases in heat transfer and pressure drop.

6.2 Straight Tube

6.2.1 Computational Domain

CFD analysis of subcooled water flowing through a straight pipe was investigated to provide a reference case using the Gnielinski correlation. An adiabatic hydrodynamic entrance length of 500 mm, approximately $10 \times d_i$, was added to the inlet of the straight pipe to ensure the establishment of a fully developed velocity profile. Refer to Table 6.1 for pipe dimensions.

Table 6.1: Straight tube geometry

Parameter	Symbol	Unit	Value
Equivalent tube length	L	mm	11363
Tube adiabatic length	L_{ai}	mm	500
Tube outside diameter	d_o	mm	50.8
Tube inside diameter	d_i	mm	42.68

6.2.2 Boundary Conditions

Pipe inlet and outlet boundaries were set to velocity inlet and pressure outlet respectively. The water velocities considered at the inlet of the tube ranged from 0.2 m/s to 2.0 m/s in increments of 0.20 m/s. A pressure outlet boundary condition of 0 kPa was specified for the pipe outlet. Subcooled water with properties specified as per the polynomial functions in equations (6.1) to (6.8) was introduced at the tube inlet.

The inlet water temperature was set to 130 °C, which represents a typical deaerated boiler feedwater inlet temperature. A constant wall temperature boundary condition of T_{sat} + 5 °C was employed for the heat pipe to allow the water to be heated, and a heat flux of $q = 0$ was used for the adiabatic entrance length. Refer to Figure 6.1 for a graphical representation of the computational domain.

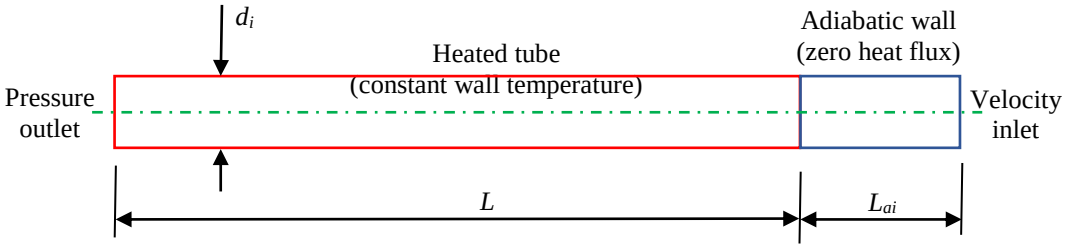

Figure 6.1: Schematic straight pipe domain

6.2.3 Computational Setup

Pressure-velocity coupling was done using the SIMPLE scheme. The second order upwind discretization scheme was used for the momentum, turbulent kinetic energy, dissipation rate and energy equations. A convergence criterion of 1.0×10^{-5} was used for continuity, velocities, k, and ε. The convergence criterion for energy balance was 1.0×10^{-8}.

6.3 Helically Coiled Tube

6.3.1 Computational Domain

The dimensions of the computational domain used in the numerical analysis are presented in Table 6.2 below. For detailed engineering drawings showing sections of the helical coil boiler geometry refer to Appendix E.

Table 6.2: Coil geometry

Parameter	Symbol	Unit	Value
Coil diameter	D_{ic}	mm	1851.8
Coil length	L	mm	11636
Coil Pitch	p	mm	203.2
Pipe Outside Diameter	d_o	mm	50.8
Pipe Inside Diameter	d_i	mm	42.68

6.3.2 Boundary Conditions

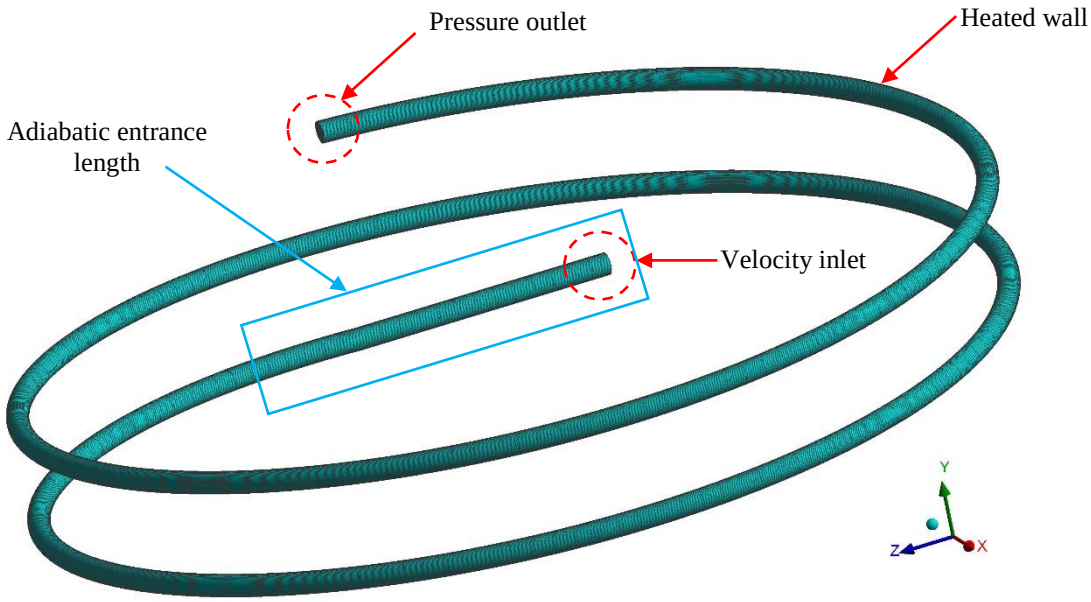

Figure 6.2: 3D mesh of coil showing boundary conditions

Figure 6.2 above illustrates the boundary conditions used for the helically coiled tube. The input parameters for velocity, pressure, temperature and heat flux were identical to that of the straight tube previously discussed.

Before performing the analysis an investigation was conducted into the influence of near-wall treatment on the heat transfer and pressure drop characteristics of the helically coiled tube. Near-wall treatment methods considered for use with the realizable k-ε model were (i) standard wall functions, (ii) non-equilibrium wall functions, and (iii) enhanced wall treatment. The results of the investigation suggested that the enhanced wall treatment method was a closer fit to that of the empirical correlation used. All subsequent runs were done with the enhanced wall treatment method enabled. Findings of the study are presented in Appendix F.

6.3.3 Computational Mesh

A grid independence study of the solution to mesh refinement was conducted prior to carrying out the actual analysis. During the mesh refinement values of wall y-plus were monitored to ensure that they remain within the limits required for the standard wall treatment. The methodology was followed until the results of static pressure, mass flow, heat transfer and outlet temperature became independent of the mesh size. Graphical illustrations of the mesh refinement process can be seen in Figure 6.3. For a summary of results obtained from the grid independence study see Table 6.3 below.

Table 6.3: Grid dependency analysis at water velocity =1 m/s.

		Number of Mesh Refinements					
	Unit	1	2	3	4	5	6
Sweep Divisions	#	300	300	300	300	300	300
Edge Sizing	#	24	32	48	64	80	96
Inflation Layers	#	15	15	15	20	20	20
Cells × 1000	#	137.7	192.6	317.7	563.1	733.8	907.8
Wall Y-plus Value	--	4.202	4.202	4.202	2.381	2.382	2.372
1st Layer Thickness	mm	0.025	0.025	0.025	0.018	0.018	0.018
Mass Flowrate	kg/s	1.322	1.329	1.334	1.335	1.336	1.336
Heat Transfer	kW	25.89	26.02	26.10	25.60	25.60	25.59
Outlet Temperature	K	407.75	407.75	407.75	407.65	407.65	407.65
Static Pressure	Pa	2839.5	2840.6	2842.3	2646.7	2641.9	2639.9

As can be seen in the above table, tube edge divisions larger than 80 did not significantly improve the mass flowrate, heat transfer and outlet temperature of the coil. Therefore, all subsequent calculations were conducted utilising the meshing parameters of mesh number 5.

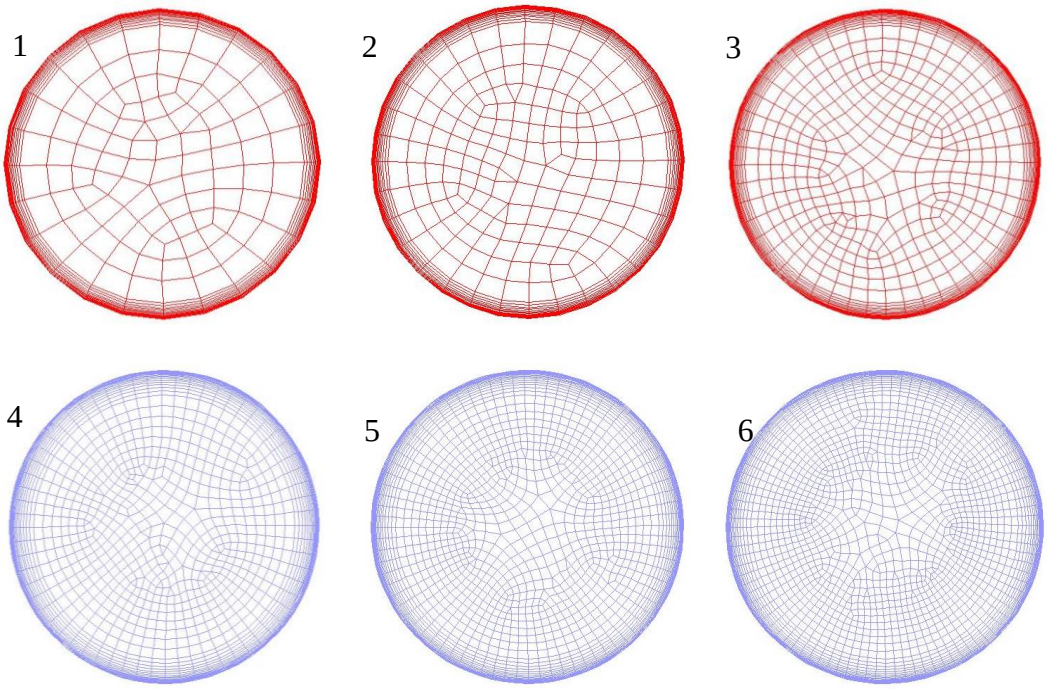

Figure 6.3: Mesh refinement of helical pipe fluid volume

6.3.4 Computational Setup

The discretization schemes utilised were second order upwind for energy, momentum, turbulent kinetic energy and turbulent dissipation rate. The SIMPLEC algorithm with skewness factor of one was applied for coupling of velocity and pressure.

6.4 Fluid Properties

The temperature dependent density, specific heat, thermal conductivity and viscosity of the water flowing within the helical coil tube were modelled in ANSYS Fluent using piecewise polynomial functions. The relationships and ranges of the below polynomials were obtained from a regression analysis of IAPSW-IF97 data for water and steam using GNU Octave. Pressure dependent fluid property effects of water were ignored during the analysis i.e. pressure was taken as saturation pressure.

Valid for the range $403.15 < T < 483.15$,

$$\rho(T) = 1128.532 - 0.538239\,T + 1.205489\times10^{-3}T^2 - 2.63468\times10^{-6}T^3 \quad (6.1)$$

$$c(T) = -1989.416 + 46.57853\,T - 1.206798\times10^{-1}T^2 + 1.082061\times10^{-4}T^3 \quad (6.2)$$

$$k(T) = 1.463815\times10^{-1} + 2.393403\times10^{-3}T - 1.947158\times10^{-6}T^2 - 1.695566\times10^{-9}T^3 \quad (6.3)$$

$$\mu(T) = 5.493693\times10^{-3} - 3.114384\times10^{-5}T + 6.132664\times10^{-8}T^2 - 4.109382\times10^{-11}T^3 \quad (6.4)$$

Valid for the range $483.15 < T < 553.15$

$$\rho(T) = 2712.438 - 10.12065\,T + 2.055498\times10^{-2}T^2 - 1.567642\times10^{-5}T^3 \quad (6.5)$$

$$c(T) = -77299.02 + 498.5589\,T - 1.02564\,T^2 + 7.127134\times10^{-4}T^3 \quad (6.6)$$

$$k(T) = 1.402647 - 5.581645\times10^{-3}T + 1.493183\times10^{-5}T^2 - 1.360578\times10^{-8}T^3 \quad (6.7)$$

$$\mu(T) = 2.256846\times10^{-3} - 1.060332\times10^{-5}T + 1.783578\times10^{-8}T^2 - 1.037173\times10^{-11}T^3 \quad (6.8)$$

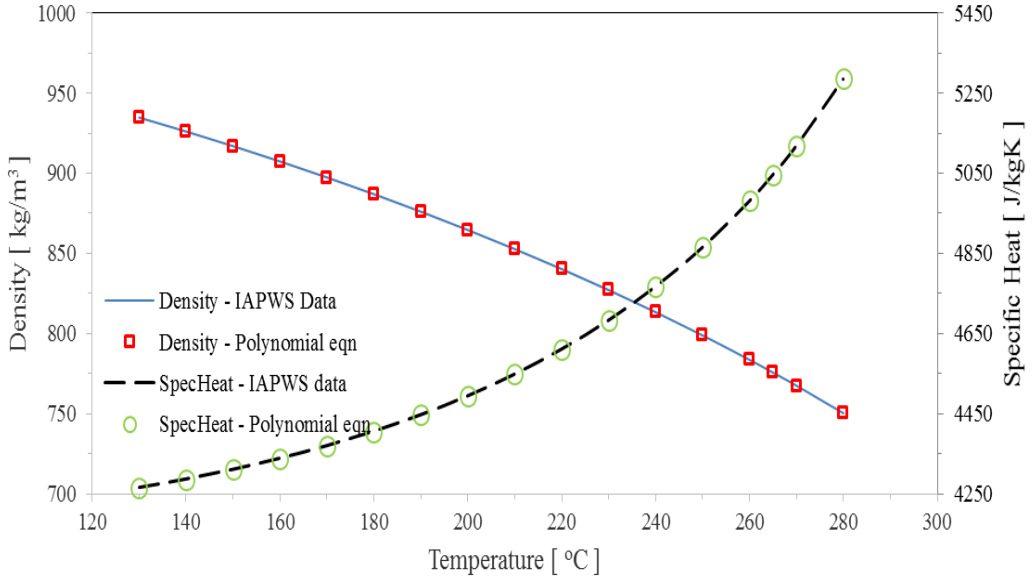

Figure 6.4: Saturated water: Temperature dependent density and specific heat

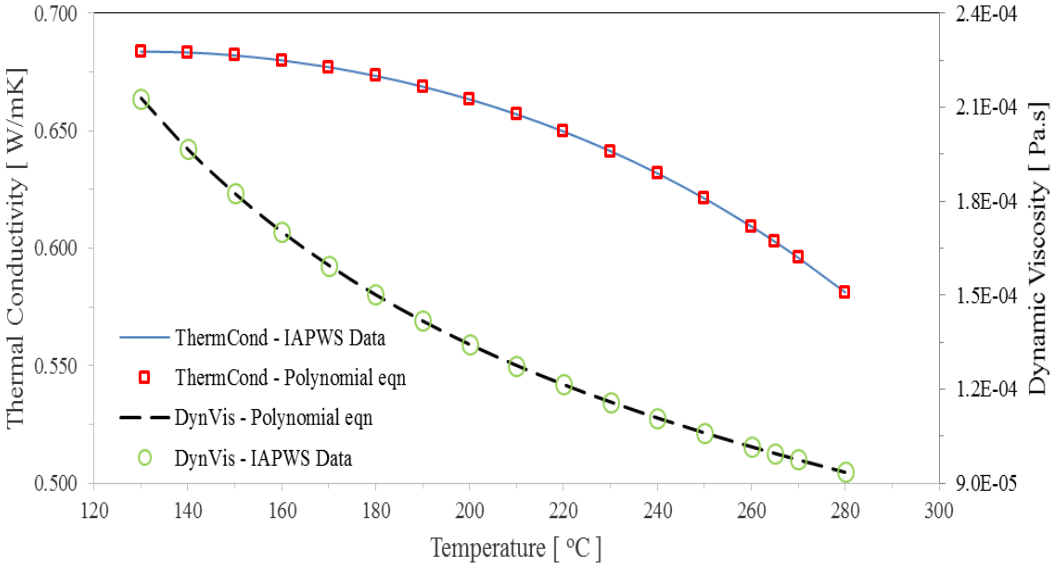

Figure 6.5: Saturated water: Temperature dependent thermal conductivity and dynamic viscosity

Figure 6.4 and Figure 6.5 above, graphically presents the fit of the values derived from the polynomial functions to the IAPWS data points.

6.5 Discussion of Results

The velocity, temperature and pressure profiles for subcooled water flowing at the helical coil exit are presented in Figure 6.6 to Figure 6.8 (where the left side always represent the outer radius of the coiled tube in the figures which follow).

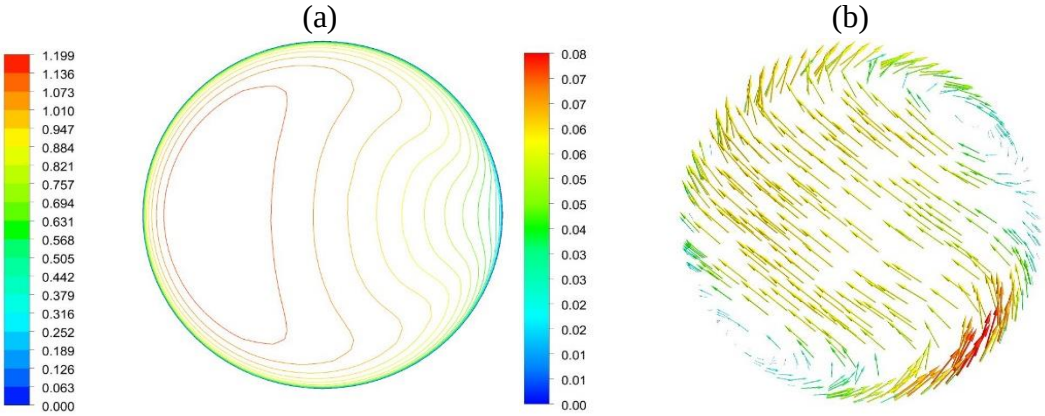

Figure 6.6: Velocity profile (a) and secondary flow (b) at tube exit where water velocity = 1m/s

Figure 6.6 shows the velocity contours at a cross-section in a plane parallel to the coil outlet. Subcooled water enters the coil section after a fully developed velocity profile has been established by the introduction of a hydrodynamic entrance region. Since centrifugal force is a function of the coil geometry and is directly proportional to the square of velocity, fluid flowing in the tube core experience higher centrifugal effects. Therefore, fluid particles with the highest velocities are forced to the outer radius of the coiled tube as a result of the centrifugal force. It can be seen in Figure 6.6 that the location of the maximum fluid velocity is towards the outer radius of the coiled tube. This results in the establishment of a secondary flow pattern which promotes heat transfer and fluid mixing. Fluid mixing in the helical coil is attributed to the rotational motion and reciprocating sideward movements of the fluid particles (Jayakumar, 2012: 318)

Figure 6.7 shows the temperature distribution on the tube periphery at the coil outlet for a fluid velocity of 1 m/s. From the figure it can be observed that the highest wall temperature occurs at the inner radius of the coiled tube. The fluid temperature differential observed at the tube cross section occurs due the variation in the fluid velocity.

This subsequently leads to the lowest heat transfer coefficient being reported at the inner radius of the coiled tube. The variation in the fluid velocity field also results in a pressure field which is skewed by the centrifugal effects. Figure 6.8 reveals that the highest pressure occurs at the coiled tube outer radius. It also shows a much lower pressure at the coil tube inner radius.

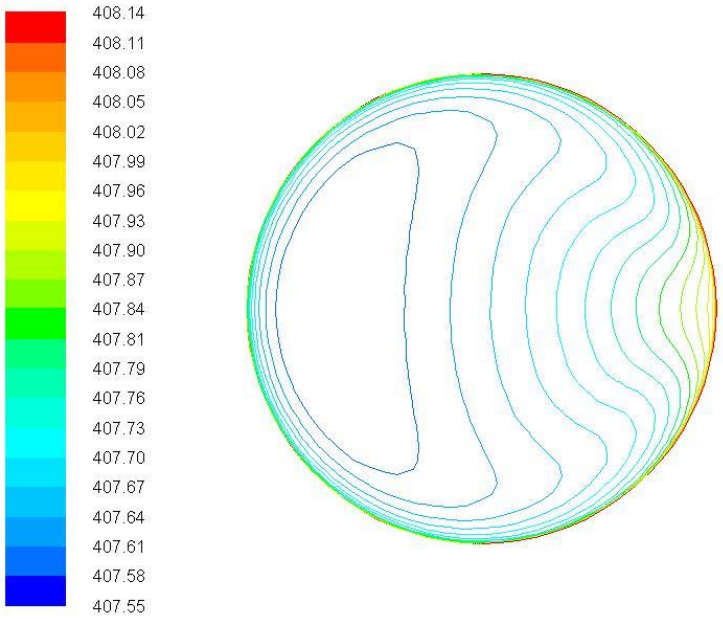

Figure 6.7: Temperature profile at tube exit where water velocity = 1m/s

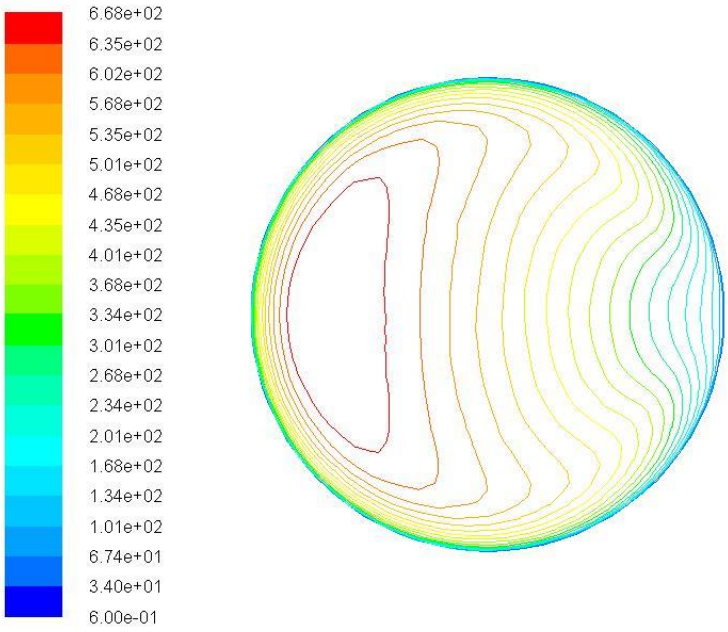

Figure 6.8: Pressure profile at tube exit where water velocity = 1m/s

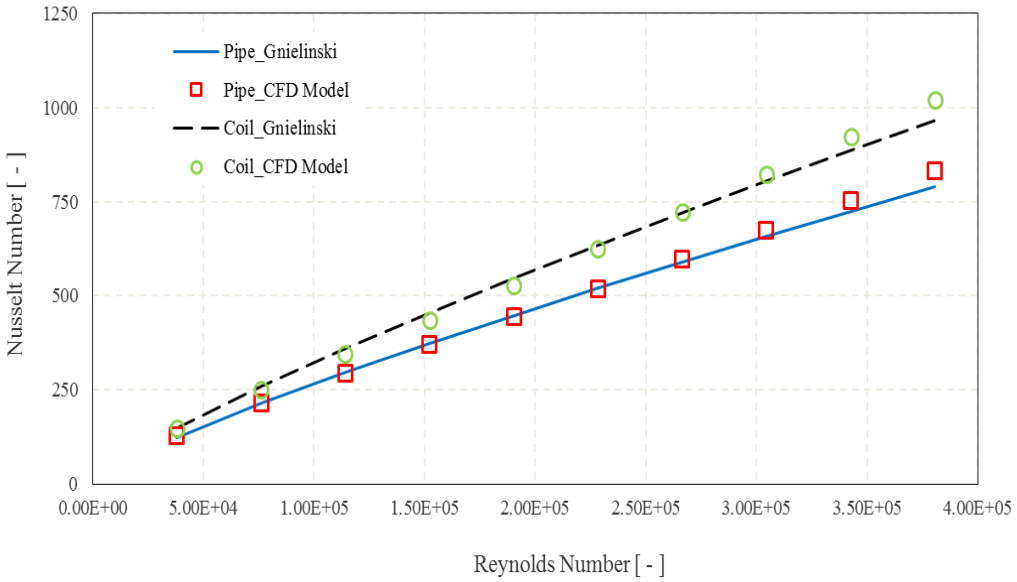

Figure 6.9: Nusselt numbers at varying Reynolds numbers - Straight tube vs. helically coiled tube

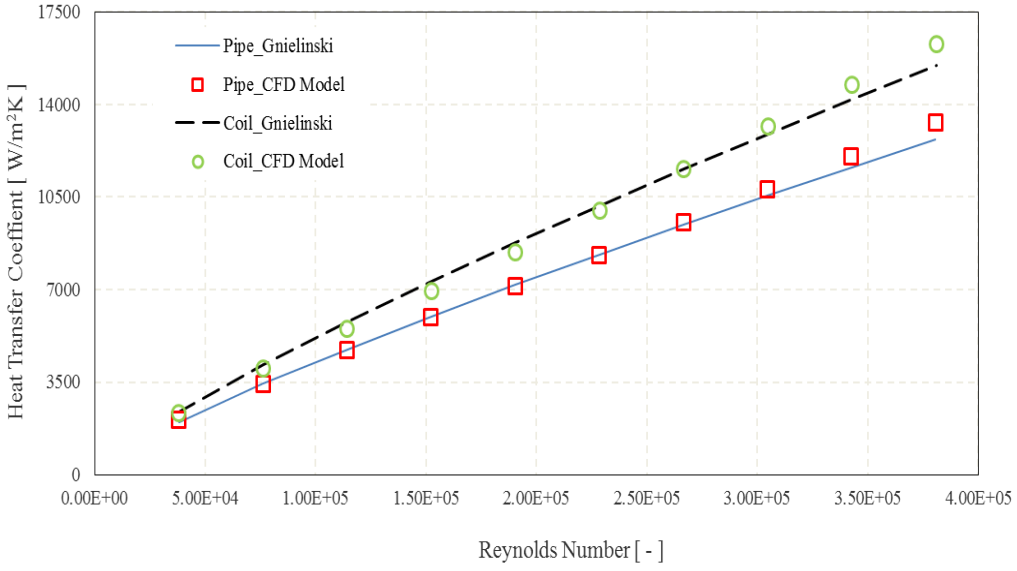

Figure 6.10: Heat transfer coefficients at varying Reynolds numbers - Straight tube vs. helically coiled tube

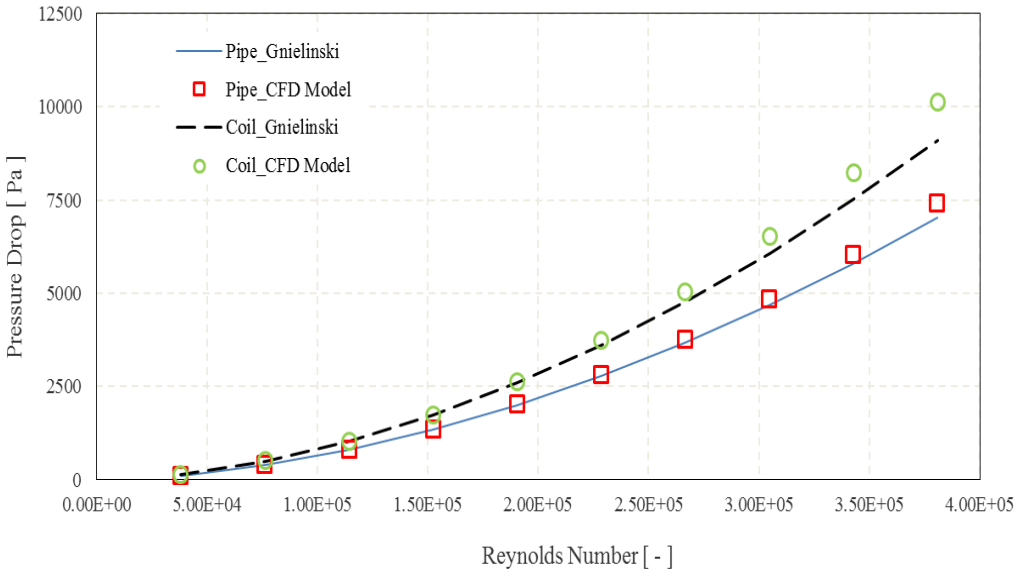

Figure 6.11: Pressure drop at increasing Reynolds numbers – Straight tube vs. helically coiled tube

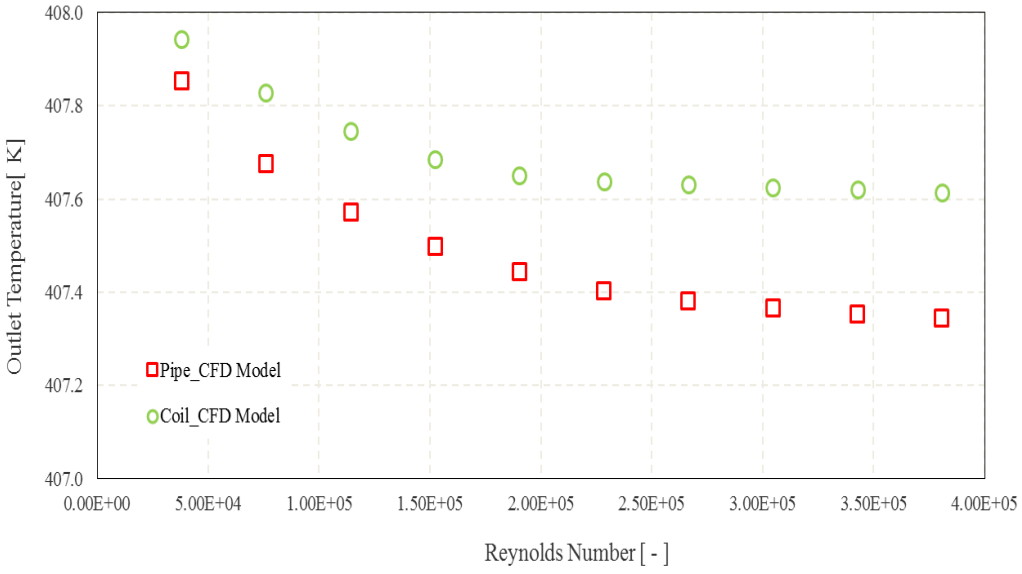

Figure 6.12: Average water temperature at tube outlet for increasing Reynolds numbers – Straight tube vs. helically coiled tube

Figure 6.9 to Figure 6.11 shows the predicted results for Nusselt number, heat transfer coefficient and pressure drop for both the straight tube and the helical coil. The figures draw a comparison between the results obtained from the CFD analysis and those obtained from the Gnielinski correlation at Reynold numbers ranging from 38 000 to 380 000.

From Figure 6.9 and Figure 6.10 we can see that there exists an agreement between the CFD and empirical results with the maximum error being reported as ±5% for both the straight tube and helical coil. It can also be observed that the percentage error between the results of the numerical analysis and the empirical correlation escalates with increases in the Reynolds number until it reaches a maximum at Reynolds number equal to 380 000. Both figures show that the Nusselt numbers and heat transfer coefficients of the helical coil are ± 11% to ± 18% higher than that of the straight tube. As the Reynolds number increases the intensity of the secondary flow also increases which causes the increase in the Nusselt number. This result is in line with the findings reported by others in open literature.

A comparison between the pressure drop of subcooled water flowing inside a straight tube and helically coiled tube is shown in Figure 6.11. The figure reveals that the CFD model of the straight tube was able to more closely reproduce the results of empirical models used at higher Reynolds numbers; with a maximum reported deviation of ± 5%. For the helically coiled tube, the results of the numerical model and the Gnielinksi correlation differed by a maximum of ± 11% for Reynolds number equaling 380 000. However, for Reynolds number of 190 500 at a fluid velocity of 1 m/s, good correlation (± 2% error) was achieved between the numerical and empirical results for the helical tube. As can be observed in Figure 6.11, the calculated pressure drop of the helically coiled tube was ± 17% to ± 27% higher than that of the straight tube.

Figure 6.12 shows the variation in the helical coil outlet water temperature as a function of Reynolds number. As expected we note that the helical coil outlet temperature is higher than that of the equivalent straight tube. The maximum recorded increase in the outlet temperature was 5%, and can be attributed to the enhanced helical coil heat transfer characteristic earlier discussed. The figure also shows reductions in the water outlet temperatures at the higher Reynolds numbers which can be related to the increase in the fluid velocity.

7 NUMERICAL ANALYSIS – TWO-PHASE FLUID FLOW AND HEAT TRANSFER IN HELICALLY COILED TUBES

7.1 Introduction

A crucial step required for the utilisation of the results obtained from CFD simulations is the assessment of the numerical accuracy against experimental data. Flow boiling in vertical pipes has been the subject of numerous experimental and numerical studies by leading scientific and technology institutions. The amount of available research and developmental data makes the comparatively simple case of upward flow boiling in vertical tubes the ideal starting point for the selection of the appropriate closure terms required to characterise the thermal hydraulic behaviour of water flowing inside a helical tube. In this study, the experimental work of Bartolemei, originally used by Kurul and Podowski to validate their RPI wall boiling model (Kurul & Podowski, 1990: 22), is used.

Initially a 3D CFD model for upward flow in a vertical tube was used to determine and validate the selected two-phase model setup parameters which most accurately predict the vapour phase distribution within the pipe. The results of the CFD analysis were then compared to the experimental results of Bartolemei. The focus of the experimental study by Bartolemei was the distribution of vapour volume fraction, velocity and bubble size for the evaporation of water within the vertical tube (Bartolemei & Chanturiya, 1967: 123).

Finally, the model closure terms selected for the case of the vertical tube were used to analyse the two-phase flow boiling characteristics of water inside the helical coil. A 3D CFD model utilising a two-phase fluid approach was implemented in order to characterise the heat transfer and flow patterns inherent in the evaporator section of the helically coiled boiler. The 3D model previously employed for the single-phase fluid case was again applied for the case of the two-phase model.

7.2 Model Validation

7.2.1 Geometry and Mesh

The domain used for the numerical analysis of the reference case was based on the experimental setup of Bartolemei. In his experiments Bartolemei studied the flow boiling heat transfer characteristics of water flowing upwards in a vertical pipe. The pipe inside diameter was set to 15.4 mm whilst the length chosen equalled 2000 mm. A constant heat flux of 570 kW/m^2 was applied to the tube wall by means of electric heaters, whilst the pressure of the water at the inlet was controlled at 4500 kPa. Subcooled water entered the tube inlet with a mass flux of 900 kg/m^2 s and an inlet temperature equalling 200 ^{o}C. This equated to an inlet subcooling temperature of 58.2 ^{o}C.

As was the case with the single-phase flow earlier examined, an unstructured meshing approached was chosen to create a 3D numerical model using hexahedral/quad meshes. The method of inflation layers was again employed to capture the near wall boundary regions. See Figure 7.1 for detail of mesh used.

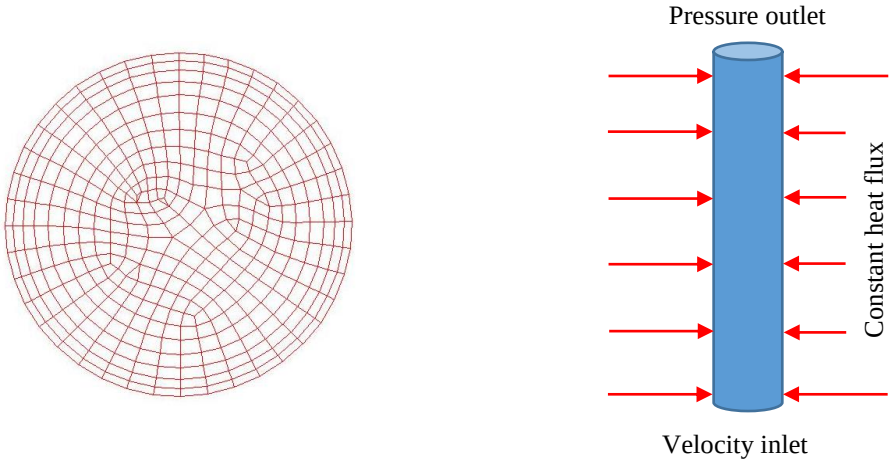

Figure 7.1 Mesh and boundary conditions used for Bartolemei bench case

7.2.2 Simulation Settings

An approach of elimination was systematically applied to investigate the effect of the pertinent model parameters such as lift, drag and turbulent dispersion force in order to investigate their influence on the numerical results. The ability of the selected model to reproduce the experimental results of Bartolemei was done with pressure-velocity coupling set to SIMPLE-Phase Coupled. The simulations were run in the transient state in order to incorporate the time-dependent two-phase flow behaviours. See Table 7.1 for a summary of ANSYS Fluent cases investigated.

Table 7.1: Summary of RPI setup cases.

	Model Simulation Cases			
	Case 1	Case 2	Case 3	Case 4
Phase Interactions: • Drag Coefficient • Lift Coefficient • Turbulent Dispersion • Turbulent Interaction	Ishii Moraga Antal Lopez	Ishii Moraga Antal Burns	Ishii Tomiyama Antal Lopez	Ishii Tomiyama Antal Burns
Wall Treatment	NEWF	NEWF	NEWF	NEWF
Pressure-velocity coupling	SIMPLE	SIMPLE	SIMPLE	SIMPLE
State	Transient	Transient	Transient	Transient

The model parameters of Case 1, refer Table 7.1 above, were best able to reproduce the experimental results obtained by Bartolemei and were used in all subsequent simulations.

Other simulation parameters for the phase interactions were found not to have a significant effect on the model results and were kept at the Fluent default settings. For the mass transfer interaction terms Fluent default values were kept for bubble departure diameter, bubble departure frequency and nucleation site density.

7.2.3 Boundary Conditions

Inlet velocity was set to 1.04 m/s (900 kg/m^2 s) and pressure outlet was specified as 0 kPa. A developed velocity profile obtained from first modelling the setup with a wall heat flux of 0 was used as an input for the inlet boundary condition. A vapour mass fraction of 0% was used at the pipe inlet and a no-slip velocity condition was specified between the liquid and vapour phases. The IAPWS fluid properties discussed in Chapter 6.4 were used to define the thermo-fluid behaviour.

A constant wall heat flux boundary condition of 570 kW/m^2 was used for the heated pipe section with an inlet temperature of 200 ^{o}C. See Figure 7.1 for a schematic of the boundary conditions used.

7.2.4 Relaxation Factors

The analysis was run in Fluent with under-relaxation factors for momentum, pressure and density specified as 1. That of body forces and vapour mass fraction was reduced to 0.3, whilst for VOF, k and ε a value of 0.3 was used. For the energy equation the under-relaxation factor was set to 0.6.

7.2.5 Convergence Criteria

The residual criteria for the equations of momentum, continuity, turbulent kinetic energy, turbulent dispersion rate and volume fraction were set to 1×10^{-5} and monitored for convergence. Due to the transient behaviour of two-phase flow additional convergence criteria, in the form of surface monitors, had to be specified in order to monitor for convergence. These criteria included mass conservation between the pipe inlet and outlet, mass averaged vapour fraction at the outlet and static pressure at the outlet.

7.3 Helically Coiled Tube

7.3.1 Model Setup

The helical model developed for the 3D single-phase study was also used for the two-phase numerical simulations. However, in order to reduce computational effort, Mesh 4 together with the NEWF approach was utilised.

The boundary conditions used were similar to that of the validation model and are presented in Table 7.2. The heat flux chosen was based on DNB calculations for two coil turns of the helical coil (refer to Appendix D for a sample calculation). The selected coil heat flux was deliberately chosen to be in excess of the coil critical heat flux to ensure that DNB would be achieved within the designated coil length. Results from the circulation calculation are presented in Table 7.3. All other computational setup parameters were identical to that used for the bench case of Bartolemei.

Table 7.2: Boundary conditions for two-phase helical coil model

Boundary condition	Type	Unit	Value
Inlet	Velocity	m/s	1
	Temperature	^{o}C	200
	Vapour volume fraction	%	0
	Pressure	kPa	4500
Outlet	Pressure	kPa	0
Wall	Constant heat flux	kW/m^2	750

Table 7.3: Summary of circulation results for two coil turns at a coil heat flux of 750 kW/m^2

	Symbol	Unit	Qty
Water mass velocity	m	kg/m2.s	867.7
Enthalpy coefficient	K_h	--	1.927
Pressure coefficient	K_p	--	0.124
Wall thickness coefficient	K_δ	--	0.588
Inlet vapour mass fraction	α_{in}	--	-0.165
Coil coefficient	K_d	--	1.039
Mass flow coefficient	K_m	--	0.876
Critical vapour mass fraction	α_{cr}	--	0.32
Critical vapour volume fraction		--	0.95
Location of boiling crisis	L_{cr}	m	10.17
Critical heat flux	Q_{cr}	kW/m^2	666.21

7.4 Discussion of Results

7.4.1 Bartolemei Bench Case

Upon validation against the experimental results obtained by Bartolemei it was shown that the RNG k-ε model with non-equilibrium wall function was able to successfully and with acceptable agreement, reproduce the experimental results for subcooled water flowing vertically upwards in a pipe. Figure 7.2 is a contour plot of the temperature distribution along the upper section of the tube wall for the reference case. The figure shows that the vapour distribution at the pipe outlet follows the velocity profile of the steam/water mixture.

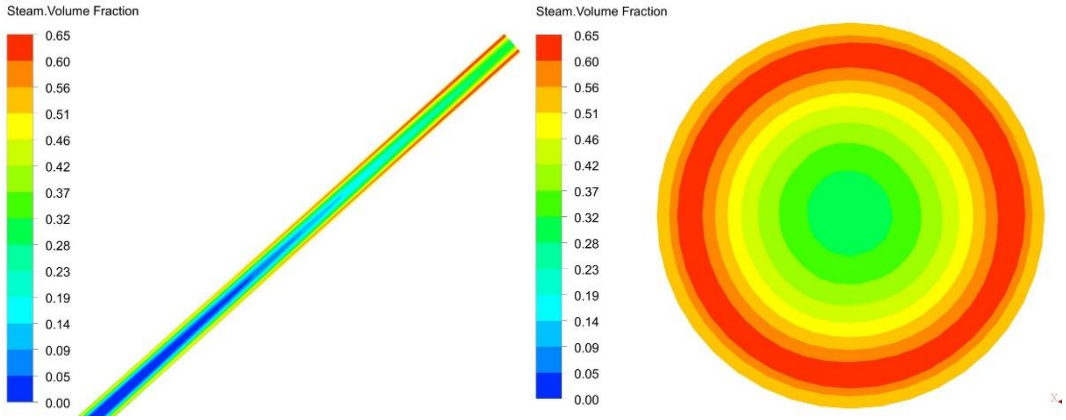

Figure 7.2 Vapour volume fraction plots (a) along the length of the pipe being considered, (b) pipe outlet

One of the most relevant findings of the simulation is the temperature distribution along the heated tube wall (see Figure 7.4). These results reveal close agreement between the bulk fluid and wall temperatures for the RPI model and the reference case. For the experimental setup of Bartolemei, the bulk liquid was found to be in the subcooled state throughout the length of the tube, see Figure 7.4. This suggests that DNB was not achieved and that the flow boiling regimes ranged between the subcooled and nucleate boiling states. A maximum deviation of ±1 and ±2% was recorded for the bulk fluid and wall temperature, respectively.

Also of significance is the vapour volume fraction at the pipe outlet (see Figure 7.3), which up to a length of 1.8 m showed good consistency between the results. In Figure 7.2 and Figure 7.3 it can be observed that the vapour volume fraction at the tube outlet has a minimum value of 0.28, a maximum of 0.65 and average of 0.51.

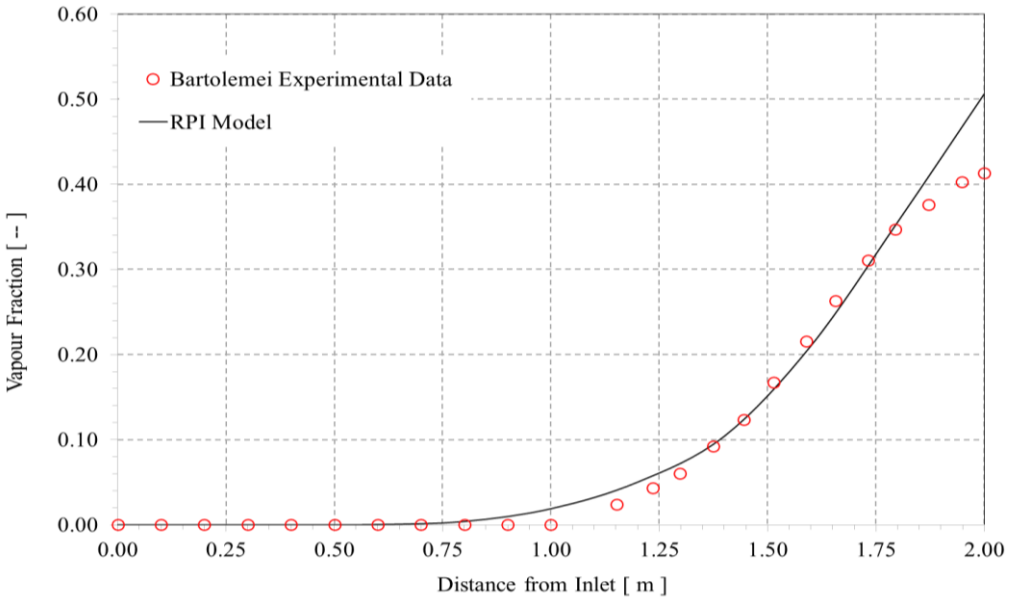

Figure 7.3: Comparison of results for vapour volume fraction along test tube for Bartolemei and CFD using RPI model

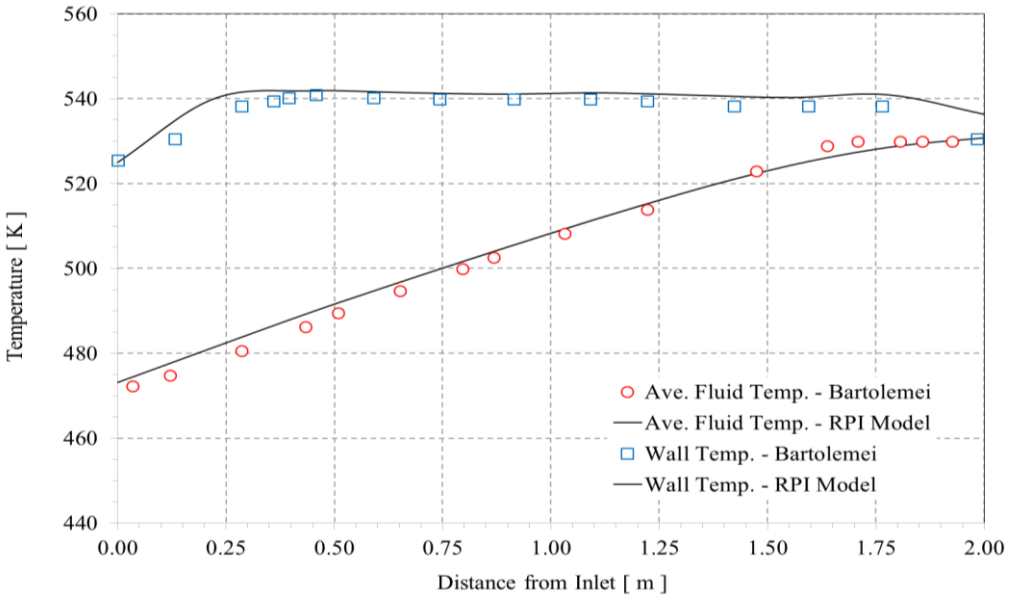

Figure 7.4: Comparison of results for average fluid and wall temperature along test tube for Bartolemei and CFD

7.4.2 Helically Coiled Tube

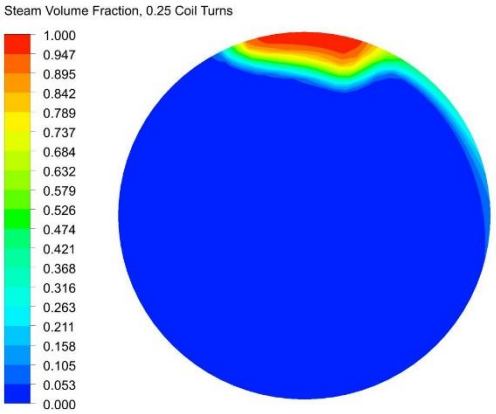

Figure 7.5: Volume fraction at 0.25 coil turns

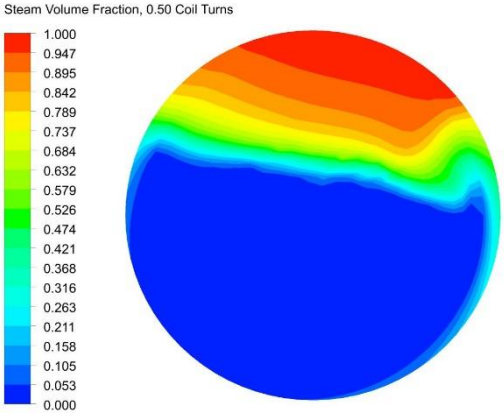

Figure 7.6: Volume fraction at 0.50 coil turns

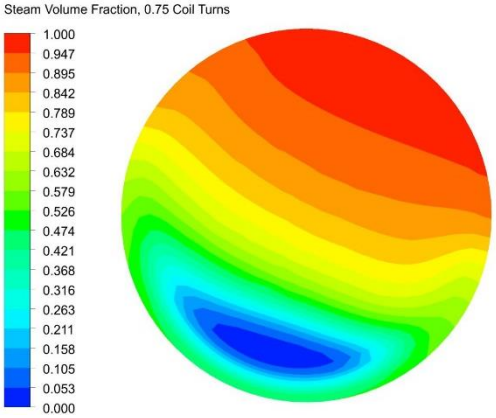

Figure 7.7: Volume fraction at 0.75 coil turns

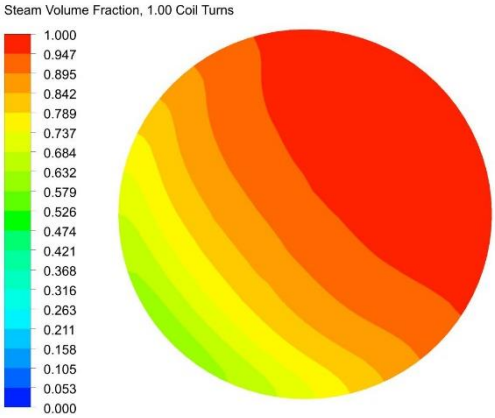

Figure 7.8: Volume fraction at 1.00 coil turns

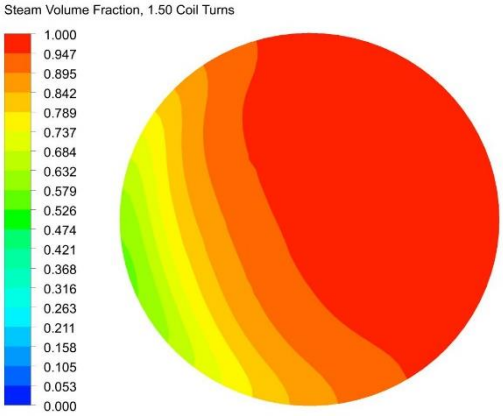

Figure 7.9: Volume fraction at 1.50 turns

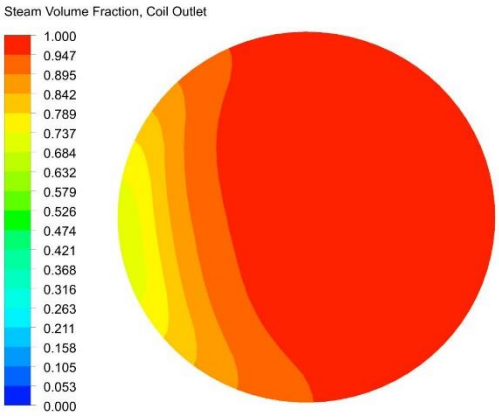

Figure 7.10: Volume fraction at coil outlet

Figures 7.5 to 7.10 show the steam volume fraction and the phase distribution profile on the tube cross section at various locations. The figures indicate that for the vapour volume fractions being studied, gravitational effects are predominant and a separated flow akin to flow in horizontal pipes is established up to a coil length of 0.75 coil turns (Figure 7.5 to 7.6). In Figure 7.5 it can however be seen that vapour starts to form at the top region of the coiled tube inner radius at 0.25 coil turns. At 0.75 coil turns, the effect of the centrifugal force can be seen as the higher density liquid phase is pushed towards the bottom region of the tube outer radius. Further increases in the vapour volume fraction result in the liquid phase accumulating near the bottom region of the tube outer radius. The liquid volume fraction is seen to rapidly reduce as the vapour volume fraction increases.

Figure 7.5 to 7.10 also show that dry out started at the top of the tube. This is due to the large coil diameter which reduced the centrifugal effects. It can be seen that vapour volume fraction increases as the water/steam mixture flows through the coiled section. This is expected as heat is continuously being added to the two-phase mixture due to the constant wall heat flux boundary condition earlier specified. At 0.75 coil turns a vapour volume fraction of 1.00 can be observed at the top of the tube, see Figure 7.7. As the flow progresses further, the vapour volume fraction continuous to increase until it reaches a maximum at the coil outlet, refer Figure 7.7 to Figure 7.9. These figures also illustrate the effect of the gravitational force, which initially retarded dry out at the bottom of the tube by promoting re-wetting of the section.

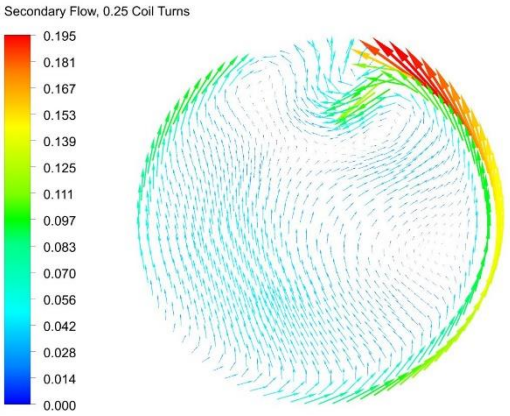

Figure 7.11: Secondary flow at 0.25 coil turns [m/s]

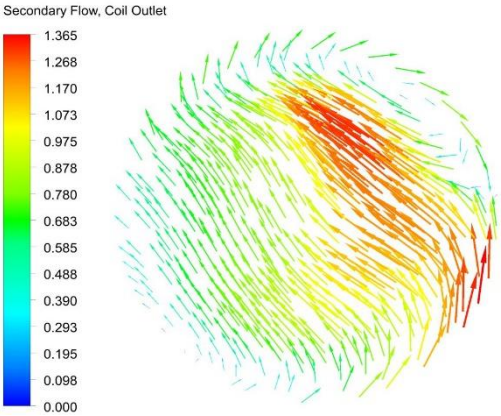

Figure 7.12: Secondary flow at coil outlet [m/s]

Figures 7.11 and 7.12 show that for the vapour volume fractions being studied the secondary flow is characterised by a single vortex. The size of the vortex in seen to increase with increases in vapour volume fraction. In Figures 7.11 and 7.12 it can be seen that the secondary flow promotes movement of liquid from the bottom region towards the inner radius of the tube, thereby ensuring constant rewetting of the region at the inner tube radius.

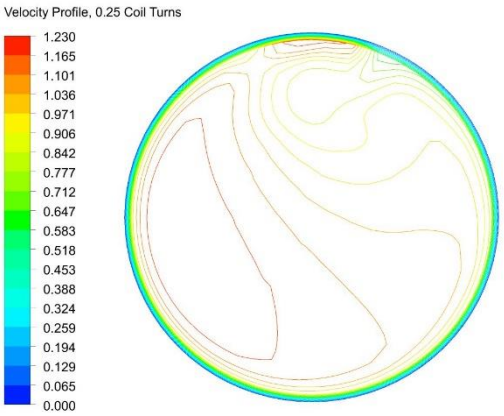

Figure 7.13: Velocity profile at 0.25 coil turns [m/s]

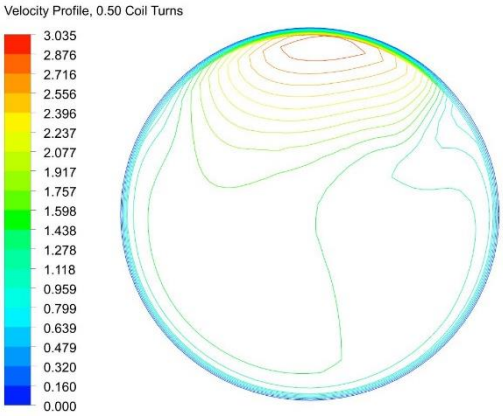

Figure 7.14: Velocity profile at 0.50 coil turn [m/s]

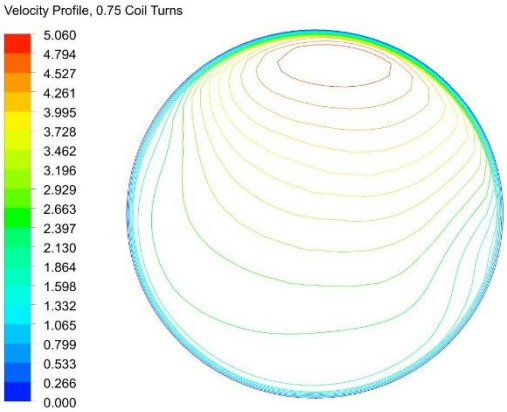

Figure 7.15: Velocity profile at 0.75 coil turns [m/s]

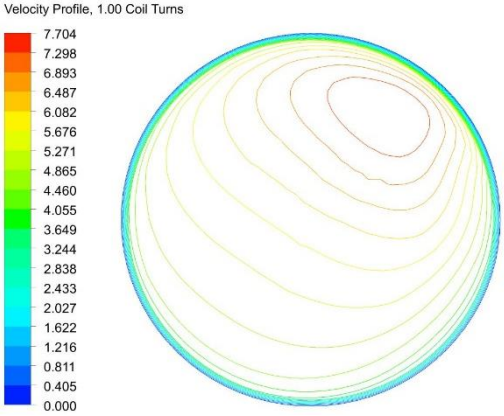

Figure 7.16: Velocity profile at 1.00 coil turns [m/s]

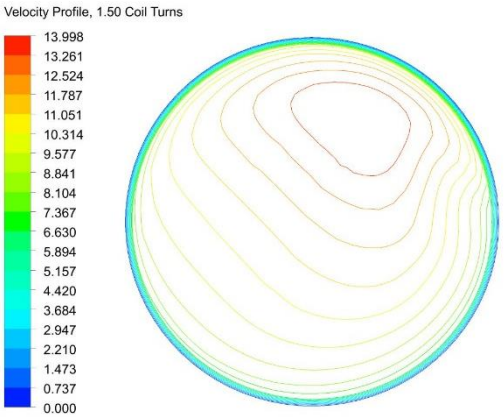

Figure 7.17: Velocity profile at 1.50 coil turns [m/s]

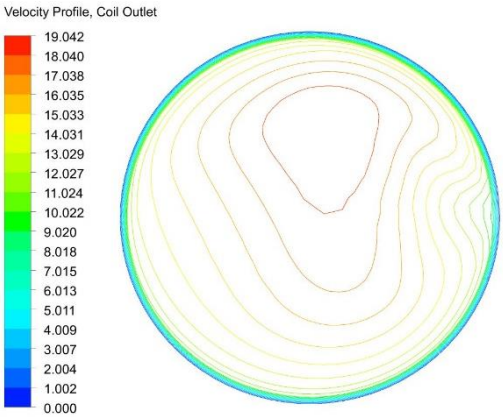

Figure 7.18: Velocity profile at coil outlet [m/s]

At low vapour volume fractions, the velocity profile is dominated by the velocity of the liquid phase flowing at the outer radius of the coiled tube (Figure 7.13). At this stage centrifugal forces are seen to have a noticeable influence on the liquid phase and the liquid phase is concentrated in the outer radius of the coiled tube. Also of significance is the development of the high-velocity vapour phase at the upper wall of the tube. The vapour volume fraction is seen to increase as the flow field develops. This results in the maximum velocity being shifted towards the upper region of the tube (Figure 7.14 to Figure 7.18). This shift in the location of the maximum velocity will continue until the velocity profile approaches that of single-phase flow at the maximum vapour volume fraction.

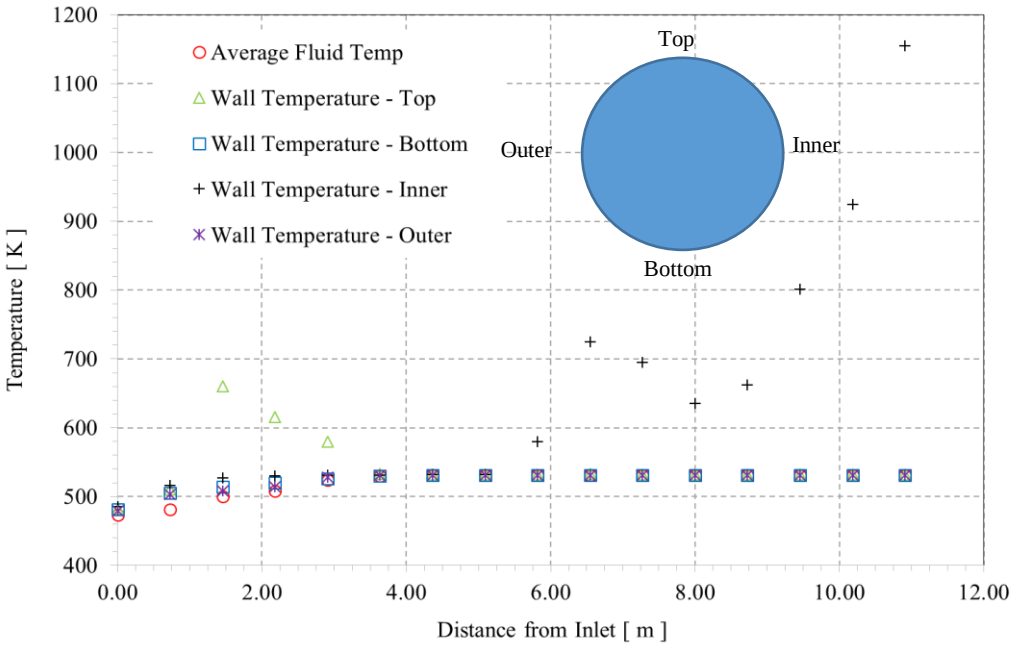

Figure 7.19: Comparison of results for average fluid and wall temperatures along length of helical coil

One of the most important outputs from the numerical simulations is the temperature distribution along the wall of the helical tube. Figure 7.19 plots the temperature distribution along the length of the coiled section at the top, bottom, inner and outer positions of the tube. As envisaged, the centrifugal effects result in the maximum tube wall temperature being reported at the inner radius of the coiled tube. However, in Figure 7.19 an initial maximum wall temperature of 660 K can be observed at the top of the helically coiled tube at a distance of 1.45 m or 0.25 coil turns. This increase in tube wall temperature suggests a wall superheat of 130 ^{o}C, which indicates a preliminary occurrence of DNB. This event is generally referred to as intermittent DNB and is typical of nucleate boiling flow in horizontal tubes.

The secondary flow effects, refer Figure 7.11, are seen to promote rewetting of the top of the tube and the wall temperature starts to reduce until it coincides with that of the bottom, inner, outer and central tube regions.

From a coil length of 3.7 m to 5.1 m the tube wall temperatures correspond with the water/steam saturation temperature. At a coil length of 5.8 m a sudden increase in the wall temperature can be observed at the tube inner radius (Figure 7.19). This change in temperature can be attributed to the formation of vapour slugs and the subsequent dispersed phase flow, which inhibits cooling of the tube wall. A maximum temperature difference of 195 ^{o}C occurs between the bulk fluid and the inner tube wall at a coil length of 6.55 m. This results in a wall superheat of 195 ^{o}C, which is significantly higher than the 30 ^{o}C wall superheat limit for DNB reported in literature and suggests the occurrence of the initial boiling crisis. Figure 7.19 also shows a maximum tube wall temperature of 1155 ^{o}C for the inner tube radius at the coil outlet. The shape of the inner tube wall temperature profile is seen to follow that of the boiling curve for saturated liquid, Figure 2.8, discussed earlier.

The results from the CFD simulations predicted an initial boiling crisis which occurred earlier than anticipated by the Ünal model. For DNB the empirical correlation predicted the location of a boiling crisis at 10.17 m, whilst the numerical model estimated a distance of 6.55 m. This corresponds to a deviation of 35.6% between the results of the CFD simulation and that of the Ünal correlation.

8 CONCLUSION AND RECOMMENDATIONS

This report detailed a 1D steady-state thermal model, which was based on the empirical correlation formulated by Gnielinski, to design a high pressure helically coiled boiler capable of producing 10 tonnes per hour of superheated steam at 45 bar and 380 ^{o}C. The thermal model developed is used to determine the required heat transfer surface areas and the resultant pressure drop of the boiler economiser, evaporator and superheater sections. Heat transferred in the different boiler sections was found to be 445.6 kW for the economiser, 2289.5 kW for the evaporator and 1049.2 kW for the superheater. The subsequent boiler geometry was used to detail the manufacturing drawings required for fabrication of the prototype boiler.

The critical heat flux of the helically coiled boiler was also estimated using the two-phase flow correlations of Ünal. The boiler circulation rate required to avoid DNB was found to be 1.4 times the boiler design evaporation. This was equivalent to a coil heat flux of 77.93 kW/m^2 at a coil length of 213.3 m. However, CFD results based on the RPI model showed that the location of the first boiling crisis occurs earlier that anticipated by the empirical correlation. Applying the findings of simulation to the 1D model resulted in a shift of DNB to a coil length of 137.6 m. This knowledge of the required boiler circulation rate will be used to size the boiler feed water pumps.

The design employed CFD modelling as a design tool in order to quantify reported increases in the heat transfer and pressure drops of the helically coiled tubes, and characterise the thermal hydraulic fluid behaviour within the helically coiled tubes by modelling two coil turns of the boiler. As a starting point, single-phase flow inside in the helically coiled tube was considered. This was then followed by two-phase flow where the DNB phenomenon was the main subject of interest.

Single-phase flow results between the empirical and the CFD model revealed good agreement. In fact, the average deviation between the results of the numerical simulation and empirical correlation was found to be 5% with respect to Nusselt number and heat transfer coefficient. The simulation results highlighted the effect of the centrifugal force, which resulted in a secondary flow due to a shift of the maximum velocity field towards the outer wall of the coil tube. The secondary flow was found to have a major effect on both the coil heat transfer coefficient and pressure drop for the case of single-phase flow.

Findings for two-phase flow was based on the Eulerian approach, incorporating the RPI wall heat flux partitioning model. The model closure terms used were selected subsequent to detailed validation of the CFD model against the experimental results of Bartolemei. CFD and experimental results for vapour volume fraction, fluid bulk and wall temperature were compared and were found to be in good agreement. Upon validation of the selected two-phase model, the simulation of the two-phase flow inside the helically coiled evaporator was conducted.

The CFD study enabled a detailed description of phase distribution inside the helically coiled tube being considered, which allowed for a more in-depth description of the wall temperature profile.

This in turn permitted more accurate identification of the location of the final boiling crisis. As originally anticipated, as well as reported in open literature, the location of the boiling crisis was found to occur at the inner radius of the helically coiled tube. However, it was seen that prior to the initial DNB phenomenon, an intermittent DNB was observed at the top of the tube. This occurred at 0.25 coil turns and amounted to a wall superheat of 130 ^{o}C. The identification of both an initial and final boiling crisis was in agreement with theory in literature, which stated that this event is unique to straight tubes and helical coils. The DNB phenomenon was also found to occur earlier than estimated by the Ünal model. In fact, the results from the CFD suggest that DNB ensues approximately 3.6 m earlier than predicted by the Ünal correlation.

Any simulation work conducted in this study using software should be considered preliminary and requires extensive experimental validation once the prototype boiler has been installed and commissioned.

9 FUTURE WORK

Future work will be focussed on the finalisation of the refractory lined combustion furnace. Once the furnace has been detailed and manufactured a suitable site will be identified and the prototype boiler installed and commissioned. Following the commissioning of the complete boiler, it is suggested that a series of field tests be conducted on the helically coiled steam generator component. Tests will include verification of heat transfer performance, validation of the pressure drop calculations, profiling of the steam vapour fraction along the length of the helically coiled tube and the identification of the location of the first boiling crisis. Of particular importance will be the experimental verification of the boiler circulation rate needed to prevent DNB.

Another aspect would be to evaluate the accuracy of the CFD results obtained in this study against actual field test results. This will eliminate any incorrect assumptions made during this study and will enable confident evaluation of other thermal hydraulic fluid behaviours inside the helically coiled tube. Of interest would be the effect that changes in coil geometry has on heat transfer, two-phase pressure drop and the bubble size distribution inside the coil tube.

As the focus of this work was the design of the helically coiled boiler and the estimation of the CHF, it is suggested that the model is extended to a conjugate CFD model in order to model the effect of gas side heat transfer and tube thermal conductivity on the boiler thermal properties.

10 REFERENCES

ANSYS Inc. 2013. *ANSYS Fluent Theory Guide, Release 15.0*. Unpublished.

Antal, S.P., Lahey Jr, R.T. & Flaherty, J.E. 1991. Analysis of Phase Distribution in Fully Developed Laminar Bubbly Two-phase Flow. *International Journal of Multiphase Flow,* 17: 635-652.

Auracher, H. & Herbst, O. 2010. Critical Boiling States in Flowing Liquids in VDI-Gesellschaft Verfahrenstechnik und Chemieingenieurwesen (ed.) *VDI Heat Atlas 2nd Edition.* Heidelberg: Springer-Verlag. 832-868.

Bakker, A. 2006. Lecture 3- Conversation Equations: Applied Computational Fluid Dynamics. [Online]. Available: http:/www.bakker.org. [29 July 2016]

Bartolemei, G.G. & Chanturiya, V.M. 1967. Experimental Study of True Void Fraction When Boiling Subcooled Water in Vertical Tubes. *Thermal Engineering,* 14(2): 123-128.

Charry Leon, C.H. 2014. Numerical Simulation of water-cooled sample holders for high-heat flux testing of low-level irradiated materials. Unpublished Thesis, Georgia Institute of Technology, December 2014.

Clark, L. S. 1999. Coil-type steam generators for heating plant applications – Design and feedwater considerations for coil-type steam generators. *Heating/Piping/Air Conditioning,* 71-76, September.

Cole, R. 1960. A Photographic Study of Pool Boiling in the Region of the Critical Heat Flux. *American Institute of Chemical Engineering Journal,* 6: 533-542.

De Kock, J.W. 1986. Report 86005: Chaingrate Stoker Performance. Unpublished Report, John Thompson Africa, Bellville.

Del Valle, V.K. & Kenning, D.B.R. 1985. Subcooled flow boiling at high heat flux. *International Journal of Heat and Mass Transfer*, 28: 1907-1920.

De Vos, D. 2014. Analysis: How much more electricity generating capacity does South Africa need? [Online]. Available: http://www.dailymaverick.co.za/article/2014-7-15-analysis-how-much-more-electricity-generating-capacity-does-south-africa-need/#.vun9U2dumUk.html. [2014, July 15].

Electricity generated and available for distribution. [S.a]. [Online]. Available: http://www.statssa.gov.za/?p=4045.html. [2016, March 01]

Elsayed, A.M. 2011. Heat Transfer in Helically Coiled Small Diameter Tubes for Miniature Cooling Systems. PhD Thesis, University of Birmingham, September 2011.

Elsayed, A., Al-dadah, R.K., Mahmoud, S. & Rezk, A. 2014. Numerical investigation of turbulent flow heat transfer and pressure drop of Al2O3/water nanofluid in helical coiled tubes. *International Journal of Low-Carbon Technologies,* 0: 1-8.

Gnielinski, V. 2010. Heat Transfer in Helically Coiled Tubes in VDI-Gesellschaft Verfahrenstechnik und Chemieingenieurwesen (ed.) *VDI Heat Atlas 2nd Edition.* Heidelberg: Springer-Verlag. 710-711.

Gnielinski, V. 2010. Heat Transfer in Cross-flow Around Single Rows of Tubes and Through Tube Bundles in VDI-Gesellschaft Verfahrenstechnik und Chemieingenieurwesen (ed.) *VDI Heat Atlas 2nd Edition.* Heidelberg: Springer-Verlag. 725-729.

IAWPS. 2010. *Revised Release on the IAPWS Industrial Formulation 1997 for the Thermodynamic Properties of Water and Steam (2010).* [Online]. Available: http://www.iapws.org

Jayakumar, J.S., Mahajani, S.M. & Mandal, J.C. 2008. Experimental and CFD estimation of heat transfer in helical coiled heat exchangers. *Chemical Engineering Research and Design,* 86: 221-232.

Jayakumar, J.S. 2012. Helical Coiled Heat Exchangers, Heat Exchangers – Basics Design Applications. Mitrovic, J (Ed). InTech. [Online]. Available: http://www.intechopen .com/books/heat-exchangers-basics-design-applications/helically-coiled-heat-exchangers.html. [10 March 2015].

Kader, B.A. 1979. Temperature and Concentration Profile in Fully Turbulent Boundary Layers. *International Journal of Heat and Mass Transfer*, 24: 1541-1544.

Kays, W.M., Crawford, M.E. & Wiegand, B. 2005. *Convective Heat and Mass Transfer 4th Edition.* New York: McGraw Hill.

Kharat, R., Bhardwaj, N. & Jha, R.S. 2009. Development of heat transfer coefficient correlation for concentric helical coil heat exchanger. *International Journal of Thermal Sciences,* 48: 2300-2308.

Kleiber, M & Joh, R. 2010. Properties of Pure Fluid Substances in VDI-Gesellschaft Verfahrenstechnik und Chemieingenieurwesen (ed.) *VDI Heat Atlas 2nd Edition.* Heidelberg: Springer-Verlag. 301-393.

Kocamustafaogullari, G. & Ishii, M. 1983. Interfacial Area and Nucleate Site Density in Boiling Systems. *International Journal of Heat and Mass Transfer*, 26: 1377-1387.

Kurul, N & Podowski, M.Z. 1990. Multidimensional Effects in Forced Convection Subcooled Boiling. "*Ninth International Heat Conference*, Jerusalem, Israel, 1-BO-04, 21-26.

Magasiner, N. 1966. Boiler Design and Selection in the Cane Sugar Industry. *Proceedings of The South African Sugar Technologists' Association*, 29-63.

Marshall, E.M. & Bakker, A. 2001. Computational Fluid Mixing. *Fluent Technical Notes*, T144, January.

Mills, A.F. 1995. *Basic Heat and Mass Transfer*. Los Angeles: R.R Donnelley & Sons Company.

Mitchta, E. 2011. Modelling of Subcooled Nucleate Boiling with OpenFoam. Master's Thesis, Royal Institute of Technology, Stockholm.

Oh, J., Ye, I., Park, S., Ryu, C. & Park, S.K. 2014. Modelling and analysis of a syngas cooler with concentric evaporator channels in coal gasification process. *Korean Journal of Chemical Engineering*, 31(12): 2136-2144.

Rahimi, M.R., Askari, A. & Ghanbari, M. 2014. Hydrodynamics of isothermal upward two phase flows in helical coils. *Petroleum and coal*, 56(5): 562-571.

Raj, R.T.K., Kumar, M.S., Mathew, A.C. & Elango, T. 2014. Numerical analysis of helically coiled heat exchanger using CFD technique. *ARPN Journal of Engineering and Applied Sciences*, 9(3): 300-307.

Ranz, W.E. & Marshall, W.R. 1952. Evaporation from drops. *Chemical Engineering*, 48(3): 141-146.

Sato, Y., Sadatomi, M. & Sekoguchi K. 1981. Momentum and Heat Transfer in Two-Phase Bubble Flow –I, Theory. *International Journal of Multiphase Flow*, 7: 167-177.

Stephan, P. 2010. Fundamentals of Heat Transfer in VDI-Gesellschaft Verfahrenstechnik und Chemieingenieurwesen (ed.) *VDI Heat Atlas 2nd Edition.* Heidelberg: Springer-Verlag. 18-29.

Tu, J., Yeoh, G. & Liu, C. 2013. *Computational Fluid Dynamics 2nd Edition*. Oxford: Butterworth-Heinemann.

Ünal, H.C. 2012. Some Aspects of Two-phase Flow, Heat Transfer and Dynamic Instabilities in Medium and High Pressure Steam Generators. PhD Thesis, Technical University of Delft, March 1981.

Versteeg, H.K. & Malalasekera, W. 2007. *An Introduction to Computational Fluid Dynamics: The Finite Volume Method, 2nd Edition*. Harlow: Pearson-Prentice Hall.

Wilcox, D.C. 2010. *Turbulence Modelling for CFD 3rd Edition*. California: DCW Industries Inc.

Wilcox, M.P. 2012. Modelling of Subcooled Boiling in a Nuclear Reactor Core. Master's Thesis, Rensselaer Polytechnic Institute, December 2012.

APPENDIX A: FUEL ANALYSIS – SA GRADE C-SMALLS COAL

Ultimate Analysis	**% by Mass**
Moisture	2,70
Ash	18,22
Carbon	65,03
Hydrogen	3,43
Nitrogen	1,70
Sulphur	0,66
Oxygen	8,26

Proximate Analysis*	**% by Mass**
Moisture	2,70
Ash	18,22
Volatile Matter	24,84
Fixed Carbon	54,24
Gross Calorific Value MJ/kg	26,0

*Air Dried Basis

Ash Fusion Temperatures	**°C**
Deformation	+ 1 400
Hemispherical	+ 1 400
Flow	+ 1 400
Swelling Index	1

Size Grading	**%**
Size range (mm)	% in range
+ 25	0
- 25 to + 19	4
- 19 to +13	11
- 13 to + 6	30
- 6 to + 3	25
- 3 to + 1	20
- 1	10

Trace Elements

There are four trace elements in coal which have an effect on the utilisation of the boiler and stoker. These are as follows:

(a) Chlorine

(b) Phosphorous

(c) Sulphur

(d) Iron

High, normal and low figures for these elements are given below:

Impurities in Coal		**APPENDIX A: Range**		
		High	**Medium**	**Low**
Chlorine	(%)	Greater than 0,3	0,15 – 0,3	Less than 0,15
Phosphorous	(%)	Greater than 0,1	0,1 – 0,03	Less than 0,03
Sulphur	(%)	Greater than 1,8	1,3 – 1,8	Less than 1,3
Iron (in ash)	(%)	Greater than 8,0	4,0 – 8,0	Less than 4,0

Notes

1. Problems will most certainly be experienced with coals containing a high level of impurities
2. Problems might possibly occur with coals containing a medium level of impurities
3. Problems should not occur with coals containing a low level of impurities

APPENDIX B: SCHEMATIC OF A HELICAL COIL BOILER

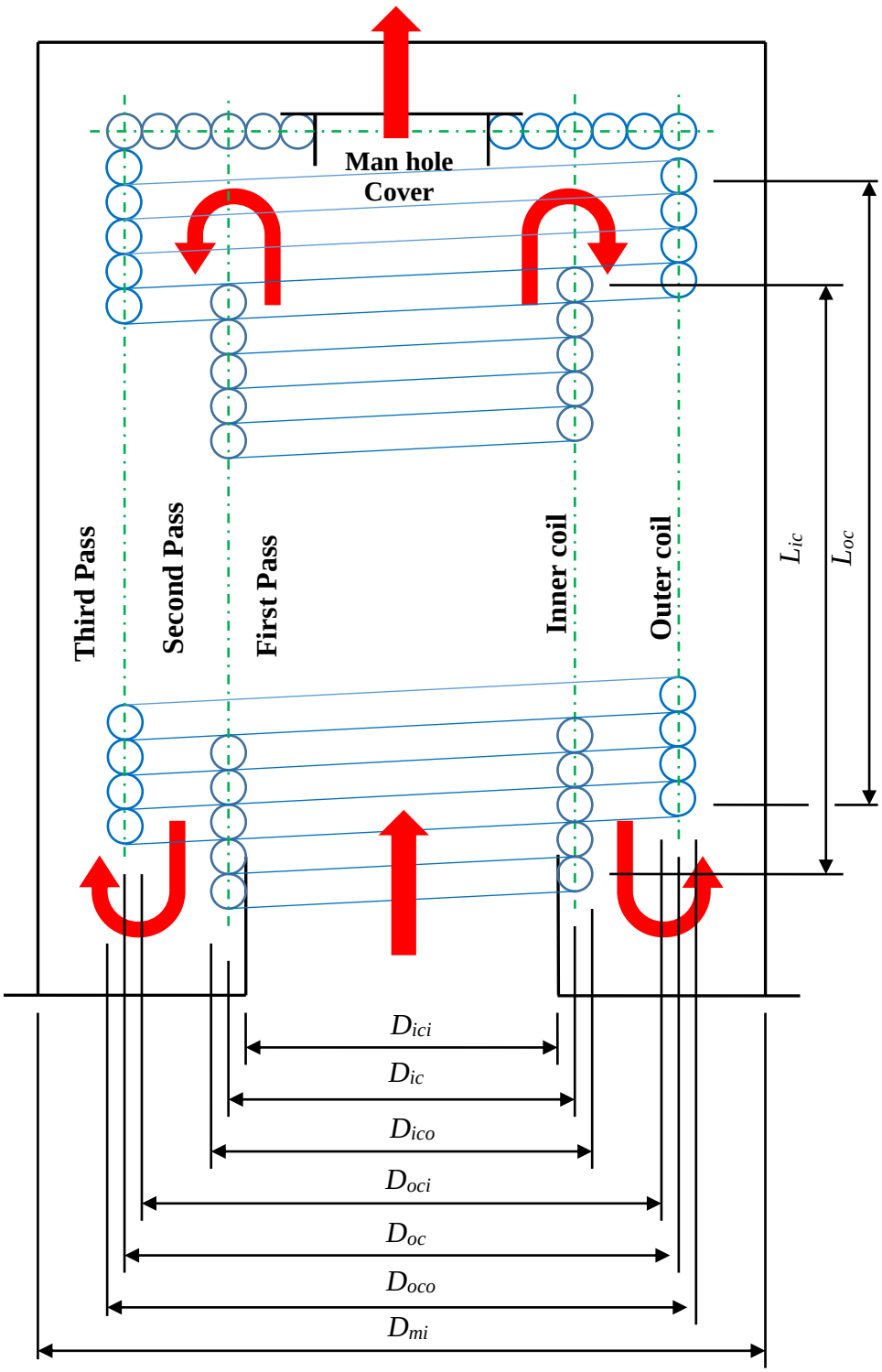

Figure B.1: Three pass helical coil boiler geometry

APPENDIX C: SAMPLE CALCULATIONS OF THE BOILER THERMAL DESIGN

C.1. Boiler Design Basis

Superheater: Design rating	= 10500 kg/hr (F&A 100ºC)
Operating pressure	= 4500 kPa
Operating temperature	= 380 ºC
Boiler load	= 100% of design rating
Final dry gas CO2	= 12%
Fuel	= Transvaal Grade "C" Smalls
Fuel GCV	= 24583 kJ/kg (As-fired)
Fuel NCV	= 23670 kJ/kg (As-fired)
Altitude	= 1800 masl
Stoker type	= Thompson Triumph chaingrate
Stoker model	= TT1050
Maximum stoker grate rating	= 220 kg/m^2 hr
Final exit temperature	= 278.2 ºC (guessed)
Thermal efficiency on GCV	= 69.92% (guessed)

C.2. Boiler Mass Balance

Rated boiler output

$$= \frac{m_{steam} \times \Delta H}{3600}$$

$$= \frac{10500 \times 2256.7}{3600}$$

= 6582 kW

Mass of fuel burnt, m_f

$$= \frac{m_{steam} \times \Delta H}{\eta_{GCV} \times GCV}$$

$$= \frac{10500 \times 2256.7}{0.6992 \times 24583}$$

= 1378.5 kg/hr

Air mass flowrate, m_{am}

= m_f × Mass of air req'd /kg fuel burnt

= 1378.5 × 11.5

= 15809 kg/hr

Gas mass flowrate, m_g

= m_f × Mass of products /kg fuel burnt

= 1378.5 × 12.42

= 17118 kg/hr

C.3. Furnace Design

C.3.1 Heat Transfer by Radiation

Furnace diameter (Inside), D_{ici} = 1800 mm

Furnace mean diameter, D_{ic} = 1851 mm

Tube outside diameter, d_o = 50.8 mm

Number of tubes per coil, $\#_{tubes}$ = 4

Number of turns per tube, n = 26.92

Gas free area, GFA

$$= \frac{\pi}{4} D_{ici}^2$$

$$= \frac{\pi}{4} (1.8)^2$$

$$= 2.545 \text{ m}^2$$

Black body surface area, $BBSA$

$$= \pi \times D_{ic} \times d_o \times n \times \#_t$$

$$= \pi \times 1851 \times 50.8 \times 26.92 \times 4 \times 10^{-6}$$

$$= 31.8 \text{ m}^2$$

$$NCV(1 - C_{loss}) = \frac{20.53 \times \varepsilon \times BBSA}{m_f} \left\{ \left(\frac{T_e + 273}{100} \right)^4 - \left(\frac{T_w + 273}{100} \right)^4 \right\} + m_g c (T_e - T_{am})$$

Where:

Carbon loss, C_{loss} = 0.062 kg/kg fuel

Emissivity factor, ε = 0.81 for bituminous coal

Mass of fuel burnt/ kg gas, m_g = 12.4 kg/kg of fuel

Steam temperature at inlet, T_{sat} = 264.9 ^{o}C

Ambient air temperature, T_{am} = 25 ^{o}C

Wall temperature, T_w

$$= T_{sat} + 20$$

$$= 264.9 + 20$$

$$= 284.9 \text{ }^o\text{C}$$

Nett heat into furnace, Q_{in}

$$= NCV(1 - C_{loss})$$

$$= 23670 (1 - 0.062)$$

$$= 22197 \text{ kJ/kg}$$

Furnace exit temperature, T_e = 967.0 ^{o}C (calculated)

Mean spec. heat capacity, c = 1.151 kJ/kg^{o}C

Heat transfer by radiation, Q_{rad}

$$= \frac{20.53 \times \varepsilon \times BBSA}{m_f}\left\{\left(\frac{T_e + 273.15}{100}\right)^4 - \left(\frac{T_w + 273.15}{100}\right)^4\right\}$$

$$= \frac{20.53 \times 0.81 \times 31.8}{1378.5}\left\{\left(\frac{967 + 273.15}{100}\right)^4 - \left(\frac{284.9 + 273.15}{100}\right)^4\right\}$$

= 8701 kJ/kg

Heat absorbed by furnace $= \frac{Q_{rad} \times m_f}{3600}$

$= \frac{8701 \times 1378.5}{3600}$

= 3331.8 kW

Heat for convection passes, Q_{conv} $= m_g\ c\ (T_e - T_a)$

$= 12.42 \times 1.151 \times (967 - 25)$

= 13496 kJ/kg

$\sum_{RHS}$ (Heat for radiation & convection) = 8701+13496

= 22197 kJ/kg

C.3.2 Heat Transfer by Convection:

Log mean temperature difference, *LMTD*

$$= (T_{in} - T_w) - (T_{out} - T_w) / \ln\left\{\frac{(T_{in} - T_w)}{(T_{out} - T_w)}\right\}$$

$$= (967 - 284.9) - (949.6 - 284.9) / \ln\left\{\frac{(967 - 284.9)}{(949.6 - 284..9)}\right\}$$

= 673.3 ^oC

Furnace exit temperature, T_{in} = 967.0 ^oC (equals T_e above)

Furnace exit temperature, T_{out} = 949.6 ^oC (guessed)

Mean gas temperature, T_m = 958.3 ^oC

Gas specific heat, c_{in} = 1.151 kJ/kg^oC

Gas specific heat, c_{out} = 1.148 kJ/kg^oC

Gas specific heat, c_m = 1.264 kJ/kg^oC

Gas dynamic viscosity, μ_m = 4.784×10^{-5} kg/m.s

Thermal conductivity, k_m = 0.092 W/m^oC

Gas mass flux, G

$$= \frac{m_g}{GFA \times 3600}$$
$$= \frac{17118}{2.545 \times 3600}$$
$$= 1.869 \text{ kg/m}^2\text{.s}$$

Reynolds number, Re

$$= \frac{G \times D_{ici} \times 10^{-3}}{\mu_m}$$
$$= \frac{1.869 \times 1800 \times 10^{-3}}{4.784 \times 10^{-5}}$$
$$= 70301$$

Prandtl number, Pr

$$= \frac{c_m \times \mu_m \times 1000}{k_m}$$
$$= \frac{1.264 \times 4.784 \times 10^{-5} \times 1000}{0.092}$$
$$= 0.661$$

Nusselt number, Nu

$$= 0.023 \times Re^{0.785} \times Pr^{0.45}$$
$$= 0.023 \times 70301^{0.785} \times 0.661^{0.45}$$
$$= 126.78$$

Heat transfer coefficient (gas side), h_g

$$= f_g \left(Nu \times k\right) / D_{ici}$$
$$= 0.79 \times \left(126.78 \times 0.092\right) / 1.8$$
$$= 4.891 \text{ W/m}^2\text{ K}$$

Where, gas side fouling factor, f_g $= 0.79$

Heat transfer coefficient (water side), h_w $= 11500 \text{ W/m}^2\text{ K}$

Heat transfer coefficient (overall), U

$$= 1 / \left(h_g^{-1} + h_w^{-1}\right)$$
$$= 1 / \left(4.891^{-1} + 11500^{-1}\right)$$
$$= 4.889 \text{ W/m}^2\text{.K}$$

Heat released by gas, Q_g

$$= \frac{m_g \left(c_{in} T_{in} - c_{out} T_{out}\right)}{3600}$$
$$= \frac{17118 \times \left(1.151 \times 967 - 1.148 \times 949.6\right)}{3600}$$
$$= 104.68 \text{ kW}$$

Heat transferred to water, Q_w = $(U \times LMTD \times A)/1000$
= $(4.889 \times 673.3 \times 31.8)/1000$
= 104.68 kW

Total heat absorbed by furnace = $Q_{rad} + Q_{conv}$
= $3331.8 + 104.68$
= 3436.44 kW

Final T_e = 949.6 °C
(if RHS ≠ LHS assume different T_e and recalculate)

C.4. 2nd Pass Tube Calculation – Superheater Section

C.4.1 Inner Coil – Shell side Heat Transfer

Site altitude = 1800 masl
Altitude factor = 1.244
Barometric pressure, P_{atm} = 101.325/1.2431
= 81.5 Pa (a)

Boiler details
Mass of gas, m_g = 17118 kg/hr
Inlet gas temperature, T_{in} = 949.6 °C

Geometric Data
Coil length, L_{ic} = 1000 mm
Mean diameter (inner coil), D_{ic} = 1851 mm
Mean diameter (outer coil), D_{oc} = 2052 mm
Coil annular gap = 50 mm
Coil pitch, p = 203.2 mm

Tube diameter (outside), d_o = 50.8 mm
Tube diameter (inside), d_i = 42.68 mm
Tube starts per coil, $\#_{starts}$ = 4
Tube circumferential length, L_{tube} = $(\pi \times d_o)/2$
= $(\pi \times 50.8)/2$
= 79.8 mm

Crosswise pitch, S_T

$= d_o + \text{annular gap}$
$= 50.8 + 50$
$= 100.8$ mm

Longitudinal pitch, S_L

$= 50.8$ mm

Dimensionless crosswise pitch, a

$= S_T / d_o$
$= 1.984$

Dimensionless longitudinal pitch, b

$= S_L / d_o$
$= 1$

Area correction factor

$$= 1 - \frac{\pi}{4a}$$
$$= 1 - \frac{\pi}{4 \times 1.984}$$
$= 0.604$

Number of turns per tube, n

$$= \left(\frac{L_{ic}}{d_o} - 1 \right) \Big/ \#_{tubes}$$
$$= \left(\frac{1000}{50.8} - 1 \right) \Big/ 4$$
$= 4.67$

Coil heat transfer area, A

$= \pi \times d_o \times L_{coil} \times \#_{tubes}$
$= \pi \times 50.8 \times 27.16 \times 4 \times 10^{-3}$
$= 17.34$ m^2

Coil gas free area, GFA

$$= \frac{\pi}{4}\left(D_{oc}^2 - D_{ic}^2\right)$$
$$= \frac{\pi}{4}\left(2052^2 - 1851^2\right) \times 10^{-3}$$
$= 0.604$ m^2

Heat from gas

Gas inlet temperature (guessed), T_{in} $= 949.6$ ºC

Mean specific heat @ inlet, c_{in} $= 1.148$ kJ/kg

Final gas temperature, T_{out} $= 773.0$ ºC

Specific Heat @ Outlet, c_{out} $=1.125$ kJ/kg

Gas Temperature

Heat released by gas, Q_g

$$= \frac{m_g \times (c_{in}T_{in} - c_{out}T_{out})}{3600}$$
$$= \frac{17118 \times (1.148 \times 949.6 - 1.125 \times 773.0)}{3600}$$
$$= 1049 \text{ kW}$$

Heat transferred to steam

Saturated steam temperature, T_{sat} = 258.7 °C

Wall temperature, T_w

$$= T_{sat} + 50$$
$$= 258.7 + 50$$
$$= 308.7 \text{ °C}$$

Mean gas temperature, T_m

$$= (T_{in} + T_{out})/2$$
$$= (949.6 + 773.0)/2$$
$$= 861.3$$

Log mean temperature difference, *LMTD*

$$= (T_{in} - T_w) - (T_{out} - T_w) \Big/ \ln\left[\frac{(T_{in} - T_w)}{(T_{out} - T_w)}\right]$$
$$= (949.6 - 308.7) - (773.0 - 308.7) \Big/ \ln\left[\frac{(949.6 - 308.7)}{(773.0 - 308.7)}\right]$$
$$= 547.8 \text{ °C}$$

Gas mass flux, G

$$= \frac{m_g}{3600 \times GFA}$$
$$= \frac{17118}{3600 \times 0.618}$$
$$= 7.69 \text{ kg/m}^2\text{.s}$$

Gas Constant, R_g = 283.1

Gas density @ T_m, ρ_m

$$= \frac{P_{atm}}{R_g (T_m + 273.15)}$$
$$= \frac{81.5}{283.1 \times (861.3 + 273.15)}$$
$$= 0.254 \text{ kg/m}^3$$

Gas velocity @ inlet, w_a

$= G/\rho_m$
$= 7.69/0.254$
$= 30.33$ m/s

True specific heat @ T_m, c_m

$= 1.243$ kJ/kg

Kinematic viscosity @ T_m, ν_m

$= 1.786\times10^{-4}$ m^2/s

Thermal conductivity @ T_m, k_m

$= 0.0860$ W/m^2.C

Reynolds number, Re

$$= \frac{w\times L_{tube}}{\psi\times\nu_m}$$
$$= \frac{30.33\times 79.8\times10^{-3}}{0.604\times1.786\times10^{-4}}$$
$= 22430$

Area correction factor, ψ

$= 1-\pi/4a$ for b ≥ 1
$= 1-\pi/4\times1.984$
$= 0.604$

Prandtl number, Pr

$$= \frac{c_m\times\nu_m\times\rho_m}{k_m}$$
$$= \frac{1.243\times1.786\times10^{-4}\times0.254}{0.0860}$$
$= 0.655$

Nusselt number (laminar), Nu_l

$= 0.644\sqrt{Re}\ \sqrt[3]{Pr}$
$= 0.644\times\sqrt{22430}\times\sqrt[3]{0.655}$
$= 83.76$

Nusselt number (turbulent), Nu_t

$$= \frac{0.037\times Re^{0.8}\ Pr}{1+2.443\times Re^{-0.1}\left(Pr^{2/3}-1\right)}$$
$$= \frac{0.037\times 22430^{0.8}0.655}{1+2.443\times 22430^{-0.1}\left(0.655^{2/3}-1\right)}$$
$= 94.03$

Nusselt number (1st tube), Nu_1

$= 0.3+\sqrt{Nu_l^2+Nu_t^2}$
$= 0.3+\sqrt{83.76^2+94.03^2}$
$= 126.23$

Tube bundle arrangement factor, f_a

$$= 1 + \frac{0.7(b/a - 0.3)}{\psi^{1.5}(b/a + 0.7)^2}$$

$$= 1 + \frac{0.7(1.984^{-1} - 0.3)}{0.604^{1.5}(1.984^{-1} + 0.7)^2}$$

$$= 1.210$$

Gas side fouling factor, f_g $= 0.79$

Gas side heat transfer coefficient, h_g

$$= f_g(Nu \times k_m)/L_{tube}$$

$$= 0.79 \times (126.23 \times 0.0860)/(79.8 \times 10^{-3})$$

$$= 111.5 \text{ W/m}^2\text{K}$$

Steam side heat transfer coefficient, h_w $= 11500 \text{ W/m}^2\text{.K}$

Overall heat transfer coefficient, U

$$= 1/(h_g^{-1} + h_w^{-1})$$

$$= 1/(111.5^{-1} + 11400^{-1})$$

$$= 110.5 \text{ W/m}^2\text{.K}$$

Heat transferred to steam, Q_s

$$= (U \times LMTD \times A)/1000$$

$$= (110.5 \times 547.8 \times 17.34)/1000$$

$$= 1049.2 \text{ kW}$$

Pressure drop across superheater:

Gas Constant, R_g $= 283.1$

Mean gas density, ρ_m $= 0.254 \text{ kg/m}^3$

Mean gas velocity, w_a $= 30.22 \text{ m/s}$

Geometric Data:

Outside diameter – Inner coil, D_{ico}

$$= D_{ici} + L_{tube}$$

$$= 1800 + 79.8$$

$$= 1879.8 \text{ mm}$$

Inside diameter – Outer coil, D_{oco}

$$= Shell\ ID - 2 \times Coil\ gap - L_t$$

$$= 2203 - (2 \times 50) - 79.8$$

$$= 2023.4 \text{ mm}$$

Equivalent hydraulic diameter, D_{hydr} $= D_{oco} - D_{ico}$
$= 2023.4 - 1879.8$
$= 143.6$ mm

Reynolds number, Re $= \frac{w_a \times D_{hydr}}{\nu_m}$
$= \frac{30.33 \times 143.6 \times 10^{-3}}{1.786 \times 10^{-4}}$
$= 24389$

Drag coefficient, C_D $\frac{1}{\sqrt{C_D}} = -2\log\left[\frac{2.51}{Re\sqrt{C_D}} + \frac{K/D_{hydr}}{3.71}\right]$

$\frac{1}{\sqrt{0.025}} = -2log\left[\frac{2.51}{24389\sqrt{0.025}} + \frac{1/143.6 \times 10^{-3}}{3.71}\right]$

$6.36 = 6.36$

Pressure drop in annulus, P $= C_D \frac{L_{ic}}{D_{hydr}} \frac{\rho_m w_{ai}}{2}$
$= 0.025 \times \left(\frac{1000}{143.6}\right) \times \left(\frac{0.254 \times 30.33}{2}\right)$
$= 20.05$ Pa

C.4.2 Inner Coil – Tube side Heat Transfer

Process data
Boiler design rating = 10500 kg/hr (F&A 100°C)

Steam properties at Superheater outlet:
Steam pressure, P_{out} = 4500 kPa
Steam temperature, T_{out} = 380.7 °C
Steam enthalpy, H_{out} = 3157.1 kJ/kg

Steam properties at Superheater inlet:
Steam pressure, P_{in} = 4516 kPa
Steam temperature, T_{in} = 259.0 °C
Steam enthalpy, H_{in} = 2797.3 kJ/kg

Steam properties at Mean temperature:

Steam temperature, T_m $= (T_{out} + T_{in})/2$
$= (380.7 + 259.0)/2$
$= 319.85\ ^oC$

Steam pressure, P_m $= (P_{out} + P_{in})/2$
$= (4500 + 4516)/2$
$= 4507.9$ kPa

Steam density, ρ_m $= 18.83$ kg/m^3

Specific heat capacity of steam, c_m $= 2.796$ kJ/kg ^{o}C

Thermal conductivity of steam, k_m $= 0.053$ W/m ^{o}C

Dynamic viscosity, μ_m $= 0.021$ mPa.s

Prandtl number, Pr_m $= \dfrac{c_m \times \mu_m}{k_m}$
$= \dfrac{2.796 \times 0.021}{0.053}$
$= 1.086$

Steam properties at tube wall temperature:

Steam pressure, P_w $= 4507.9$ kPa (@ mean pressure)

Steam temperature, T_w $= T_m + 50$
$= 319.85 + 50$
$= 369.85\ ^oC$

Steam density, ρ_w $= 16.75$ kg/m^3

Specific heat capacity of steam, c_w $= 2.505$ kJ/kg ^{o}C

Thermal conductivity of steam, k_w $= 0.057$ W/m ^{o}C

Dynamic viscosity, μ_w $= 0.023$ mPa.s

Prandtl number, Pr_w $= \dfrac{c_w \times \mu_w}{k_w}$
$= \dfrac{2.505 \times 0.023}{0.057}$
$= 1.015$

Geometric data

Length of coil, L_{ic} $= 1000$ mm

Tube outside diameter, d_o $= 50.8$ mm

Tube inside diameter, d_i $= 42.68$ mm

Number of tubes per coil, $\#_{tubes}$ $= 4$

Coil pitch, p

$= d_o \times \#_{tubes}$
$= 50.8 \times 4$
$= 203.2$ mm

Number of turns per tube, n

$= \left[\left(L_{ic}/d_o\right)-1\right]/\#_{tubes}$
$= \left[\left(1000/50.8\right)-1\right]/4$
$= 4.67$

Average coil diameter, D_m

$= L_{coil} \times 10^{-3}/\left(\pi \times n\right)$
$= 27.16/\left(\pi \times 4.67\right)$
$= 1850.9$ mm

Projected winding diameter, D_w

$= \sqrt{D_m^2 - \left(p/\pi\right)^2}$
$= \sqrt{1850.9^2 - \left(203.2/\pi\right)^2}$
$= 1849.7$ mm

Average diameter of curvature, D_{ave}

$= D_w + \left[1 + \left(p/\pi D_w\right)^2\right]$
$= 1849.7 + \left[1 + \left(203.2\ /\pi \times 1849.7\ \right)^2\right]$
$= 1852.0$ mm

Steam flowrate per tube, V

$= \dfrac{\dot{m}}{\rho_m \times \#_{tubes} \times 3600}$
$= \dfrac{10500}{18.83 \times 4 \times 3600}$
$= 0.038$ m^3/s

Steam velocity inside tubes, u

$= \dfrac{4V}{\pi\ d_i^2}$
$= \dfrac{4 \times 0.038}{\pi\left(42.68 \times 10^{-3}\right)^2}$
$= 27.06$ m/s

Reynolds number, Re

$= \dfrac{u \times d_i \times \rho_m}{\mu_m}$
$= \dfrac{27.06 \times 42.68 \times 10^{-3} \times 18.83}{0.023 \times 10^{-3}}$
$= 1047864$

Critical Reynolds number, Re_{cr} $= 2300\left(1+8.6\left(d_i/D\right)^{0.45}\right)$

$= 2300\left(1+8.6\left(42.68/1852.0\right)^{0.45}\right)$

$= 5926$

Nusselt number (laminar), Nu_l for $Re \le Re_{cr}$

$= 3.66+0.08\left[1+0.8\left(d_i/D\right)^{09}\right] Re^m\, Pr^{1/3}\left(Pr/Pr_w\right)^{0.14}$

$= 3.66+0.08\left[1+0.8\left(42.68/1852.0\right)^{09}\right] 1047864^m\, 1.086^{1/3}\left(1.086/1.015\right)^{0.14}$

$= 608.84$

Where m $= 0.5+0.2903\left(d/D\right)^{0.194}$

$= 0.5+0.2903\left(42.68/1852.0\right)^{0.194}$

$= 0.6397$

Nusselt number (turbulent), Nu_t for $Re > 2.2\times10^4$

$$= \frac{\left(\xi/8\right)Re\,Pr}{1+12.7\sqrt{\xi/8}\left(Pr^{2/3}-1\right)}\left(\frac{Pr}{Pr_w}\right)^{0.14}$$

$$= \frac{\left(\xi/8\right)\times1047864\times1.086}{1+12.7\sqrt{\xi/8}\left(1.086^{2/3}-1\right)}\left(\frac{1.086}{1.015}\right)^{0.14}$$

$= 2013.06$

Where ξ $$= \left[\frac{0.3164}{Re^{0.25}}+0.03\left(\frac{d_i}{D}\right)^{0.5}\right]$$

$$= \left[\frac{0.3164}{1047864^{0.25}}+0.03\left(\frac{42.68}{1852.0}\right)^{0.5}\right]$$

$= 0.0144$

Nusselt number (laminar), Nu_l for $Re = Re_{cr}$

$= 3.66+0.08\left[1+0.8\left(d_i/D\right)^{09}\right] Re^m\, Pr^{1/3}\left(Pr/Pr_w\right)^{0.14}$

$= 3.66+0.08\left[1+0.8\left(42.68/1852.0\right)^{09}\right] 5926^m\, 1.086^{1/3}\left(1.086/1.015\right)^{0.14}$

$= 25.75$

Nusselt number (turbulent), Nu_t for $Re = 2.2\times10^4$

$$= \frac{\left(\xi/8\right)Re\,Pr}{1+12.7\sqrt{\xi/8}\left(Pr^{2/3}-1\right)}\left(\frac{Pr}{Pr_w}\right)^{0.14}$$

$$= \frac{\left(\xi/8\right)\times22000\times1.086}{1+12.7\sqrt{\xi/8}\left(1.086^{2/3}-1\right)}\left(\frac{1.086}{1.015}\right)^{0.14} = 88.16$$

Where ξ $= \left[\frac{0.3164}{Re^{0.25}} + 0.03\left(\frac{d_i}{D}\right)^{0.5}\right]$

$= \left[\frac{0.3164}{22000^{0.25}} + 0.03\left(\frac{42.68}{1852.0}\right)^{0.5}\right]$

$= 0.0305$

Nusselt number for transition zone, $Re_{cr} < Re < 2.2\times10^4$, Nu_{trans}

$= \gamma\, Nu_l\,(Re_{cr}) + (1-\gamma)\, Nu_t\,(Re = 22000)$

$= \gamma \times 25.75 + (1-\gamma)\, 88.16$

$= 88.16$

Where γ $= \frac{2.2\times10^4 - Re}{2.2\times10^4 - Re_{cr}}$

$= \frac{2.2\times10^4 - 1047864}{2.2\times10^4 - 5926}$

$= -63.82$

Since $Re > Re_{cr}$, Nusselt for turbulent is used for calculating the heat transfer coefficient,

Waterside heat transfer coefficient, h_w $= (Nu \times k_m)/d_i$

$= (2013.06\times0.053)/(42.68\times10^{-3})$

$= 2520$ W/m^{2}K

(note: h_w equal to 11500 W/m^{2}K used)

Pressure drop inside superheater coil:

Critical Reynolds number, Re_{cr} $= 5926$

For turbulent flow, where $1 < Re\sqrt{d_i/D} > Re_{cr}\sqrt{d_i/D}$ we can calculate the friction factor, ξ_w as follows:

ξ_w $= \frac{0.3164}{Re^{0.25}}\left(1 + 0.095\left(\frac{d_i}{D}\right)^{0.5} Re^{0.25}\right)$

$= \frac{0.3164}{1047864^{0.25}}\left(1 + 0.095\left(\frac{42.68}{1852.0}\right)^{0.5} 1047864^{0.25}\right)$

$= 0.0145$

Coil pressure drop, ΔP

$$= \xi_w \frac{l}{\#_{tubes} d_i} \frac{\rho w^2}{2}$$

$$= 0.0145 \left(\frac{27.16 \times 10^3}{4 \times 42.68} \right) \left(\frac{18.83 \times 27.06^2}{2} \right)$$

$$= 15.9 \text{ kPa}$$

C.5. 2nd Pass Tube Calculation – Evaporator Section

C.5.1 Inner Coil – Shell side Heat Transfer

Site altitude = 1800 masl
Altitude factor = 1.244
Barometric pressure, P_{atm} = 101.325/1.2431
= 81.5 Pa (a)

Boiler details
Mass of gas, m_g = 17118 kg/hr
Inlet gas temperature, T_{in} = 773.0 °C

Geometric Data
Coil length, L_{ic} = 5520 mm
Mean diameter (inner coil), D_{ic} = 1851 mm
Mean diameter (outer coil), D_{oc} = 2052 mm
Coil annular gap = 50 mm
Coil pitch, p = 203.2 mm

Tube diameter (outside), d_o = 50.8 mm
Tube diameter (inside), d_i = 42.68 mm
Tube starts per coil, $\#_{starts}$ = 4
Tube circumferential length, L_{tube} $= (\pi d_o)/2$
$= (\pi \times 50.8)/2$
= 79.8 mm

Crosswise pitch, S_T $= d_o + annular\ gap$
$= 50.8 + 50$
= 100.8 mm

Longitudinal pitch, S_L = 50.8 mm

Dimensionless crosswise pitch, a $= S_T / d_o$
$= 1.984$

Dimensionless longitudinal pitch, b $= S_L / d_o$
$= 1$

Area correction factor, ψ $= 1 - \frac{\pi}{4a}$
$= 1 - \frac{\pi}{4 \times 1.984}$
$= 0.604$

Number of turns per tube, n $= \left(\frac{L_{ic}}{d_o} - 1 \right) \Big/ \#_{tubes}$
$= \left(\frac{5520}{50.8} - 1 \right) \Big/ 4$
$= 26.92$

Coil heat transfer area, A $= \pi \times d_o \times L_{coil} \times \#_{tubes}$
$= \pi \times 50.8 \times 27.16 \times 4 \times 10^{-3}$
$= 17.34 \text{m}^2$

Coil gas free area, GFA $= \frac{\pi}{4} \left(D_{oc}^2 - D_{ic}^2 \right)$
$= \frac{\pi}{4} \left(2052^2 - 1851^2 \right) \times 10^{-3}$
$= 0.604 \text{ m}^2$

Heat from gas
Gas inlet temperature (guessed), T_{in} $= 773.0 \text{ }^{o}\text{C}$

Mean specific heat @ inlet, c_{in} $= 1.125$ kJ/kg

Final gas temperature, T_{out} $= 363.0 \text{ }^{o}\text{C}$

Specific Heat @ Outlet, c_{out} $=1.070$ kJ/kg
Gas Temperature

Heat released by gas, Q_g

$$= \frac{m_g\left(c_{in}T_{in} - c_{out}T_{out}\right)}{3600}$$
$$= \frac{17118\times\left(1.125\times 773.0 - 1.070\times 363.0\right)}{3600}$$
$$= 2289.5 \text{ kW}$$

Heat transferred to steam

Saturated steam temperature, T_{sat} = 264.9 °C

Wall temperature, T_w

$$= T_{sat} + 5$$
$$= 264.9 + 5$$
$$= 269.9 \text{ °C}$$

Mean gas temperature, T_m

$$= \left(T_{in} + T_{out}\right)/2$$
$$= \left(773.0 + 363.0\right)/2$$
$$= 568.0 \text{ °C}$$

Log mean temperature difference, $LMTD$

$$= \left(T_{in} - T_w\right) - \left(T_{out} - T_w\right) \Big/ \ln\left[\frac{\left(T_{in} - T_w\right)}{\left(T_{out} - T_w\right)}\right]$$
$$= \left(773.0 - 269.9\right) - \left(363.0 - 269.9\right) \Big/ \ln\left[\frac{\left(773.0 - 269.9\right)}{\left(363.0 - 269.9\right)}\right]$$
$$= 242.9 \text{ °C}$$

Gas mass flux, G

$$= \frac{m_g}{3600\times GFA}$$
$$= \frac{17118}{3600\times 0.618}$$
$$= 7.69 \text{ kg/m}^2\text{.s}$$

Gas Constant, R_g = 283.1

Gas density @ T_m, ρ_m

$$= \frac{P_{atm}}{R_g\left(T_m + 273.15\right)}$$
$$= \frac{81.5}{283.1\times\left(568.0 + 273.15\right)}$$
$$= 0.342 \text{ kg/m}^3$$

Gas velocity @ inlet, w_a

$= G/\rho_m$
$= 7.69/0.342$
$= 22.49$ m/s

True specific heat @ T_m, c_m

$= 1.175$ kJ/kg

Kinematic viscosity @ T_m, ν_m

$= 1.084\times10^{-4}$ m^2/s

Thermal conductivity @ T_m, k_m

$= 0.0681$ W/m^2.C

Reynolds number, Re

$$= \frac{w_a \times L_{tube}}{\psi \times \nu_m}$$
$$= \frac{22.49\times 79.8\times10^{-3}}{0.604\times1.084\times10^{-4}}$$
$= 27403$

Area correction factor, ψ

$= 1-\pi/4a$ for b ≥ 1
$= 1-\pi/4\times1.984$
$= 0.604$

Prandtl number, Pr

$$= \frac{c_m \times \nu_m \times \rho_m}{k_m}$$
$$= \frac{1.175\times1.084\times10^{-4}\times0.342}{0.0681}$$
$= 0.640$

Nusselt number (laminar), Nu_l

$= 0.644\sqrt{Re}\ \sqrt[3]{Pr}$
$= 0.644\times\sqrt{27403}\times\sqrt[3]{0.640}$
$= 91.85$

Nusselt number (turbulent), Nu_t

$$= \frac{0.037\times Re^{0.8}\ Pr}{1+2.443\times Re^{-0.1}\left(Pr^{2/3}-1\right)}$$
$$= \frac{0.037\times 27403^{0.8}0.640}{1+2.443\times 27403^{-0.1}\left(0.640^{2/3}-1\right)}$$
$= 108.62$

Nusselt number (1st tube), Nu_1

$= 0.3+\sqrt{Nu_l^2+Nu_t^2}$
$= 0.3+\sqrt{91.85^{\,2}+108.62^{\,2}}$
$= 142.55$

Tube bundle arrangement factor, f_a

$$= 1 + \frac{0.7(b/a - 0.3)}{\psi^{1.5}(b/a + 0.7)^2}$$

$$= 1 + \frac{0.7(1.984^{-1} - 0.3)}{0.604^{1.5}(1.984^{-1} + 0.7)^2}$$

$$= 1.210$$

Gas side fouling factor, f_g $= 0.79$

Gas side heat transfer coefficient, h_g

$$= f_g(Nu \times k_m)/L_{tube}$$

$$= 0.79 \times (142.55 \times 0.0681)/(79.8 \times 10^{-3})$$

$$= 96.1 \text{ W/m}^2\text{K}$$

Waterside heat transfer coefficient, h_w $= 5009 \text{ W/m}^2\text{.K}$

Overall heat transfer coefficient, U

$$= 1/(h_g^{-1} + h_w^{-1})$$

$$= 1/(96.1^{-1} + 5009^{-1})$$

$$= 94.3 \text{ W/m}^2\text{.K}$$

Heat transferred to water, Q_s

$$= (U \times LMTD \times A)/1000$$

$$= (94.3 \times 242.9 \times 99.91)/1000$$

$$= 2289.5 \text{ kW}$$

Pressure drop across superheater:

Gas Constant, R_g $= 283.1$

Mean gas density, ρ_m $= 0.342 \text{ kg/m}^3$

Mean gas velocity, w_a $= 22.49 \text{ m/s}$

Geometric Data:

Outside diameter – Inner coil, D_{ico}

$$= D_{ici} + L_{tube}$$

$$= 1800 + 79.8$$

$$= 1879.8 \text{ mm}$$

Inside diameter – Outer coil, D_{oci}

$$= Shell\ ID - 2 \times Coil\ gap - L_t$$

$$= 2203 - (2 \times 50) - 79.8$$

$$= 2023.4 \text{ mm}$$

Equivalent hydraulic diameter, D_{hydr}

$$= D_{oci} - D_{ico}$$

$$= 2023.4 - 1879.8$$

$= 143.6$ mm

Reynolds number, Re

$$= \frac{w_a \times D_{hydr}}{\nu_m}$$

$$= \frac{22.49 \times 143.6 \times 10^{-3}}{1.084 \times 10^{-4}}$$

$= 29796$

Drag coefficient, C_D

$$\frac{1}{\sqrt{C_D}} = -2\log\left[\frac{2.51}{Re\sqrt{C_D}} + \frac{K/D_{hydr}}{3.71}\right]$$

$$\frac{1}{\sqrt{0.024}} = -2\log\left[\frac{2.51}{29796\sqrt{0.024}} + \frac{1/143.6 \times 10^{-3}}{3.71}\right]$$

$6.52 = 6.52$

Pressure drop in annulus, P

$$= C_D \frac{L_{ic}}{D_{hydr}} \frac{\rho_m w_a}{2}$$

$$= 0.024\left(\frac{5520}{143.6}\right)\left(\frac{0.342 \times 22.49}{2}\right)$$

$= 78.27$ Pa

C.5.2 Inner Coil – Waterside Heat Transfer

Process data

Boiler design rating $= 10500$ kg/hr (F&A 100°C)

Steam properties at Evaporator inlet:

Steam pressure, P_{in} $= 4999$ kPa

Steam temperature, T_{in} $= 264.9$ °C

Since the evaporation process is isothermal and no accuracy is lossed in assuming constant pressure conditions for determining the steam properties, we get;

Steam density, ρ_m $= 25.8$ kg/m^3

Specific heat capacity of steam, c_m $= 4.472$ kJ/kg °C

Thermal conductivity of steam, k_m $= 0.056$ W/m °C

Dynamic viscosity, μ_m $= 0.018$ mPa.s

Prandtl number, Pr_m

$$= \frac{c_m \times \mu_m}{k_m}$$

$$= \frac{4.472 \times 0.018}{0.056}$$

$= 1.456$

Steam properties at tube wall temperature:

Steam pressure, P_w = 5416 kPa (saturation pressure at T_w)

Steam temperature, T_w $= T_m + 5$
$= 264.9 + 5$
$= 269.9\ ^oC$

Steam density, ρ_w $= 28.0\ kg/m^3$

Specific heat capacity of steam, c_w $= 5.118\ kJ/kg\ ^oC$

Thermal conductivity of steam, k_w $= 0.596\ W/m\ ^oC$

Dynamic viscosity, μ_w $= 0.098\ mPa.s$

Prandtl number, Pr_w $= \dfrac{c_w \times \mu_w}{k_w}$
$= \dfrac{5.118 \times 0.098}{0.596}$
$= 0.837$

Geometric data

Length of coil, L_{ic} $= 5520\ mm$

Tube outside diameter, d_o $= 50.8\ mm$

Tube inside diameter, d_i $= 42.68\ mm$

Number of tubes per coil, $\#_{tubes}$ $= 4$

Coil pitch, p $= d_o \times \#_{tubes}$
$= 50.8 \times 4$
$= 203.2\ mm$

Number of turns per tube, n $= \left[\left(L_{ic}/d_o\right) - 1\right]/\#_{tubes}$
$= \left[\left(5520/50.8\right) - 1\right]/4$
$= 26.92$

Average coil diameter, D_m $= L_{coil} \times 10^{-3}/\left(\pi \times n\right)$
$= 156.50/\left(\pi \times 26.92\right)$
$= 1850.9\ mm$

Projected winding diameter, D_w $= \sqrt{D_m^2 - \left(p/\pi\right)^2}$
$= \sqrt{1850.9^2 - \left(203.2/\pi\right)^2}$
$= 1849.7\ mm$

Average diameter of curvature, D $= D_w + \left[1 + \left(p/\pi D_w\right)^2\right]$
$= 1849.7 + \left[1 + \left(203.2\ /\pi \times\ 1849.7\ \right)^2\right]$

$= 1852.0$ mm

Steam flowrate per tube, V

$$= \frac{cr \times \dot{m}}{\rho_m \times \#_{tubes} \times 3600}$$
$$= \frac{1.4 \times 10500}{25.8 \times 4 \times 3600}$$
$= 0.158$ m^3/s

Steam velocity inside tubes, u

$$= \frac{4V}{\pi d_i^2}$$
$$= \frac{4 \times 0.158}{\pi (42.68 \times 10^{-3})^2}$$
$= 27.67$ m/s

Reynolds number, Re

$$= \frac{u \times d_i \times \rho_m}{\mu_m}$$
$$= \frac{27.67 \times 42.68 \times 10^{-3} \times 25.8}{0.018 \times 10^{-3}}$$
$= 1685134$

Critical Reynolds number, Re_{cr}

$$= 2300 \left(1 + 8.6 \left(d_i / D\right)^{0.45}\right)$$
$$= 2300 \left(1 + 8.6 \left(42.68/1852.0\right)^{0.45}\right)$$
$= 5926$

Nusselt number (laminar), Nu_l for $Re \leq Re_{cr}$

$$= 3.66 + 0.08 \left[1 + 0.8 \left(d_i/D\right)^{09}\right] Re^m \, Pr^{1/3} \left(Pr/Pr_w\right)^{0.14}$$
$$= 3.66 + 0.08 \left[1 + 0.8 \left(42.68/1852.0\right)^{09}\right] 1685134^{\,m} \, 1.456^{1/3} (1.456/0.837)^{0.14}$$
$= 971.46$

Where m $= 0.5 + 0.2903 \left(d/D\right)^{0.194}$

$$= 0.5 + 0.2903 \left(42.68/1852.0\right)^{0.194}$$
$= 0.6397$

Nusselt number (turbulent), Nu_t for $Re > 2.2 \times 10^4$

$$= \frac{(\xi/8) Re \, Pr}{1 + 12.7 \sqrt{\xi/8} \left(Pr^{2/3} - 1\right)} \left(\frac{Pr}{Pr_w}\right)^{0.14}$$
$$= \frac{(\xi/8) \times 1685134 \times 1.456}{1 + 12.7 \sqrt{\xi/8} \left(1.456^{2/3} - 1\right)} \left(\frac{1.456}{0.837}\right)^{0.14}$$
$= 3850.95$

Where ξ $= \left[\frac{0.3164}{Re^{0.25}} + 0.03\left(\frac{d_i}{D}\right)^{0.5}\right]$

$= \left[\frac{0.3164}{1685134^{0.25}} + 0.03\left(\frac{42.68}{1852.0}\right)^{0.5}\right]$

$= 0.0133$

Nusselt number (laminar), Nu_l for $Re = Re_{cr}$

$= 3.66 + 0.08\left[1 + 0.8\left(d_i/D\right)^{09}\right] Re^m\, Pr^{1/3}\left(Pr/Pr_w\right)^{0.14}$

$= 3.66 + 0.08\left[1 + 0.8\left(42.68/1852.0\right)^{09}\right] 5926^{\,m}\, 1.456^{1/3}\left(1.456/0.837\right)^{0.14}$

$= 29.72$

Nusselt number (turbulent), Nu_t for $Re = 2.2\times10^4$

$= \frac{(\xi/8)\,Re\,Pr}{1 + 12.7\sqrt{\xi/8}\left(Pr^{2/3} - 1\right)}\left(\frac{Pr}{Pr_w}\right)^{0.14}$

$= \frac{(\xi/8)\times 22000\times 1.456}{1 + 12.7\sqrt{\xi/8}\left(1.456^{2/3} - 1\right)}\left(\frac{1.456}{0.837}\right)^{0.14}$

$= 107.98$

Where ξ $= \left[\frac{0.3164}{Re^{0.25}} + 0.03\left(\frac{d_i}{D}\right)^{0.5}\right]$

$= \left[\frac{0.3164}{22000^{0.25}} + 0.03\left(\frac{42.68}{1852.0}\right)^{0.5}\right]$

$= 0.0305$

Nusselt number for transition zone, $Re_{cr} < Re < 2.2\times10^4$, Nu_{trans}

$= \gamma\, Nu_{lam}\left(Re_{cr}\right) + \left(1-\gamma\right) Nu_t\left(Re = 22000\right)$

$= \gamma \times 29.72 + \left(1-\gamma\right) 107.98$

$= 107.98$

Where γ $= \frac{2.2\times10^4 - Re}{2.2\times10^4 - Re_{cr}}$

$= \frac{2.2\times10^4 - 1685134}{2.2\times10^4 - 5926}$

$= -103.47$

Since $Re > Re_{cr}$, Nusselt for turbulent is used for calculating the heat transfer coefficient,

Waterside heat transfer coefficient, h_w $= (Nu \times k_m)/d_i$

$= (3850.95 \times 0.056)/(42.68 \times 10^{-3})$

$=5009$ W/m^{2}K

(Note: h_w equal to 11500 W/m^{2}K normally used in boiler sizing calculations)

Pressure drop inside superheater coil:

Critical Reynolds number, Re_{cr} = 5926

For turbulent flow, where $1 < Re\sqrt{d_i/D} > Re_{cr}\sqrt{d_i/D}$ we can calculate the friction factor, ξ_w as follows:

$$\xi_w = \frac{0.3164}{Re^{0.25}}\left(1+0.095\left(\frac{d_i}{D}\right)^{0.5} Re^{0.25}\right)$$

$$= \frac{0.3164}{1685134^{0.25}}\left(1+0.095\left(\frac{42.68}{1852.0}\right)^{0.5} 1685134^{0.25}\right)$$

$$= 0.0133$$

Coil pressure drop, ΔP $= \xi_w \frac{l}{\#_{tubes} d_i}\frac{\rho w^2}{2}$

$$= 0.0133\left(\frac{156.5\times10^3}{4\times42.68}\right)\left(\frac{25.8\times27.67^2}{2}\right)$$

$= 483.1$ kPa

Check:

Therefore outlet pressure equals, P_{out} $= P_{in} - \Delta P$

$= 4999 - 483.1$

$= 4515.9$ kPa

APPENDIX D: SAMPLE CALCULATION – BOILER CIRCULATION RATE

D.1. Evaporator Inlet Conditions

Boiler Design Evaporation = 10500 kg/hr (F&A 100°C)
Operating pressure = 4500 kPa
Operating temperature = 257.4 °C

Feedwater Conditions at Inlet
Inlet pressure, P_{in} = 5027.9 kPa
Inlet temperature, T_{in} = 105 °C kPa
Enthalpy of liquid at inlet, H_{in} = 443.9 kJ/kg
Enthalpy of saturated liquid, H_{sat} = 1161.3 kJ/kg
Enthalpy of evaporation, H_{fg} = 1632.0 kJ/kg
Density of saturated liquid, ρ = 775.2 kg/m^3

D.2. Circulation Calculations

Water mass velocity, m

$$= \frac{4 \times m_{steam} \times C_f}{3600 \times n \times \pi \times d_i^2}$$

$$= \frac{4 \times 10500 \times 1.4}{3600 \times 4 \times \pi \left(42.68 \times 10^{-3}\right)^2}$$

= 713.5 kg/m^2.s

Inner coil geometry
Coil mean diameter, D_{ic} = 1851 mm
Tube outside diameter, d_o = 50.8 mm
Tube inside diameter, d_i = 42.68 mm
Tube wall thickness, t = 4.06 mm
Number of tubes per coil, $\#_{tubes}$ = 4
Calculated pipe length per turn, L_{ic} = 156.5 m

Calculation factors
Enthalpy coefficient, K_h

$$= 1 + 3.8\left(1 - H_{in}/H_{sat}\right)$$

$$= 1 + 3.8\left(1 - 443.9/1161.3\right)$$

= 3.347

Pressure coefficient, K_p

$$= 0.114 - 0.41 \ln(1 - P_r)$$
$$= 0.114 - 0.41 \ln(1 - 0.232)$$
$$= 0.125$$

Wall thickness coefficient, K_δ

$$= \left(\frac{2\delta}{d_i}\right)^{0.32}$$
$$= \left(\frac{2 \times 4.06}{42.68}\right)^{0.32}$$
$$= 0.588$$

Reduced reference pressure, P_r

$$= \frac{P_{in} + P_{atm}}{220.64}$$
$$= \frac{5057.6 + 81.5}{220.64}$$
$$= 0.232$$

Froude number, Fr

$$= \frac{m}{\rho\sqrt{9.81 \times d_i}}$$
$$= \frac{713.5}{775.2\sqrt{9.81 \times 42.68}}$$
$$= 1.423$$

Inlet vapour fraction, x_{in}

$$= \frac{H_{in} - H_{sat}}{H_{fg}}$$
$$= \frac{443.9 - 1161.3}{1632.0}$$
$$= - 0.440$$

D.3. 1st Boiling Crisis - Film Boiling (Departure from Nucleate Boiling)

Coil coefficient, K_D

$$= 1 + 0.44 \exp(-0.056 D_{ic}/d_i)$$
$$= 1 + 0.44 \, exp\,(-0.056\,(1851/42.68))$$
$$= 1.039$$

Calculation factor, L_{cr}/d_i

$$= \frac{m \times H_{fg}}{4 q_{av}}(x_{cr} - x_{in})$$
$$= \frac{713.5 \times 1632.0}{4 \times 57.3}(0.544 - (-0.440))$$
$$= 4997$$

Mass flow coefficient, K_m

$$= \frac{(L_{cr}/d_i)+4.59(L_{cr}/d_i)^{-0.2}}{(L_{cr}/d_i)+Fr^{0.44}}$$

$$= \frac{4997+4.59\times 4997^{-0.2}}{4997+1.423^{0.44}}$$

$$= 0.994$$

Critical vapour mass fraction, x_{cr}

$$= 3.88\times K_h K_p K_D K_\delta K_m + x_{in}$$

$$= 3.88\times 3.347\times 0.125\times 1.039\times 0.588\times 0.994 - 0.440$$

$$= 0.544$$

Location of 1st boiling crisis, L_{cr}

$$= d_i (L_{cr}/d_i)$$

$$= 42.68\times 4997\times 10^{-3}$$

$$= 213.3 \text{ m}$$

Coil critical heat flux (Based on coil geometry)

Calculated pipe length per turn, L_{cr} = 156.5 m

Calculation factor, L_{cr}/d_i

$$= \frac{L_{cr}}{d_i}$$

$$= \frac{156.5}{42.68\times 10^{-3}}$$

$$= 3667$$

Mass flow coefficient, K_m

$$= \frac{(L_{cr}/d_i)+4.59(L_{cr}/d_i)^{-0.2}}{(L_{cr}/d_i)+Fr^{0.44}}$$

$$= \frac{3667+4.59\times 3667^{-0.2}}{3667+1.423^{0.44}}$$

$$= 0.991$$

Critical vapour mass fraction, x_r

$$= 3.88\times K_h K_p K_D K_\delta K_m + x_{in}$$

$$= 3.88\times 3.347\times 0.125\times 1.039\times 0.588\times 0.991 - 0.440$$

$$= 0.542$$

Critical heat flux, q_{cr}

$$= \frac{m\times d_i\times H_{fg}}{4L_{cr}}(x_{cr}-x_{in})$$

$$= \frac{713.5\times 42.68\times 1632}{4\times 156.5}(0.542+0.440)$$

= 77.93 kW/m^2

D.4. 2nd Boiling Crisis - Dry Out of Heating Surfaces (Deposition Controlled Burnout)

Coil coefficient, K_D = 1.348

Calculation factor, L_{cr}/d_i = 6492

Mass flow coefficient, K_m = 0.995

Critical vapour mass fraction, x_{cr} = 0.839

Location of 2nd boiling crisis, L_{cr} = 277.1 m

Coil critical heat flux (Based on coil geometry)
Calculated pipe length per turn, L_{cr} = 156.5 m

Calculation factor, L_{cr}/d_i = 3667

Mass flow coefficient, K_m = 0.991

Critical vapour mass fraction, x_{cr} = 0.834

Critical heat flux, q_{cr} = 101.09 kW/m^2

APPENDIX E: MANUFACTURING DRAWINGS FOR THE SUPERHEATER, EVAPORATOR AND ECONOMISER SECTIONS

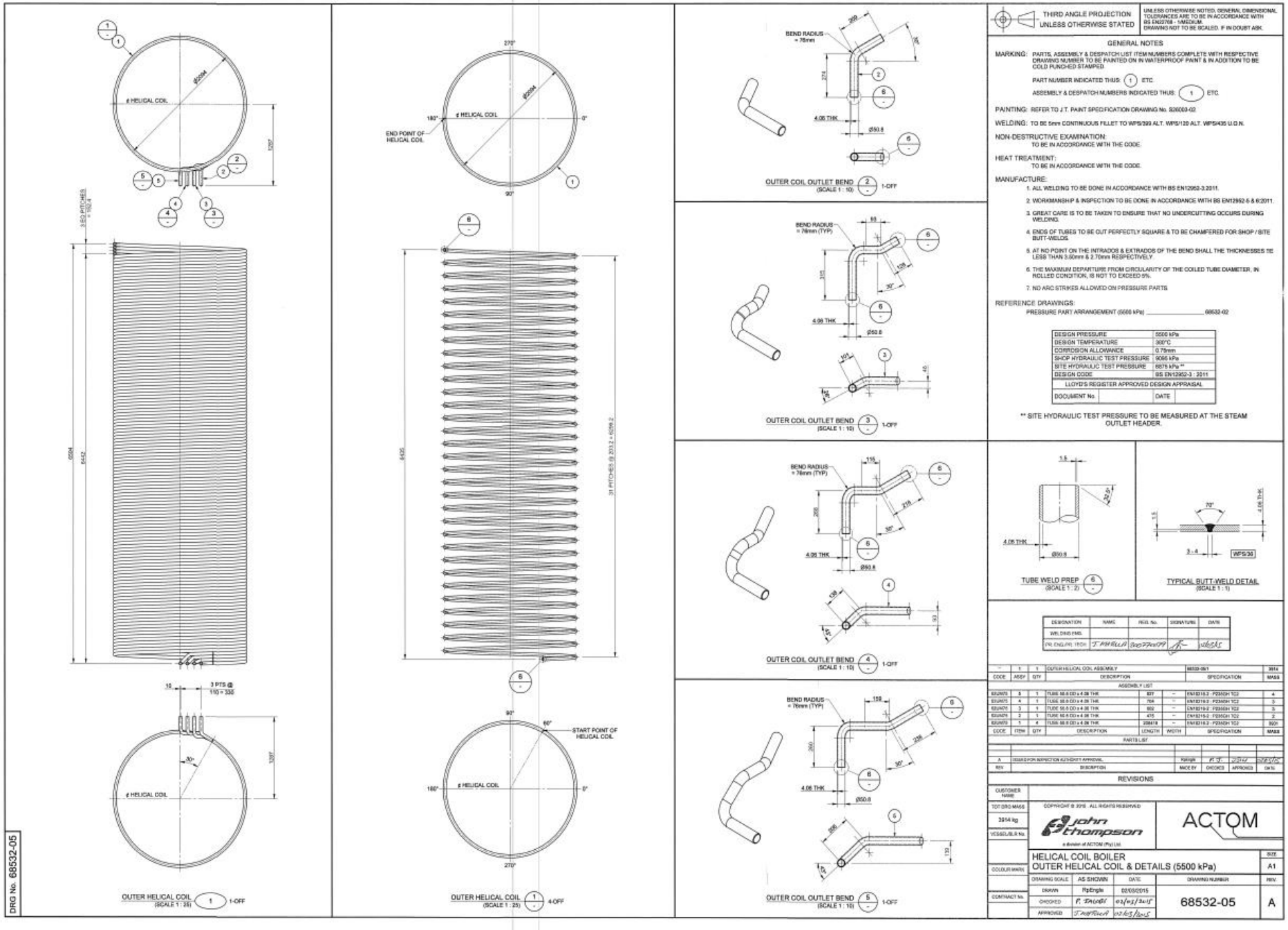

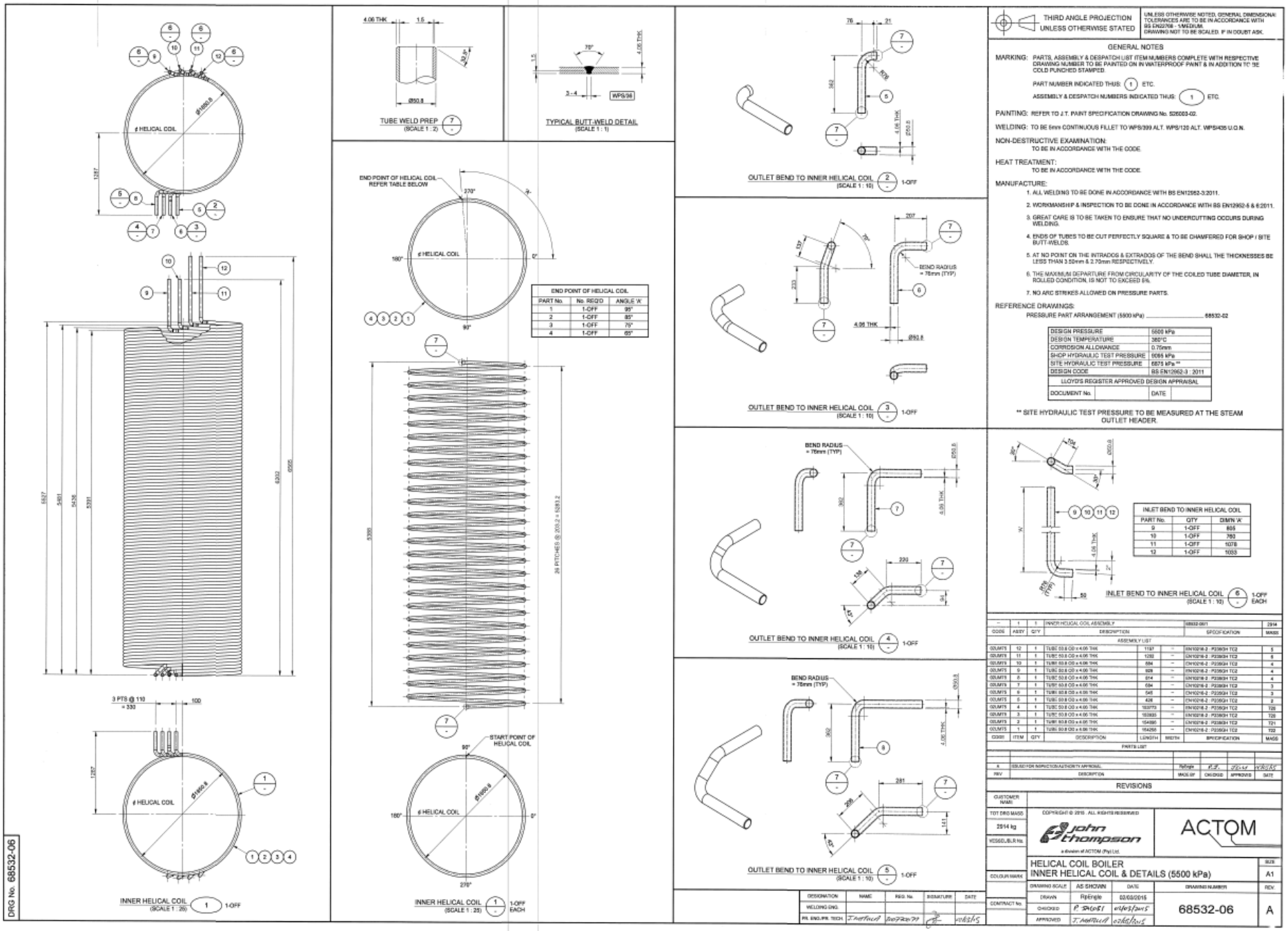

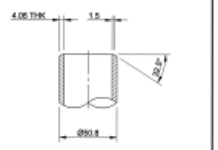

TUBE WELD PREP (7) (SCALE 1 : 2)

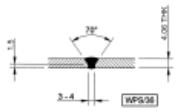

TYPICAL BUTT-WELD DETAIL (SCALE 1 : 1)

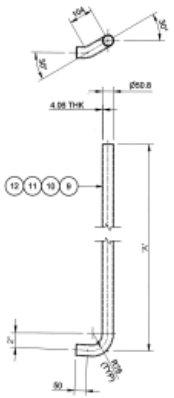

INLET BEND TO S/HEATER HELICAL COIL		
PART No.	QTY	DIM'N 'A'
9	1-OFF	1169
10	1-OFF	1123
11	1-OFF	640
12	1-OFF	595

INLET BEND TO SUPERHEATER HELICAL COIL (6) (SCALE 1 : 10) 1-OFF EACH

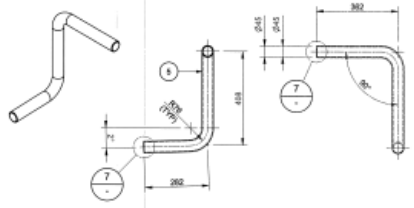

OUTLET BEND TO INNER HELICAL COIL (2) (SCALE 1 : 10) 1-OFF

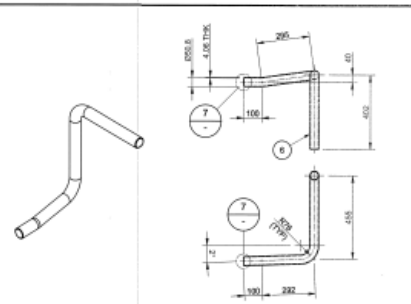

OUTLET BEND TO INNER HELICAL COIL (3) (SCALE 1 : 12.5) 1-OFF

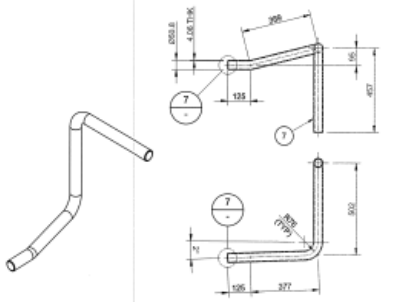

OUTLET BEND TO INNER HELICAL COIL (4) (SCALE 1 : 12.5) 1-OFF

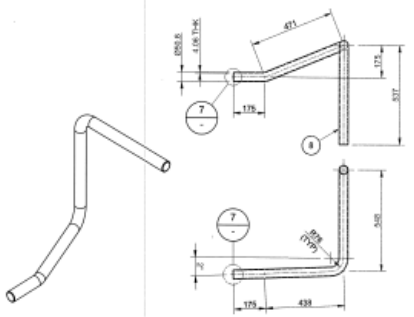

OUTLET BEND TO INNER HELICAL COIL (5) (SCALE 1 : 10) 1-OFF

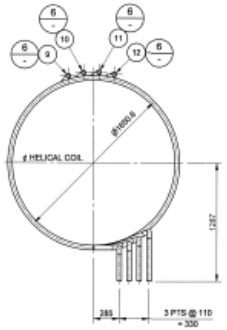

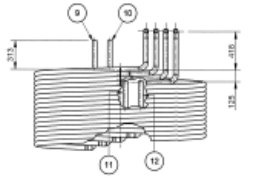

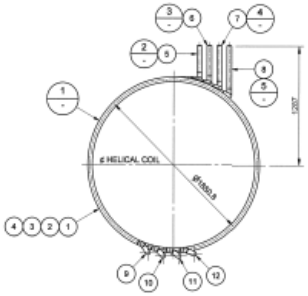

SUPERHEATER HELICAL COIL (1) (SCALE 1 : 25) 1-OFF

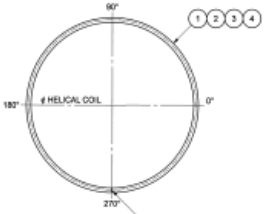

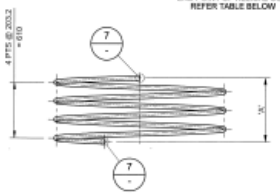

SUPERHEATER HELICAL COIL DETAILS			
PART No.	QTY	DIM'N 'A'	ANGLE 'B'
1	1-OFF	697	115°
2	1-OFF	703	105°
3	1-OFF	708	95°
4	1-OFF	714	85°

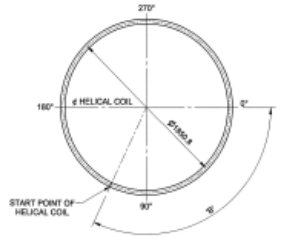

SUPERHEATER HELICAL COIL (1) (SCALE 1 : 25) 1-OFF EACH

THIRD ANGLE PROJECTION UNLESS OTHERWISE STATED

UNLESS OTHERWISE NOTED, GENERAL DIMENSIONAL TOLERANCES ARE TO BE IN ACCORDANCE WITH BS EN22768 - 1/MEDIUM. DRAWING NOT TO BE SCALED. IF IN DOUBT ASK.

GENERAL NOTES

MARKING: PARTS, ASSEMBLY & DESPATCH LIST ITEM NUMBERS COMPLETE WITH RESPECTIVE DRAWING NUMBER TO BE PAINTED ON IN WATERPROOF PAINT & IN ADDITION TO BE COLD PUNCHED STAMPED.

PART NUMBER INDICATED THUS: (1) ETC.

ASSEMBLY & DESPATCH NUMBERS INDICATED THUS: (1) ETC.

PAINTING: REFER TO J.T. PAINT SPECIFICATION DRAWING No. S26003-02.

WELDING: TO BE 6mm CONTINUOUS FILLET TO WPS/309 ALT. WPS/120 ALT. WPS/435 U.O.N.

NON-DESTRUCTIVE EXAMINATION:
TO BE IN ACCORDANCE WITH THE CODE.

HEAT TREATMENT:
TO BE IN ACCORDANCE WITH THE CODE.

MANUFACTURE:

1. ALL WELDING TO BE DONE IN ACCORDANCE WITH BS EN12952-3:2011.
2. WORKMANSHIP & INSPECTION TO BE DONE IN ACCORDANCE WITH BS EN12952-6 & 6:2011.
3. GREAT CARE IS TO BE TAKEN TO ENSURE THAT NO UNDERCUTTING OCCURS DURING WELDING.
4. ENDS OF TUBES TO BE CUT PERFECTLY SQUARE & TO BE CHAMFERED FOR SHOP / SITE BUTT-WELDS.
5. AT NO POINT ON THE INTRADOS & EXTRADOS OF THE BEND SHALL THE THICKNESSES BE LESS THAN 3.02mm & 2.79mm RESPECTIVELY.
6. THE MAXIMUM DEPARTURE FROM CIRCULARITY OF THE COILED TUBE DIAMETER, IN ROLLED CONDITION, IS NOT TO EXCEED 5%.
7. NO ARC STRIKES ALLOWED ON PRESSURE PARTS.

REFERENCE DRAWINGS:
PRESSURE PART ARRANGEMENT (5500 kPa) 68532-02

DESIGN PRESSURE	5500 kPa
DESIGN TEMPERATURE	380°C
CORROSION ALLOWANCE	0.75mm
SHOP HYDRAULIC TEST PRESSURE	6686 kPa
SITE HYDRAULIC TEST PRESSURE	6875 kPa **
DESIGN CODE	BS EN12952-3 : 2011
LLOYD'S REGISTER APPROVED DESIGN APPRAISAL	
DOCUMENT No.	DATE

** SITE HYDRAULIC TEST PRESSURE TO BE MEASURED AT THE STEAM OUTLET HEADER.

DESIGNATION	NAME	REG. No.	SIGNATURE	DATE
WELDING ENG.				
PR. ENG./PR. TECH.	J. MATTHEW	ZA0FR2179		2015/5/5

ITEM	CODE	ASSY	QTY	DESCRIPTION	SPECIFICATION	MASS
–	–	1	1	SUPERHEATER COIL ASSEMBLY	68532-011	421
				ASSEMBLY LIST		
12	EDUN75		1	TUBE 38.0 OD x 4.06 THK	713	– EN10216-2 : P295GH TC2 3
11	EDUN75		1	TUBE 38.0 OD x 4.06 THK	768	– EN10216-2 : P295GH TC2 4
10	EDUN75		1	TUBE 38.0 OD x 4.06 THK	1242	– EN10216-2 : P295GH TC2 6
9	EDUN75		1	TUBE 38.0 OD x 4.06 THK	1267	– EN10216-2 : P295GH TC2 6
8	EDUN75		1	TUBE 38.0 OD x 4.06 THK	1855	– EN10216-2 : P295GH TC2 8
7	EDUN75		1	TUBE 38.0 OD x 4.06 THK	1410	– EN10216-2 : P295GH TC2 7
6	EDUN75		1	TUBE 38.0 OD x 4.06 THK	1169	– EN10216-2 : P295GH TC2 6
5	EDUN75		1	TUBE 38.0 OD x 4.06 THK	980	– EN10216-2 : P295GH TC2 5
4	EDUN75		1	TUBE 38.0 OD x 4.06 THK	20444	– EN10216-2 : P295GH TC2 86
3	EDUN75		1	TUBE 38.0 OD x 4.06 THK	20262	– EN10216-2 : P295GH TC2 85
2	EDUN75		1	TUBE 38.0 OD x 4.06 THK	20131	– EN10216-2 : P295GH TC2 84
1	EDUN75		1	TUBE 38.0 OD x 4.06 THK	19859	– EN10216-2 : P295GH TC2 83
ITEM	CODE	ITEM	QTY	DESCRIPTION	LENGTH WIDTH	SPECIFICATION MASS
				PARTS LIST		

REV	DESCRIPTION	MADE BY	CHECKED	APPROVED	DATE
A	ISSUED FOR INSPECTION & FABRICATION APPROVAL	RpEngle	P. F.	[illegible]	2015/05/05

REVISIONS

CUSTOMER NAME

TOT DRG MASS 421 kg

VESSEL/B.R No.

COLOUR MARK

CONTRACT No.

john thompson
a division of ACTOM (Pty) Ltd.

ACTOM

HELICAL COIL BOILER
SUPERHEATER HELICAL COIL & DETAILS (5500 kPa)

SIZE: A1

DRAWING SCALE	AS SHOWN	DATE	DRAWING NUMBER	REV.
DRAWN	RpEngle	02/03/2015	68532-07	A
CHECKED	P. FACHER	2015/5/5		
APPROVED	J. MATTHEW	2015/5/5		

DRG No. 68532-07

APPENDIX F: SELECTION OF NEAR-WALL TREATMENT METHOD

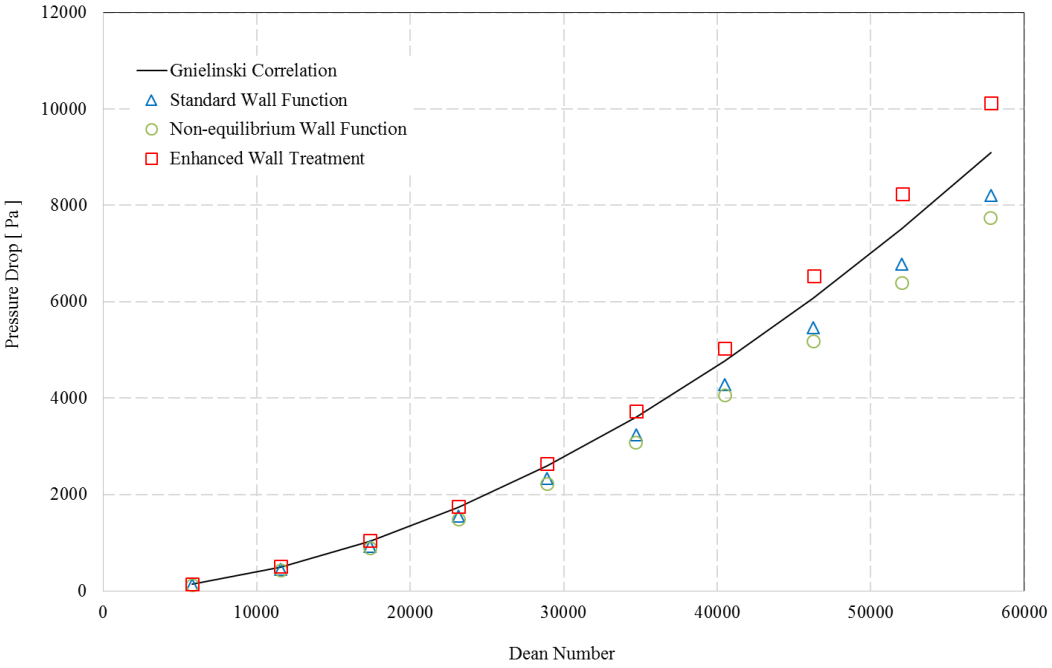

Figure F.1: Pressure drop comparison for near-wall treatment methods considered.

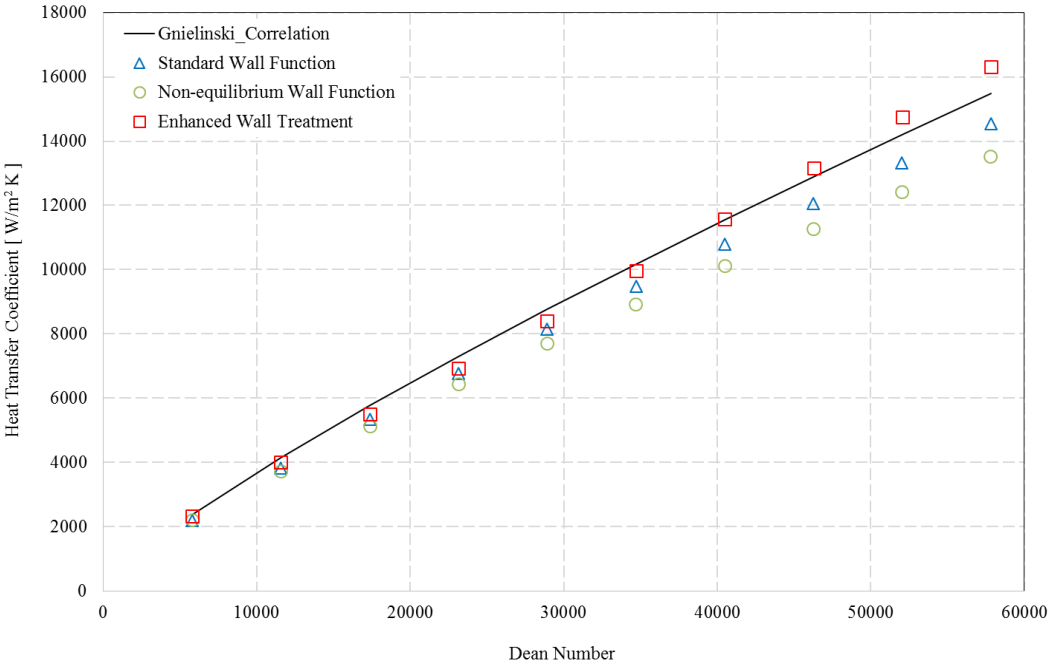

Figure F.2: Heat transfer coefficient comparison for near-wall treatment methods considered.

Figure F.1 compares the pressure drop results obtained using the Gnielinski correlation with that of the numerical simulation utilising the realizable *k-ε* model and the three near-wall treatment methods being studied. For Dean numbers ranging between 5000 and 30000 there exist good agreement between the results obtained from the standard, non-equilibrium and enhanced wall treatment methods. In fact, the results almost coincide and the maximum error between the results of the empirical correlation and the numerical simulation using the enhanced wall treatment method is approximately 2% on average. For the standard and non-equilibrium wall functions the maximum error was found to be ±10 and ±14%, respectively. Results obtained for the realizable *k-ε* with standard wall treatment are in good agreement with the under 10% error reported by Colombo (2013:52).

In the medium to high Dean number region, 30000 to 55000 range, it can be seen that the enhanced wall treatment method is able to better reproduce the results of the Gnielinski correlation. Here the maximum deviation for the enhanced wall treatment method was found to be ±11% for Dean number equalling 55000. In contrast to the anticipated result, the standard wall function was able to outperform the non-equilibrium wall function for Dean numbers between 30000 and 55000.

This unexpected result may be contributed to the fact that the first cell height was kept constant during the investigations. This resulted in wall y-plus values ranging between 25.42 and 196.29 for the standard wall function, and 25.37 to 195.54 for the non-equilibrium wall function. Refer to Table F.1 and Table F.2 for results of y-plus values obtained.

Table F.1: Y-plus values for realizable *k-ε* with enhanced wall treatment.

1st Cell Height [mm]	Velocity [m/s]	Reynolds no. [--]	Y-plus [--]
0.018	0.20	3.814×10^{4}	0.59
	0.40	7.625×10^{4}	1.05
	0.60	1.144×10^{5}	1.49
	0.80	1.524×10^{5}	1.93
	1.00	1.905×10^{5}	2.38
	1.20	2.286×10^{5}	2.85
	1.40	2.667×10^{5}	3.33
	1.60	3.048×10^{5}	3.82
	1.80	3.429×10^{5}	4.30
	2.00	3.810×10^{5}	4.76

Table F.2: Y-plus values for realizable *k-ε* with standard and non-equilibrium wall functions (NEWF).

1st Cell Height [mm]	Velocity [m/s]	Reynolds no. [--]	Y-plus Standard [--]	Y-plus NEWF [--]
0.35	0.20	3.814×10^{4}	25.42	25.37
	0.40	7.625×10^{4}	46.52	46.19
	0.60	1.144×10^{5}	66.63	66.21
	0.80	1.524×10^{5}	86.15	85.70
	1.00	1.905×10^{5}	105.21	104.72
	1.20	2.286×10^{5}	123.91	123.38
	1.40	2.667×10^{5}	142.33	141.75
	1.60	3.048×10^{5}	160.52	159.87
	1.80	3.429×10^{5}	178.50	177.80
	2.00	3.810×10^{5}	196.29	195.54

A comparison between the Dean number and the heat transfer coefficient for the three wall treatment methods under consideration is shown in Figure F.2. The figure shows that the enhanced wall treatment method is again able to more accurately mimic the empirical solution, with a maximum reported deviation of ±5% being reported at Dean number equal to 57840. For Dean number of 28913, which equates to the coil design velocity of 1m/s, the error reduces to ±4%. The maximum deviation recorded for the standard and non-equilibrium wall function was ±6% and ±13%, respectively.

Overall, the realizable *k-ε* model with enhanced wall treatment was found to more accurately approximate the values obtained using the Gnielinski correlation. The results from the near-wall treatment study further suggest that the enhanced wall treatment method is able to predict heat transfer coefficients within helically coiled tubes with greater precision. Both the standard and non-equilibrium wall function was found to under predict both the pressure drop and heat transfer coefficients for the Dean numbers under considered.

References

Colombo, M. 2013. Experimental Investigation and Numerical Simulation of the Two-Phase Flow in the Helical Coil Steam Generator. PhD Thesis, Politecnico Di Milano, February 2013.

APPENDIX G: PHOTOS OF HELICALLY COILED BOILER SECTIONS

Figure G.1: Refractory cooler and support (LH); and superheater (RH)

Figure G.2: Evaporator section

Figure G.3: Economiser section